THE RESPONSE OF RADIATIVE FEEDBACKS, EQUATORIAL PACIFIC SEASONALITY, AND WETLANDS TO ORBITAL FORCING IN MODEL SIMULATIONS

By

MICHAEL PHILIP ERB

A Dissertation submitted to the

Graduate School-New Brunswick

Rutgers, The State University of New Jersey

in partial fulfillment of the requirements

for the degree of

Doctor of Philosophy

Graduate Program in Atmospheric Science

written under the direction of

Anthony J. Broccoli

and approved by

_____

_____

_____

_____

_____

New Brunswick, New Jersey

January, 2014

ABSTRACT OF THE DISSERTATION

The response of radiative feedbacks, equatorial Pacific seasonality, and wetlands to orbital forcing in model simulations

By MICHAEL PHILIP ERB

Dissertation Director:

Anthony J. Broccoli

By altering the seasonal and latitudinal distribution of insolation, variations in the Earth's orbital parameters have likely produced large climate changes in the past. To better understand the effect of orbital forcings, the GFDL Climate Model, version 2.1 (CM2.1), is used to perform idealized simulations in which only orbital parameters are altered while ice sheets, atmospheric composition, and other climate forcings are prescribed at preindustrial levels. These idealized simulations isolate the climate response to changes in obliquity and longitude of the perihelion alone. Additional simulations are conducted with a slab ocean model to assess the importance of ocean dynamics in parts of the climate response, and a water table model to study changes in groundwater. Though orbital forcing affects many aspects of the climate system, this research focuses on radiative feedbacks, the equatorial Pacific Ocean, and groundwater. Analysis shows that, despite being forced only by a redistribution of insolation with no

global annual-mean component, feedbacks induce significant global-mean climate change, resulting in mean temperature changes of -0.5K in a lowered obliquity experiment and +0.6K in a precession experiment. At times when the orbital configuration favors glaciation, cloud feedbacks partially counteract changes in summer insolation, posing an additional challenge to understanding glacial inception. Precession can significantly affect the equatorial Pacific seasonal cycle, especially in the east, through thermodynamic and dynamic mechanisms. In addition to the direct thermodynamic effect of insolation anomalies, heat is redistributed across the basin by way of thermocline signals in the precession experiments, which appear to result from changes in the strength of subtropical anticyclones and shifts in the regions of convection in the western equatorial Pacific. On land, groundwater responds to orbitally-forced changes in monsoon circulations and other precipitation anomalies, and the relationships between net water flux, groundwater in the CM2.1, and shallow water table extent are explored. These three aspects of the climate system -- radiative feedbacks, the equatorial Pacific Ocean, and groundwater -- all may have played important roles in past climate variations.

ACKNOWLEDGEMENTS

I would like to extend my thanks to Fanrong Zeng, John Krasting, and Lori Sentman for their help in conducting these simulations; Brian Soden for use of the radiative kernels and CMIP3 calculations; David Pollard for help with the calendar conversion; Virendra Ghate, Jennifer Kay, and Neil Barton for their cloud expertise; the NOAA Geophysical Fluid Dynamics Laboratory at Princeton and the Extreme Science and Engineering Discovery Environment for use of their computing resources; and two anonymous reviewers who commented on parts of this text. I would also like to thank my collaborators Tony Broccoli, Amy Clement, Neal Graham, Ben Lintner, Andrew Wittenberg, Gabriel Vecchi, Haibin Li, Ying Fan Reinfelder, and many others for their contributions to this work, and my doctoral committee Tony Broccoli, Ben Lintner, Ying Fan Reinfelder, Yair Rosenthal, and Amy Clement for their patience and useful advice.

Finally, I would like to thank my advisor, Tony Broccoli, for years of quality mentorship, my friends, for the many good times, and my family, for their love and support.

This research and my graduate education were supported by a School of Environmental and Biological Sciences (SEBS) Excellence Fellowship, a Graduate Assistance in Areas of National Need (GAANN) fellowship, and a grant from the Paleo Perspectives on Climate Change program of the National Science Foundation (Grant ATM0902735). This work used the Extreme Science and Engineering Discovery Environment (XSEDE), which is supported by National

Science Foundation grant number OCI-1053575. Some parts of this dissertation were previously published by the American Meteorological Society (AMS) in the Journal of Climate under the title “The contribution of radiative feedbacks to orbitally driven climate change”, by M. P. Erb, A. J. Broccoli, and A. C. Clement. The majority of the writing in that paper is my own, done with helpful advice from coauthors and reviewers.

Table of Contents

List of Tables

List of Illustrations

1. INTRODUCTION

Paleoclimate modeling and data studies suggest that large periodic variations in past global-mean temperature have been driven by cyclical changes in Earth's eccentricity, obliquity, and longitude of the perihelion. By dictating the earth's orbital geometry, these three cycles alter the seasonal and latitudinal distribution of insolation, which (amplified by internal climate system feedbacks) can result in global-mean climate change. The idea that orbital cycles are responsible for glacial-interglacial cycles and other Quaternary variations was championed by Milankovitch (1941) and has since been expanded in work by Hays et al. (1976) and numerous others in more recent times (e.g., Imbrie et al. 1993; Raymo and Nisancioglu 2003). For glacial-interglacial cycles, low obliquity (axial tilt) and Northern Hemisphere (NH) winter solstice perihelion encourage ice sheet expansion by reducing NH summer insolation. This orbital theory suggests that by allowing ice to survive through the less intense melt season, additional ice may accumulate during the winter, cooling the earth through a positive ice-albedo feedback.

Orbital signals in the proxy record have been well documented (e.g., Petit et al. 1999; Jouzel et al. 2007), but uncertainties remain concerning the exact climatic effects of orbital forcing. Hypotheses have been proposed to answer unresolved questions such as why climate variations dominantly occur with 100-kyr periodicity in the late Pleistocene (Imbrie et al. 1993; Huybers 2006) and why 40 kyr is the dominant period in the early Pleistocene (Raymo and Nisancioglu

2003; Huybers 2006; Huybers and Tziperman 2008). Because global annual-mean radiative forcing caused by orbital cycles is exceedingly small, substantial climate feedbacks are necessary to explain global-mean climate shifts.

Orbital cycles can affect such disparate aspects of the climate system as monsoon strength (Wang et al. 2008; Prell and Kutzbach 1987) and methane emissions (Loulergue et al. 2008). One region of change is the equatorial Pacific Ocean, which has been widely studied due to its importance to local climates, such as South America and Indonesia, as well as more distant climate through teleconnections. Part of its importance can be attributed to the El Niño-Southern Oscillation (ENSO), a coupled atmosphere-ocean system which has teleconnections to non-local temperature and precipitation patterns, tropical cyclone formation, and atmospheric circulation in distant regions of the globe (Diaz et al. 2001; Vecchi and Wittenberg 2010; Collins et al. 2010). However, local changes in the mean seasonal temperature cycle, which underlie ENSO variations, can also affect climate, and the annual cycle is important to aspects of the ENSO phenomenon (e.g., Tzipperman et al. 1994, 1997; Vecchi 2006; Lengaigne and Vecchi 2009). Research suggests that the equatorial Pacific mean seasonal cycle has changed in the past, likely having an effect on ENSO (Luan et al. 2012; Braconnot et al. 2012) as well as local and non-local climate.

The present-day eastern equatorial Pacific sea surface temperature (SST) cycle is characterized by maximum warmth in boreal spring and minimum warmth in boreal summer and autumn. Toward the western Pacific, the seasonal cycle is weaker and months later, exhibiting a more semi-annual cycle compared

to the east. Because tropical insolation forcing is semi-annual, with maxima near the two equinoxes, the eastern equatorial Pacific SST cycle cannot be fully explained as a direct thermodynamic response to insolation. Instead, research suggests that the equatorial Pacific seasonal cycle responds to a combination of zonal and meridional wind stresses and local heat fluxes caused by the seasonal shift of the insolation gradient, although the relative importance of these elements is a matter of debate (Harrison et al. 2009). Harrison et al. provide a summary of many current hypotheses, and notes that while many general circulation models (GCMs) are able to produce a realistic seasonal cycle in the region, modeling groups differ in their explanations of the cause. From their own experiments, Harrison et al. assert that the equatorial seasonal cycle is caused largely by zonal wind stress, and that the influence of meridional wind stress is limited to the very easternmost part of the Pacific. Despite uncertainty in the exact relationships, however, these intermediate forcing mechanisms are all ultimately driven by the annual insolation cycle, so changes in insolation from orbital forcing can potentially impact equatorial Pacific seasonality.

Other important aspects of the climate system are the water table and soil moisture. To some extent, both of these features are related to wetlands (Fan and Miguez-Macho 2010), which influence modern and past climate on regional as well as global scales. Over shorter timescales, wetlands alter albedo and exchange water and energy with the atmosphere through evapotranspiration (Fan et al. 2007). On longer timescales, they can act as a source for methane, nitrous oxide, and carbon dioxide, although they can be a sink for carbon as well

(Kayranli et al. 2010; Friborg et al. 2003; Fan and Miguez-Macho 2010). These greenhouse gases act as a positive feedback to climate change over glacial/interglacial cycles, and heat and water exchanges are key processes in the climate system.

Climate models, and GCMs in particular, provide a useful way to investigate the response of climate system to orbitally forcing. While much focus in modeling has been placed on specific time periods such as the last glacial maximum, last interglacial, and the mid-Holocene, attribution of the influence of orbital signals in such simulations is complicated by competing effects from changes in ice sheets and atmospheric composition. Idealized simulations in which only the orbital configuration is changed can provide a clearer picture of the feedback response.

Several studies using idealized simulations have already been completed, with early work being done by Phillipps and Held (1994), who investigated the climate response under various orbital configurations. More recently, Jackson and Broccoli (2003) ran an atmosphere-slab ocean model forced with only the accelerated orbital forcing of the past 165 kyr and found that low obliquity and late NH spring aphelion led to enhanced snow accumulation at times mostly consistent with the proxy record, largely influenced by storm activity and feedbacks involving sea ice. Further analysis highlighted the importance of atmospheric dynamics such as the northern annular mode (Hall et al. 2005). Other idealized orbital forcing studies have focused on the roles of vegetation and sea ice (Tuenter et al. 2005a,b), the effect of precession at the last

interglacial (Khodri et al. 2005), the response of the tropical climate to orbital forcing (Clement et al. 2004; Lee and Poulsen 2005; Timmermann et al. 2007), the response of monsoons to orbital forcing (Wyrwoll et al. 2007), and feedbacks in response to changes in obliquity (Lee and Poulsen 2008; Mantsis et al. 2011).

In this study, results from a fully coupled atmosphere-ocean general circulation model (AOGCM) are analyzed to further explore the response of feedbacks, equatorial Pacific seasonality, wetlands, and other climate features in orbitally forced climate simulations. While there have been other studies that look at the climate response to orbital cycles, little focus has been placed on the role of radiative feedbacks, particularly with a fully coupled AOGCM. In addition, a novel aspect of this part of the research is the use of the kernel method of feedback analysis, which has rarely been applied to paleoclimate simulations. Another novel aspect of this research is the idealized experimental design, in which the climate response to changes in obliquity and longitude of the perihelion may be isolated and explored. By setting all non-orbital forcings to preindustrial levels, the potential competing effects of changes in ice sheet extent and atmospheric composition are excluded.

To better understand the feedback response, feedbacks computed in these orbital experiments are also compared with feedbacks from a doubled CO_2 experiment. Previous studies have suggested that feedbacks operate similarly in simulations driven by changes in different forcing agents (e.g., CO_2, solar irradiance, and organic carbon), although the feedbacks do show some sensitivity to the latitude and altitude of the imposed forcing (Yoshimori and

Broccoli 2008). The comparison of feedbacks under orbital and anthropogenic forcing in the present research provides a test of this idea and will allow us to identify which aspects of feedback remain consistent under different forcings, and which are sensitive to the type and distribution of forcing.

As for the equatorial Pacific, several studies concerning the effect of orbital forcing on equatorial Pacific seasonality have already been conducted. Clement et al. (1999) forced climate with the accelerated orbital variations of the past 150 kyr in a simplified ocean-atmosphere model and found that Milankovitch cycles affected annual-mean equatorial Pacific SSTs through changes in seasonality. Timmermann et al. (2007) performed a simulation covering from 142 kyr before present to ~23 kyr after present with accelerated orbital forcing and found that equatorial Pacific seasonality is largely affected by precession through relationships with cloudiness and meridional temperature gradient. The influence of obliquity was primarily limited to changes in the annual-mean state. Ashkenazy et al. (2010) conducted simulations at 201 kya and 213 kya, times at which the perihelion occurs at the vernal and autumnal equinox, respectively, so that equatorial insolation was primarily characterized by annual, rather than semi-annual, cycles in both cases. They found that equatorial Pacific SSTs largely followed the given insolation pattern, with times of maximum and minimum SST lagging times of maximum and minimum insolation by a month or two, though some aspects of the response were likely influenced by air-sea interactions. Luan et al. (2012) forced the climate with the orbital configuration of the Early Holocene and mid-Holocene and found that eastern equatorial Pacific

seasonality was controlled by a combination of direct solar forcing and propagation of thermocline anomalies from the west. Furthermore, Luan et al. suggest that ENSO timing and magnitude are related to the strength of the seasonal cycle. Braconnot et al. (2012) presented some additional analysis of the relationship between equatorial Pacific seasonality and ENSO.

In the present study, the AOGCM simulations are analyzed to explore the response of the equatorial Pacific Ocean to orbital forcing, and complementary simulations with a slab ocean model help distinguish the relative importance of ocean processes in producing the modeled changes. Analysis of simulations from phase 5 of the Climate Modeling Intercomparison Project (CMIP5) helps test the robustness of the results.

Regarding groundwater, many general circulation models (GCMs) simulate groundwater with a “bucket” type model, which water can be precipitated into or evaporated out of, but which drains excess water into a different storage area when overfilled (Fan et al. 2007; Miguez-Macho et al. 2008). This type of groundwater model ignores the importance of the water table and, because the water table can affect wetlands and soil moisture (especially in areas with shallow water tables), omitting it from GCMs can lead to inaccurate results.

While future GCMs may implement better groundwater processes, dedicated groundwater models present a current solution. Fan and Miguez-Macho (2010) present one such model, in which water table depth can be modeled using recharge and temperature output from a GCM and other sources,

as well as specified topography, sea level, and other land properties.

Instead of considering each grid cell alone, as most GCMs do, Fan and Miguez-Macho's water table model allows water fluxes to be transported between grid cells. When climate-induced water flux enters from the top, it is subject to the forces of groundwater convergence and divergence, moving laterally between cells. Land elevation, slope, and ground properties influence lateral transport, and the balance between recharge, transport, and sea level (in coastal areas) determines water table depth (Fan and Miguez-Macho 2010). Areas where the water table is very near to the surface, which are the result of high precipitation, slow drainage, or transport of water from other regions, give an approximation of wetland distribution. Accurate modeling of the water table depth is crucial for estimating wetland distribution and methane emissions, since water table depth is a key factor for methane production in wetlands (Fan and Miguez-Macho 2010). To explore the response of groundwater to orbital forcing, and to evaluate the role of the water table and horizontal groundwater transport, results from the AOGCM simulations are used to help drive this water table model, and measures of the groundwater response in both models are explored.

In the following sections, the response of these three aspects of the climate system to orbital forcing will be investigated. Section 2 looks at the response of radiative forcing. Section 3 explores changes in the equatorial Pacific seasonal cycle. Section 4 investigates water table and soil moisture anomalies. The dissertation concludes with a summary and discussion of all of these topics in section 5.

2. RADIATIVE FEEDBACKS

This section focuses on the ways in which radiative feedbacks influence the Earth's climate response to orbital forcing. The design of the orbital forcing experiments is outlined in section 2.1. Section 2.2 explores the temperature response in these orbital experiments. The roles of feedbacks in producing the modeled climate change are discussed in section 2.3, and section 2.4 compares feedbacks under orbital forcings to those under anthropogenic forcing. Section 2.5 considers the potential effect of cloud feedbacks on large-scale NH ice sheet growth.

2.1 Experimental Design

The AOGCM used for this research is the Geophysical Fluid Dynamics Laboratory (GFDL) Climate Model, version 2.1 (CM2.1), which has atmosphere, ocean, land, and sea ice components coupled without flux adjustments. Atmospheric resolution is 2° latitude by 2.5° longitude with 24 vertical levels, and ocean resolution is 1° by 1°, becoming finer in the tropics to a meridional resolution of 1/ 3° with 50 vertical levels (Delworth et al. 2006). Reichler and Kim (2008) compared simulations of modern and preindustrial climate and found that CM2.1 performed the best among the models from phase 3 of the Coupled Modeling Intercomparison Project (CMIP3) at simulating modern climate.

To explore feedback mechanisms under obliquity and precession-only forcing, four idealized equilibrium simulations have been conducted (Table 1).

For obliquity, two simulations set obliquity to the low (22.079°) and high (24.480°) extremes of the past 600 kyr with all other variables, such as ice sheet extent and atmospheric composition, prescribed at preindustrial levels. To isolate precession, two simulations set perihelion to the NH winter solstice (WS) and NH summer solstice (SS) with all other variables prescribed to preindustrial levels except eccentricity, which is increased to 0.0493, the maximum eccentricity of the past 600 kyr (Berger and Loutre 1991). Simulations at the NH autumnal equinox (AE) and NH vernal equinox (VE) are also conducted, but will not be explored in this section. Because the effects of precession on insolation scale with eccentricity, the high value of eccentricity has been chosen to raise the signal-to-noise ratio in the precession results. A CMIP3 (Meehl et al. 2007) doubled CO_2 simulation, in which CO_2 is increased from preindustrial levels at 1% yr^{-1} until doubling and stabilized at that level thereafter (Stouffer et al. 2006), is compared with a preindustrial control run. This doubled CO_2 experiment is used as the basis for comparing feedbacks under orbital forcing with those estimated from anthropogenic forcing. Because CM2.1 lacks dynamic ice sheets, dynamic vegetation, and a carbon cycle, the analysis in this section focuses on the fast radiative feedbacks in the climate system (i.e., surface albedo, water vapor, lapse rate, and clouds).

In the precession results, a calendar adjustment has been made. Because of the elliptical shape of Earth's orbit, changes in longitude of the perihelion alter the lengths of seasons according to Kepler's second law. When comparing precession results on a standard fixed day calendar, this causes dates to

become offset from each other, making comparison between simulations problematic (Joussaume and Braconnot 1997). As a remedy for this problem, precession results have been converted to a common fixed-angular calendar where each ‘‘month’’ corresponds to a 30° arc of orbit. The conversion was made using the method outlined in Pollard and Reusch (2002), which is one of several proposed methods (Timm et al. 2008; Chen et al. 2010).

All of the orbital forcing simulations were run for 600 years, and the results presented in this dissertation use the mean of years 501-600. The precession simulations were run on a slightly updated version of CM2.1, which implements some bug fixes and has a slightly different value for snow albedo as well as some other minor changes, but these adjustments do not appear to affect the results. For analysis purposes, results of the orbital forcing simulations are presented as low minus high obliquity (the Lo-Hi experiment) and NH winter solstice perihelion minus NH summer solstice perihelion (the WS-SS experiment) in this section. This convention is undertaken so both experiments reduce the NH summer insolation, which is conducive to NH glaciation.

The Lo-Hi experiment discussed in this dissertation has also been analyzed in Mantsis et al. (2011), which uses two different methods to investigate feedbacks in response to obliquity changes. The present work expands upon the work of Mantsis et al. (2011) by exploring feedbacks computed with the kernel method in greater depth, with a focus on the physical mechanisms that lead to the feedback responses. The climate response and feedbacks in the WS-SS experiment have not been previously explored.

2.2. Insolation change and temperature response

The Lo-Hi experiment is defined by a decrease in Earth's axial tilt from 24.480° to 22.079°. In an annual-mean sense, this increases top-of-atmosphere (TOA) solar radiation in the tropics by several watts per square meter and decreases it at higher latitudes by up to ~15 W m^{-2}, increasing the equator-to-pole insolation gradient (Fig. 1a). Seasonally, the amplitude of the extratropical insolation cycle is reduced in both hemispheres - winter insolation increases by over 15 W m^{-2} and summer insolation decreases by up to ~50 W m^{-2}. In comparison, the WS-SS experiment consists of changing Earth's perihelion from NH summer solstice to NH winter solstice, resulting in increased insolation during the half year centered on NH winter solstice and decreased insolation for the rest of the year, with monthly insolation differences as large as ~100 W m^{-2} (Fig. 1b). The WS-SS insolation anomalies reach their peak in mid- and high-latitude summer when the magnitude of insolation is largest and result in a weakening of the NH but a strengthening of the Southern Hemisphere (SH) annual insolation cycle.

Responding to these changes, the seasonal- and annual-mean surface air temperature changes ΔT are shown for both experiments in Fig. 2. The Lo-Hi experiment exhibits a slightly positive ΔT throughout most of the tropics, averaging +0.1K over the tropics, with decreases in ΔT over the mid- and high latitudes becoming greater in magnitude toward the poles. In the midlatitudes, winter ΔT is mostly negative despite positive insolation changes during that season. This is because of the large heat capacity of the upper ocean, which

acts as an integrator of forcing. On the whole, the equator-to-pole temperature gradient is increased. Other features of the temperature response are discussed in Mantsis et al. (2011). Importantly, negative annual-mean ΔT extends equatorward of negative annual-mean insolation change, suggesting that feedbacks can overwhelm the direct effects of local insolation forcing.

In the WS-SS experiment, ΔT exhibits much more seasonal variation, with most latitudes experiencing negative ΔT from approximately June to October and positive ΔT through the rest of the year, which is delayed from the insolation changes by as much as several months because of the thermal inertia of the climate system. In Antarctica, which is more thermally isolated by virtue of the Antarctic Circumpolar Current, ΔT remains positive through almost all of the year. Spatially, annual-mean ΔT is especially positive over the North African and Indian Ocean monsoon regions, with negative ΔT mostly confined to midlatitude continents. The reasons for these changes are explored in the following section. In both the Lo-Hi and WS-SS experiments, global annual-mean insolation change is zero. A more accurate measure of the change in insolation felt by the climate system is radiative forcing, which is defined by Ramaswamy et al. (2001, p.353) as

> "the change in net (down minus up) irradiance (solar plus long-wave; in W m^{-2}) at the tropopause after allowing for stratospheric temperatures to readjust to radiative equilibrium, but with surface and tropospheric temperatures and state held fixed at the unperturbed values."

In this dissertation, radiative forcing does not include longwave radiation, and stratospheric temperatures are not allowed to adjust. Positive values of radiative forcing represent a heating of the climate system. Despite the absence of a net

change in global annual-mean insolation, mean radiative forcing is +0.10 W m^{-2} for Lo-Hi and -0.11 W m^{-2} for WS-SS because of the spatial and temporal covariance of insolation anomalies and albedo. Although the radiative forcing is small, global-mean ΔT is -0.5 K for Lo-Hi and +0.6 K for WS-SS. This disproportionate ΔT response (which is opposite to the sign of the radiative forcing in both cases) indicates the crucial role of radiative feedbacks in determining climate response to orbital forcing.

2.3. Radiative feedbacks

The ‘‘fast’’ radiative feedbacks, which are the focus of this research, involve changes in Earth’s surface albedo α_s, atmospheric water vapor q, vertical temperature lapse rate Γ, and cloud optical properties c. These four radiative feedbacks, plus the blackbody sensitivity δF/δT, equal the total climate sensitivity dF/dT (which is the change in radiative forcing per unit temperature change) in CM2.1, as expressed in the following equation:

$$\frac{dF}{dT} = \frac{\delta F}{\delta T} + \frac{\delta F}{\delta \alpha_s}\frac{\delta \alpha_s}{\delta T} + \frac{\delta F}{\delta q}\frac{\delta q}{\delta T} + \frac{\delta F}{\delta \Gamma}\frac{\delta \Gamma}{\delta T} + \frac{\delta F}{\delta c}\frac{\delta c}{\delta T} \quad (1)$$

In the absence of vegetation and geological changes, changes in surface albedo result from variations in sea ice and continental snow cover, which tend to enhance climate perturbations through melt or expansion. Water vapor is an effective greenhouse gas, so its concentration and distribution influence the atmosphere’s ability to affect longwave (LW) radiation and, to a smaller extent, shortwave (SW) radiation. A change in the lapse rate (the rate at which temperature decreases with height) affects the loss of LW radiation to space by

affecting the emitting temperature of the upper troposphere, which emits to space more readily than the surface. Clouds affect the radiation balance through the absorption and scattering of SW radiation and the absorption and emission of LW radiation in the atmosphere, so changes in the amount, distribution, and water content of clouds may amplify or diminish climate perturbations.

To isolate and quantify these feedbacks, the kernel method outlined in Soden and Held (2006) and Soden et al. (2008) is employed. This method uses a set of radiative ‘‘kernels,’’ computed using a stand-alone radiation code to quantify the net changes in TOA radiation that result from unit changes in surface albedo, water vapor, and lapse rate at each grid point and time of year. The cloud feedback cannot be calculated explicitly with this method because of strong nonlinearities in the cloud feedback, but is instead calculated by adjusting the change in cloud radiative forcing to account for the influence of clouds in masking noncloud feedbacks (i.e., temperature, water vapor, and surface albedo; Soden et al. 2004, 2008). The kernel method is convenient because it can differentiate the effects of concurrent radiative feedbacks without the need to rerun model code, which can be computationally expensive. In interpreting the following results it should be noted that the results are here expressed as the effect of feedbacks on net TOA radiation ΔR_{net} (W m^{-2}), rather than as feedbacks (W m^{-2} K^{-1}). Doing so avoids dividing by the small values of global-mean ΔT in the orbital experiments. Positive values of ΔR_{net} indicate increased net downward radiation. In the following subsections the role of each feedback under orbital forcing is examined. A further analysis of some of the mechanisms at work will follow in

section 5.

2.3.a. Surface albedo feedback

The ΔR_{net} from the surface albedo feedback is shown in Figs. 3a and 3b. In the Lo-Hi experiment, the sea ice fraction increases in the Arctic Ocean, Greenland Sea, Barents Sea, and Bering Sea, and snow cover increases across much of the NH high-latitude continents, increasing reflection of SW radiation primarily in the NH summer when insolation values are high. SH changes are characterized by increases in sea ice in much of the Southern Ocean, but snow expansion is limited by a lack of SH midlatitude continental areas and by the thermal isolation of Antarctica, which sustains snow cover year-round, causing SH changes to be less extensive than NH ones. Global-mean ΔR_{net} for each feedback is given in Table 2. The global-mean ΔR_{net} from the surface albedo feedback in the Lo-Hi experiment is -0.27 W m^{-2}, indicating a cooling effect.

In the WS-SS experiment, snow and sea ice changes occur in largely the same regions as the Lo-Hi experiment, but present a more seasonally varying response because of the more seasonal nature of the forcing. In the NH, snow cover retreats more during a warmer NH spring and Arctic sea ice retreats less during a cooler NH summer. Aided by the large size of NH midlatitude continents, snow retreat has a larger total effect on albedo than sea ice increase, so the total effect of these two competing NH changes is a warming. In the SH, Southern Ocean sea ice retreats farther than normal during the warmer SH summer. However, because of the limited area of SH midlatitude continents, SH snow

cover anomalies during SH spring are small despite cooler temperatures. This imbalance in the land-sea distribution allows sea ice reductions to dominate the SH albedo response, leading to a warming effect. Global-mean ΔR_{net} from the surface albedo feedback is +0.31 W m^{-2} in the WS-SS experiment, emphasizing the importance of seasonality and surface type in determining feedback responses.

2.3.b. Water vapor feedback

The ΔR_{net} from the water vapor feedback is given in Figs. 3c and 3d and is characterized by both latitudinal and seasonal variations for Lo-Hi and mostly seasonal variations for WS-SS, generally having a warming effect where ΔT is positive and a cooling effect where ΔT is negative. To see what effect circulation changes have on this feedback, the water vapor response is separated into two components (Fig. 4): a thermodynamic component that corresponds to the change in specific humidity that would result from ΔT according to the Clausius-Clapeyron relation with a fixed RH and a dynamic component resulting from changes in atmospheric eddies and circulation patterns.

In the Lo-Hi experiment, thermodynamic changes are characterized by increased water vapor in the tropics, where ΔT is positive, and decreased water vapor elsewhere, where ΔT is negative. Dynamic changes show an additional increase in tropical water vapor associated with an enhanced annual-mean Hadley circulation, with enhanced dry zones in regions of subtropical descent. Enhancement of the annual-mean Hadley circulation is consistent with the

increased equator-to-pole insolation and temperature gradients, as previously found by Otto-Bliesner and Clement (2004) and Rind and Perlwitz (2004).

In the WS-SS experiment, thermodynamic changes dominate at higher latitudes, but dynamic changes are equally large in the tropics. These dynamic changes are primarily associated with changes in monsoons. Precipitation differences in the WS-SS experiment (Table 3) reveal diminished NH rainy seasons in North America, northern Africa, and Asia and enhanced SH rainy seasons in South America, southern Africa, and Australia. Changes in monsoon intensity affect the amount of water vapor transported into continental regions, with weakened NH monsoons transporting less water vapor into NH continents and strengthened SH monsoons transporting more. Strengthening and weakening of monsoons in response to precession forcing is a robust feature of both proxy (e.g., Fleitmann et al. 2007; Wang et al. 2008; Ziegler et al. 2010) and model (e.g., Prell and Kutzbach 1987; Tuenter et al. 2003; Wyrwoll et al. 2007) studies. Monsoon changes in the Lo-Hi experiment (not shown) are present, but comparatively small, mostly being characterized by weaker monsoons in most regions and equatorward shift of areas of maximum rainfall. The Australian monsoon shows only a small dependence on obliquity changes in the present Lo-Hi experiment, in contrast to larger variations modeled by Wyrwoll et al. (2007).

When considered in terms of global-mean climate response, the water vapor feedback is least important in these experiments. Despite strong regional effects, it is chiefly characterized by positive and negative effects of nearly equal

magnitude. It accounts for only about 10% of the total global-mean ΔR_{net} in both Lo-Hi and WS-SS experiments (Table 2).

2.3.c. Lapse rate feedback

The ΔR_{net} from the lapse rate feedback is shown in Figs. 3e and 3f. The lapse rate feedback is related to changes in the vertical thermal structure of the atmosphere. At low latitudes, deep convection maintains a nearly moist adiabatic lapse rate, amplifying ΔT at higher altitudes through the transport of latent heat. At higher latitudes, where synoptic systems play a larger role and the lapse rate is not moist adiabatic, ΔT is generally smaller aloft relative to the surface (Bony et al. 2006).

In the Lo-Hi experiment, ΔR_{net} from the lapse rate feedback is mostly negative at higher latitudes and near zero in the tropics. This is partly consistent with the latitudinal nature of the response mentioned above: at higher latitudes the temperature decreases more at the surface than aloft. Seasonally, a large reversal occurs in the sign of the Arctic lapse rate feedback between NH summer and fall. The reduced Arctic stability during NH summer results from melting ice keeping the surface temperatures near freezing while temperatures cool aloft. This happens because of the influence of sea ice. Sea ice melting is reduced during NH summer but, because there is enough energy to melt sea ice in both cases, surface temperature stays near zero while temperatures cool aloft, leading to reduced atmospheric stability. Afterward, in NH fall, increased sea ice better insulates the surface air from the Arctic waters, allowing temperatures to

plummet more quickly at the surface and resulting in increased atmospheric stability. Manabe and Stouffer (1980), Robock (1983), and Hall (2004) observe the same mechanism in increased CO_2 and altered solar constant experiments, noting that anomalous insolation largely impacts sea ice melt rather than ΔT in NH summer, while subsequent sea ice thickness anomalies affect ΔT through changes in ocean insulation in NH fall and winter. This dichotomy between the lapse rate feedback in Arctic summer and fall also influences local clouds, discussed in the next section. Additionally, the lapse rate feedback tends to be negatively correlated with the water vapor feedback, which partially counteracts its effects (Colman 2003; Bony et al. 2006).

In the WS-SS experiment, many of these same features are observed, but like the water vapor response, sign changes are more seasonal in nature. In the low latitudes, where the lapse rate is closer to moist adiabatic, the effect of the lapse rate feedback is generally positive when ΔT is negative and negative when ΔT is positive. In the Arctic, cooler summers lead to the same dichotomy of summer and fall lapse rates that was seen in the Lo-Hi experiment.

Of the four radiative feedbacks, the lapse rate feedback has among the largest effects in both the Lo-Hi and WS-SS experiments, resulting in a global-mean ΔR_{net} of -0.90 W m^{-2} for Lo-Hi and +0.47 W m^{-2} for WS-SS.

2.3.d. Cloud feedback

Figures 3g and 3h show ΔR_{net} from the cloud feedback in the Lo-Hi and WS-SS experiments. Because cloud feedback can affect both the SW and LW

radiation, it is useful to view those effects separately (Fig. 5). In the Lo-Hi experiment, the effect of clouds is manifested most strongly in the SW component, with the LW effect being smaller and opposite at most latitudes. Outside of the tropics, the SW effect is dictated predominantly by changes in cloud liquid water content. Since cloud droplet concentration is held constant in the CM2.1 (Anderson et al. 2004), increased cloud liquid water results in an unchanged concentration of larger droplets, which increases cloud albedo. The modeled SW effect is also affected by increases in low-cloud fraction throughout much of the midlatitudes, especially over NH continental areas and the Southern Ocean (Fig. 6). The LW effects are mostly caused by changes in high clouds (not shown), with areas of positive LW ΔR_{net} generally being associated with increased high cloud fraction. An analysis of interannual variability in a preindustrial CM2.1 simulation reveals that, with the exception of over Greenland, Arctic cloud water content is positively correlated with stability in July (Fig. 7). This relationship suggests that the decrease in Arctic cloud water content during NH summer is associated with the decreased stability during those months. In a more stable atmosphere, the inhibition of vertical mixing allows moisture to remain concentrated in the Arctic boundary layer, resulting in greater cloud water content at low levels. A decrease in stability is thus associated with a reduction in the water content of low clouds in the model. The cloud feedback accounts for about 33% of the global-mean ΔR_{net} in the Lo-Hi experiment. A more detailed analysis of these cloud changes may be found in Mantsis et al. (2011).

The cloud feedback in the WS-SS experiment is more spatially complex and larger in magnitude than the Lo-Hi experiment, contributing over 40% of the global annual-mean ΔR_{net}. Annual-mean ΔR_{net} is positive over most oceanic regions with negative values generally confined to continental areas and limited oceanic areas such as the band of ocean between ~40° and 60°S. As in the Lo-Hi experiment, changes in ΔR_{net} from clouds primarily result from SW effects, with LW effects generally being opposite sign and smaller. The exception to this is near the equator, where changes in SW and LW are comparable due primarily to two mechanisms. First, weakened NH monsoons over northern Africa, India, and parts of China result in reduced cloud water content, ice content, and cloud fraction over those areas during NH summer. Strengthened SH monsoons over South America, southern Africa, and Australia have an approximately opposite effect in those regions. Of the monsoons, the North African monsoon has the largest impact on cloud feedback, resulting in an annual-mean ΔR_{net} over West Africa of more than 20 W m^{-2}. The second mechanism is the cooling of the eastern equatorial Pacific of over 2 K during NH summer, which is associated with increases in low clouds at the expense of mid- and high clouds. Unlike most of the other changes in cloud fraction, this is accompanied by little change in cloud water content and is simply a preferential increase in low clouds. Similar preferential changes in clouds may be seen in Clement et al. (2010). These cloud changes are not the primary cause of the eastern equatorial Pacific ΔT, but they contribute to ΔR_{net} by more than -20 W m^{-2} over much of the region during NH summer. A warming of the eastern equatorial Pacific during NH winter results in

positive ΔR_{net} during that time.

By far the largest effect of clouds in the WS-SS experiment occurs in the NH high-latitude summer. Widespread decreases in cloud water content at latitudes poleward of 40°N in the WS-SS experiment likely result from decreased high-latitude summer stability. The associated reduction in cloud albedo, together with a decrease in low-cloud fraction over the Arctic and northern Atlantic and Pacific basins during July and August (Fig. 6), allows a larger percentage of SW radiation to the reach the surface. This results in a ΔR_{net} from the cloud feedback between +15 and +20 W m^{-2} in the NH high-latitude summer, partially counteracting the direct radiative forcing. In these experiments, clouds may be regarded as a negative feedback on orbital forcing in this region and will be discussed further in section 6.

Because clouds have long been considered one of the major sources of uncertainty in climate modeling, it is reasonable to wonder if the cloud responses described above may be model dependent, particularly given that much of the change comes from the effect of clouds on SW radiation. Soden and Vecchi (2011) analyzed doubled CO_2 experiments in 12 coupled AOGCMs and showed that while there is some spread among the models, they do agree on many characteristics of cloud feedback. A comparison of CM2.1 cloud feedbacks with the multimodel analysis of Soden and Vecchi (2011) indicates that the behavior of the GFDL CM2.1 is broadly consistent with other AOGCMs (Fig. 8). The main disagreement between models occurs in the relatively small area poleward of 80°N in the SW component. The general agreement between these models

provides some confidence that the results obtained in the present orbital forcing experiments may not be model dependent.

2.3.e. Total feedbacks

The total effect of the surface albedo, water vapor, lapse rate, and cloud feedbacks is shown in Figs. 3i and 3j for the Lo-Hi and WS-SS experiments, respectively. In the Lo-Hi experiment, the feedbacks generally result in strongly negative ΔR_{net} at the mid- and high latitudes and a weakly positive ΔR_{net} at the low latitudes. This cools the mid- and high latitudes much more than it warms the low latitudes, contributing to the modeled temperature response. In the WS-SS experiment, ΔR_{net} is mostly positive from November to April, with a mix of positive and negative ΔR_{net} during the rest of the year, contributing to the modeled annual-mean warming in the WS-SS experiment.

When looking at global annual-mean values, the lapse rate and cloud feedbacks contribute most strongly to the total ΔR_{net}, together accounting for over 70% of the total ΔR_{net} in each experiment (Table 2). Water vapor accounts for the smallest mean changes in the orbital experiments, which is in contrast to the doubled CO_2 experiment, where it is the most important by far, and the surface albedo feedback shows similar magnitude of effects in the two experiments despite vastly different forcings. Because obliquity and precession variations result in equal areas of positive and negative TOA insolation anomalies, the global-mean importance of each feedback becomes dependent on the spatial and temporal distribution of the forcing, the nonlinearities of each

feedback's response to positive and negative forcing, and other large-scale mechanisms such as circulation and monsoons. It is worth noting that all four feedbacks work counter to the initial weak radiative forcing in both orbital experiments. Total ΔR_{net} from these fast radiative feedbacks is -2.03 W m^{-2} in the Lo-Hi experiment and +1.72 W m^{-2} in the WS-SS experiment, leading to ΔT of -0.5K and +0.6K, respectively. Even when given no global annual-mean insolation change, feedbacks can push the climate toward a colder (as in the Lo-Hi experiment) or warmer (as in the WS-SS experiment) state.

2.4. Comparison with feedbacks under doubled CO_2 forcing

To more fully understand the mechanisms responsible for feedbacks in the orbital experiments, feedbacks computed for the Lo-Hi and WS-SS experiments with the kernel method are compared with feedbacks estimated from the CM2.1 doubled CO_2 experiment. Three questions are posed: 1) To what extent are feedbacks in the orbital experiments consistent with those responding to doubled CO_2? 2) Can feedbacks be understood as a simple response to local ΔT, regardless of the type of forcing, or are spatially and seasonally dependent response mechanisms at play? 3) If these other mechanisms do produce some of the regional climate change, are they also important to the global-mean response?

To answer these questions, a calculation is performed to estimate the effect feedbacks would have if the relationship between each feedback and local ΔT was exactly the same in the orbital experiments as it is in the doubled CO_2

experiment. Stated more explicitly, these estimated feedbacks are calculated by dividing ΔR_{net} from doubled CO_2 feedbacks by the seasonally/spatially varying surface ΔT in the doubled CO_2 experiment to normalize for temperature, then multiplying them by the ΔT in each orbital experiment, as expressed below:

$$estimated\ effect\ of\ feedback\ =\ \delta F_{CO2} * \frac{\Delta T_{orbital}}{\Delta T_{CO2}} \quad (2)$$

Values of ΔT_{CO2} (not shown) are generally consistent with ΔT from other doubled CO_2 experiments, with a global-mean ΔT_{CO2} of +2.4 K. We compare the actual effect of feedbacks in the orbital runs, calculated with the kernel method (Fig. 3), with the estimated effect of feedbacks as determined above (Fig. 9). If the actual and estimated figures were identical, it would imply that the effect of feedbacks on ΔR_{net} varied linearly with local surface ΔT in the same manner in both the doubled CO_2 and orbital experiments, and that the feedbacks depend only on the local temperature response. Differences between the actual and estimated response indicate a dependence on more complex response mechanisms. Global-mean values for the estimated feedbacks are given in parentheses in Table 2.

A shortcoming of this method is the overestimation of feedback effects in areas where ΔT_{CO2} is near zero. To account for this, areas where ΔT_{CO2} is between -0.5 and +0.5K have been masked out. However, the estimate is still disproportionately affected by areas of low ΔT_{CO2} , so this section will focus primarily on differences in sign, not magnitude, in the comparison of the actual (Fig. 3) and estimated (Fig. 9) effect of feedbacks.

2.4.a. Lo-Hi experiment

Of the four feedbacks in the Lo-Hi experiment, the surface albedo feedback shows the strongest similarities between the actual and estimated response, suggesting that changes in snow and sea ice are primarily associated with local ΔT and do not rely heavily on other mechanisms. While this is perhaps not surprising, it is interesting to note that the actual and estimated responses are similar, despite the opposite signs of high-latitude ΔT in the Lo-Hi and CO_2 experiments.

In the remaining feedbacks, differences are apparent in the mid- to high latitudes during summer in both hemispheres. The high-latitude changes stem from relatively low ΔT_{CO2} in the Southern Ocean and northern Atlantic during their respective summers, where changes in ocean circulation tend to reduce local warming in global warming experiments (Stouffer et al. 2006) and in parts of Canada and Russia during NH summer, where ΔT_{CO2} is low because of increased precipitation in the doubled CO_2 experiment (Wetherald 2010). Increased precipitation throughout the year in these NH high-latitude continental regions makes the soil wetter, allowing increased evaporation during NH summer. This decrease in the Bowen ratio diminishes local warming. Because ΔT in the orbital experiments is not affected in the same way in these regions, differences arise between the actual and estimated feedback responses.

In the water vapor feedback, the calculated effect of the water vapor feedback is larger at the equator and smaller in the North African and Asian monsoon regions than in the estimation. This difference is caused by the

enhanced Hadley circulation and a slight weakening of those monsoons in the Lo-Hi experiment, which rely more on the latitudinal temperature gradient and seasonal changes than local ΔT alone. Monsoon changes also lead to differences in the cloud feedback, as weaker NH monsoons result in local decreases in summer clouds. These cloud feedbacks are not well reproduced in the estimated response.

Outside of these regional variations, several wider-scale differences should be addressed. In particular, the calculated effects of the lapse rate and cloud feedbacks are more negative than in the estimate, and the effect of the water vapor feedback is more positive (Table 2). One hypothesis to explain these differences involves the transport of moist static energy (MSE) by the mean meridional circulation. In the Lo-Hi experiment, increases in insolation at low latitudes produce positive MSE anomalies through increases in surface air temperature and specific humidity. Decreases in insolation at high latitudes have the opposite effect. From a Lagrangian perspective, the mean meridional circulation transports low-latitude air upward and poleward, while air at the poles is transported downward and equatorward. This circulation should transport positive MSE anomalies poleward in the upper troposphere and negative MSE anomalies equatorward near the surface. This differential transport should have the effect of stabilizing the atmosphere in the Lo-Hi experiment and affecting radiative feedbacks in three important ways: 1) A decreased lapse rate emits more LW radiation to space, cooling the climate; 2) a more stable atmosphere sustains additional water vapor at height, increasing the greenhouse effect and

partially offsetting the primary radiative effect of a decreased lapse rate; and 3) a more stable atmosphere encourages increased cloud water (Fig. 7), reflecting more insolation back to space. Thus, despite potential changes in water vapor, the export of high-latitude air with reduced MSE by the mean meridional circulation may be responsible for pushing the Lo-Hi experiment toward a colder global-mean climate. This would allow regions of negative ΔT to be sustained equatorward of the regions of negative insolation change, as seen between approximately 20° and 40° latitude in both hemispheres in the Lo-Hi experiment.

Outside of these important differences, however, many aspects of the feedback responses remain relatively consistent between the Lo-Hi and CO_2 experiments. The sign of the surface albedo and water vapor feedbacks is consistent over most regions, as are the lapse rate and cloud feedbacks outside of the midlatitudes, suggesting that many aspects of the feedbacks depend upon the local temperature change and are relatively insensitive to the global distribution and type of forcing. Notably, the dichotomy between the Arctic summer and fall lapse rate responses in the Lo-Hi experiment is well reproduced in the estimated feedback response, reinforcing the notion that this feature is a robust model response largely dependent on local, rather than global, processes.

This comparison between actual and estimated feedbacks suggests that many aspects of feedbacks are a direct response to local ΔT, but some aspects depend on changes in atmospheric circulation. This is especially apparent when comparing the total effect of feedbacks (Figs. 3i, 9i), which show large-scale similarities as well as some important differences. Table 2 lists global-mean

values of ΔR_{net} for both the actual and estimated response. The surface albedo and water vapor responses are relatively similar, but the larger differences in the lapse rate and cloud responses indicate complexities in the relationship between feedbacks and the seasonal and latitudinal pattern of temperature change.

2.4.b. WS-SS experiment

Comparing the actual and estimated responses in the WS-SS experiment reveal large-scale similarities, but, as in the Lo-Hi experiment, important differences become apparent as well. For the water vapor feedback, the greatest differences occur at low latitudes, mostly corresponding to monsoonal changes, which are much larger in the WS-SS experiment than the doubled CO_2 experiment. These large monsoonal changes in the WS-SS experiment point to the importance of the seasonality of the forcing. Because the thermal inertia of the ocean allows the climate system to maintain a memory of forcing in earlier seasons, previous seasonal changes may impact later climate response. It is important to note, however, that while NH and SH monsoons produce changes in the water vapor feedback that are of the opposite sign, these anomalies are not of equal magnitude, making the actual ΔR_{net} from the water vapor feedback +0.19 W m^{-2}, while the estimated one is +0.61 W m^{-2}. Some of this stems from the fact that changes in the North African monsoon are more pronounced than changes in other monsoons, significantly decreasing the water vapor over northern Africa.

Monsoon changes also explain some of the differences in the lapse rate

and cloud feedbacks. In the lower latitudes, less convectively active NH monsoons transport less latent heat aloft, increasing the lapse rate over northern Africa and the Indian subcontinent. The SH monsoons have the opposite effect over South America, southern Africa, and Australia during SH summer. Monsoonal changes also reduce cloud water content and cloud fraction over NH monsoon regions and increase them over SH monsoon regions. These changes, as well as the response of clouds to seasonal temperature anomalies in the eastern equatorial Pacific, are not well represented in the estimated response. This is apparent when comparing the total effect of feedbacks (Figs. 3j, 9j), again pointing toward the importance of seasonal variations in determining parts of the feedback response.

Taking a step back, Table 2 shows that the latitudinal- and seasonal-dependent response mechanisms outlined above are important not just to aspects of local ΔR_{net} but also to global ΔR_{net}. Therefore, the questions posed at the beginning of this section may be answered as follows: 1) There are many large-scale similarities between the actual and estimated effect of the feedbacks, but also crucial differences. 2) Important parts of the feedback response cannot be understood as a simple response to local ΔT. 3) Changes in systems such as the Hadley circulation and monsoons are important to the global-mean climate response.

2.5. Potential effect of feedbacks on expansion of NH ice sheets

According to orbital theory, low obliquity and perihelion at NH winter

solstice (which are simulated separately in Lo-Hi and WS-SS) should promote NH ice sheet growth by allowing high-latitude snow to survive through cooler summers. Although the current experiments cannot explicitly address the slow feedbacks that are instrumental in amplifying the climate response to orbital changes because of the absence of dynamic ice sheets and biogeochemistry in CM2.1, the fast radiative feedbacks can be evaluated to see whether they encourage high-latitude NH perennial snow cover in these experiments or not.

Both Lo-Hi and WS-SS result in high-latitude cooling during the NH summer, with Lo-Hi additionally cooling at high latitudes year round (Fig. 2). Spatially, the NH high-latitude summer ΔT is negative almost everywhere in both experiments (Figs. 10a,b, shading), though the WS-SS experiment has ΔT near zero over northern ocean areas. Some of this pattern may be attributed to the summer cloud feedback (Figs. 10a,b, contours), which contributes positive ΔR_{net} over high-latitude ocean regions and some continental regions in both experiments. The total effect of feedbacks (not shown) has the same sign as the cloud feedbacks over most latitudes, enhancing cooling in some regions while diminishing it in others.

The NH high-latitude summer WS-SS cloud feedback constitutes one of the largest feedbacks seen anywhere in the orbital experiments and, as previously stated, involves widespread decreases in cloud water content over the majority of regions poleward of approximately 40°N associated with decreased high-latitude summer stability. Together with a decrease in low-cloud fraction over the Arctic and northern ocean basins during July and August (Fig. 6), this

decrease in cloud water reduces cloud albedo and allows a higher percentage of SW radiation to reach the surface. The region of positive ΔR_{net} from the cloud feedback extends over parts of northern Canada including Baffin Island, which remains one of the most likely locations for past initiations of the Laurentide Ice Sheet (Clark et al. 1993). This suggests that the cloud feedback could partially counteract changes in summer insolation at or near these regions at times when the orbital configuration is favorable for ice sheet expansion.

However, despite the decreases in insolation and continental temperature in both experiments, neither experiment shows a widespread increase in perennial snow cover, which would be the precursor to ice sheets. Perennial snow cover remains confined to Greenland and Antarctica, with the sole exception of a single point over the Himalayas in the WS-SS experiment, which maintains its snow throughout the cooler summer. An analysis of melting degree-days, which indicate whether snowmelt would increase or decrease over the course of the year, shows that these experiments are still in agreement with orbital theory. Figures 10c and 10d show that melting degree-days are reduced over almost all continental regions poleward of 30°N. Because continental temperature can drop significantly below zero in winter, melting degree-days are more affected by summer ΔT, which is negative in both experiments, than by winter ΔT, which is negative in the Lo-Hi experiment but positive in the WS-SS experiment. These reductions in melting degree-days should allow snow to remain on the ground later in the melt season in both experiments.

Large-scale increases in perennial snow cover are not expected in these

experiments for several reasons: First, the present experiments model low obliquity and NH winter solstice perihelion forcing separately, while orbital theory suggests that both should be present to start glaciations. Second, GFDL CM2.1 lacks the fine resolution required to resolve the tall mountain peaks where glaciations likely begin. Third, when comparing a modern run from GFDL CM2.1 against data from the Climatic Research Unit, version 2.1 (CRU v.2.1), temperature dataset (Mitchell and Jones 2005), GFDL CM2.1 displays a warm bias of several degrees over northern Canada and parts of northern Russia during NH summer. This warm bias increases the drop in temperature needed to promote permanent snow cover in the CM2.1, even if the first two reasons listed above are ignored.

As a final note, an open question remains regarding how feedbacks may change as ice sheets grow. Changes in surface type and elevation, both of which will happen with expanding ice sheets, could have significant effects on feedbacks. Snow feedbacks, which can be pronounced over dark surfaces such as forests and grasslands, would be much weaker over ice sheets, changing the regional characteristics of the surface albedo feedback. The lapse rate feedback will be affected by the much cooler surface temperatures. Higher topography associated with ice sheet growth may lead to a southward displacement of the NH winter jet stream (Clark et al. 1999). Such changes in the atmospheric circulation and topography may influence the cloud feedback. Because of the complexity of these potential responses, feedbacks that initially discourage or promote high-latitude cooling may change with the growth of ice sheets. While

this topic deserves further research, analysis of those potential responses is beyond the scope of the present experiments.

3. EQUATORIAL PACIFIC SEASONALITY

The equatorial Pacific seasonal cycle exhibits significant changes in response to orbital forcing. This response will be explored in this section. Section 3.1 of this dissertation describes the experimental design. The response of equatorial Pacific seasonality to precession is explored in section 3.2, and section 3.3 investigates the response of seasonality to obliquity. In section 3.4, these results are compared to output from mid-Holocene simulations in CMIP5 models. Section 3.5 provides additional discussion as well as some implications for analysis of proxy records.

3.1. Experimental Design

The primary model used in this research is the GFDL CM2.1, a coupled atmosphere-ocean GCM, as described in section 2.1. In the equatorial Pacific, CM2.1 control simulations compare well against observations, accurately capturing many aspects of equatorial Pacific climatology while showing relatively few biases (Wittenberg et al. 2006). Compared to other CMIP3 models, the CM2.1 performs better than many models at reproducing the annual-mean and seasonal range of tropical zonal winds and produces a reasonably accurate cold tongue, and is among the best models at simulating realistic ENSO variability (van Oldenborgh et al. 2005; Capotondi et al. 2006; Merryfield 2006; Joseph and Nigam 2006; Reichler and Kim 2008; Guilyardi et al. 2009; Kug et al. 2010). One difficulty with CM2.1's simulation of the equatorial Pacific is the so-called "double

ITCZ" problem, in which the Intertropical Convergence Zone (ITCZ) has a northern and southern component, producing too much precipitation near 10°S during boreal spring (Wittenberg et al. 2006). However, this problem is common to many GCMs (Lin 2007), so the present results would likely not be improved by switching to a different model of the same generation.

To explore the response of equatorial Pacific seasonality to precession and obliquity, the AE, WS, VE, and SS precession simulations and the Lo and Hi obliquity simulations, described in section 2.1, are analyzed. A final precession simulation is run with eccentricity set to 0, eliminating perihelion and any possible effect of precession. This zero eccentricity simulation is used as a point of comparison for a preindustrial simulation. The preindustrial simulation is used for control purposes, and a mid-Holocene (6ka) simulation is used for comparison in section 3.4 (Table 1).

To better isolate and understand the role of ocean dynamics in these CM2.1 simulations, a second set of simulations was run on a slab ocean version of the model described above, here called the SM2.1. The atmosphere and ice components in the SM2.1 are identical to the CM2.1, but they are coupled to a single layer slab ocean with a fixed depth of 50 m which exchanges heat and moisture with the atmosphere but has no horizontal or vertical transport. A repeating seasonally and spatially varying climatology of heat fluxes are prescribed to account for the missing oceanic heat transport (Stouffer et al. 2006) and to prevent the overproduction of sea ice. Except for at high latitudes in the preindustrial simulation, where there is a strict limit on the maximum thickness of

sea ice, these heat flux terms are identical across SM2.1 simulations and result in a realistic cold tongue without dictating the climate response to orbital forcing. The land model has also been updated in the SM2.1 relative to CM2.1, but still uses prescribed vegetation. Simulations using this slab ocean model are set up in a similar manner as the CM2.1 simulations, consisting of the five precession and two obliquity simulations as well as the preindustrial control run. As was done with the CM2.1 precession simulations (see section 2.1), a calendar adjustment has been made to the SM2.1 precession results to account for the shift in dates that occurs when longitude of the perihelion is altered under high eccentricity.

For the CM2.1 orbital forcing simulations, results in this section use the mean climatology of the final 100 years of the 600 year runs. SM2.1 simulations were run for 100 years, and results in this dissertation use climatologies of the last 50 years. To analyze the results, precession simulations are compared against the preindustrial control runs, while obliquity simulations are analyzed as low obliquity minus high obliquity.

3.2. Effects of precession on equatorial Pacific seasonality

Precession, which has periodicities around 20 kyr, alters the timing of perihelion, increasing insolation during approximately half of the year and decreasing it during the other half. At present, perihelion occurs in the first week of January, so equatorial insolation is slightly higher in boreal winter than boreal summer, though both seasons have reduced equatorial insolation compared to

spring and autumn, when solar radiation intercepts the tropics at a lower mean zenith angle. The gradual shift in the longitude of perihelion determines which season has increased insolation due to closer proximity to the sun, an effect which is amplified by high eccentricity in the precession simulations (Fig. 11). Simulations with perihelion at the autumnal equinox (AE) and vernal equinox (VE) are characterized by a sharp equatorial insolation maximum at that equinox and a flatter double minimum during the opposite time of year. The simulations with perihelion at winter solstice (WS) and summer solstice (SS) have flatter insolation maxima and sharper minima. In all four of these cases, the enhanced eccentricity results in seasonal insolation distributions in the tropics which are more annual in their period, rather than semi-annual as in the preindustrial simulation. In the zero eccentricity simulation, equatorial insolation has no annual component, instead having a pronounced semi-annual cycle with maxima at the two equinoxes. Maximum monthly TOA equatorial insolation anomalies between preindustrial and the four precession simulations are ~50 W m^{-2}, which is a change of ~10% of the total insolation. Between the four precession simulations, insolation anomalies can reach ~80 W m^{-2}.

3.2.a. CM2.1 simulations

The present day equatorial Pacific SST cycle is marked by strong seasonal variation in the east, with maximum temperatures in boreal spring and minimum temperatures in boreal summer and autumn, as can be seen in the ERSST.v3b observational dataset (Fig. 12a) (Smith et al. 2008). Extreme

temperatures farther west in the equatorial Pacific are generally delayed by several months, exhibit much less seasonal variation, and are several degrees warmer overall. In the CM2.1 preindustrial simulation, despite a cold tongue which extends too far west and is too cold throughout the year, the general pattern of variability is simulated relatively well (Fig. 12b). Interestingly, this pattern is also qualitatively similar to the seasonal cycle in the zero eccentricity simulation (Fig. 12c), suggesting that much of the preindustrial seasonality in the eastern equatorial Pacific is not driven by eccentricity. Seasonality is stronger at preindustrial than in the zero eccentricity simulation, however, with SSTs that are up to ~0.5°C warmer during boreal winter and ~0.5°C cooler during boreal summer and autumn, suggesting that the timing of perihelion does influence the SST response to some extent. To explore this more fully, the remaining CM2.1 precession experiments are compared against the preindustrial simulation to see how precession affects the timing, magnitude, and character of the SST response (Fig. 13).

One of the simulations most similar to preindustrial in the timing of SST maxima and minima is WS (Fig. 13b), which is also the simulation with the most similar orbit: the orbital longitude of perihelion is 102.9° in the preindustrial simulation and 90.0° in the WS simulation. Since seasonality is stronger at preindustrial than in the zero eccentricity simulation, it is unsurprising to see that WS, where an increase in eccentricity is the primary change, has an even stronger seasonal SST cycle. Eastern Pacific SSTs are ~1°C warmer than preindustrial in boreal winter and up to ~1°C cooler than preindustrial in boreal

summer. Changes in the western Pacific are smaller in comparison, with the largest change being a warming of up to ~0.4°C in boreal spring. Compared to preindustrial, maximum and minimum SSTs generally occur a few weeks earlier in the year.

The VE simulation, with a longitude of perihelion of 180°, also displays a strengthening of the seasonal SST cycle, with maximum and minimum temperatures about a few weeks later in the year compared to preindustrial (Fig. 13c). Of any of the precession simulations, VE displays the largest eastern equatorial Pacific seasonality, with an amplitude >5°C between boreal spring and autumn. Since these simulations are limited to four distinct moments during the precessional cycle, however, it is unlikely that the longitude of perihelion which produces maximum seasonality has been simulated. Assuming that the magnitude of seasonality at each location follows a sinusoidal trend over the course of a full precession cycle (which is a simplification, but a useful one), then fitting the first harmonic of a Fourier series to the four simulations should reveal the longitude of perihelion which produces maximum seasonality at each location (Fig. 14). In the northern and southern extratropical Pacific Ocean, maximum SST seasonality occurs when perihelion reinforces the natural tilt-forced insolation cycle, which happens when longitude of the perihelion is near 270° (SS) in the Northern Hemisphere and 90° (WS) in the Southern Hemisphere. In the tropics, however, a more complex pattern emerges. Throughout most of the western Pacific warm pool, changes in longitude of the perihelion have only a small effect on the magnitude of seasonality. In the eastern Pacific there is a

mixed response from ~0-5°N, but a strong response just south of the equator, with maximum seasonality occurring with perihelion shortly before the vernal equinox. In the Niño 3 region, this corresponds with a longitude of perihelion of ~155°. In other words, maximum seasonality in that region should occur when the date of perihelion is roughly a month before NH vernal equinox. Because present day perihelion is slowly becoming later in the year, this simple analysis suggests that, if acting alone, precession would cause the eastern equatorial Pacific seasonality to slightly increase in strength over the next three millennia (calculation based on Berger 1978). However, the long-term decrease in eccentricity should negate this effect to some extent, and both factors will likely be negligible compared to the much more rapid effects of anthropogenic climate change.

In contrast with the WS and VE simulations, which generally have increased seasonality compared to preindustrial, the main response in the SS simulation is a shift in the timing of maximum and minimum SSTs (Fig. 13d). In the eastern equatorial Pacific, minimum SST occurs in January, a change of five months from the preindustrial simulation, while maximum SST occurs in May or June, a change of only one or two months from the preindustrial simulation, although a second local maximum occurs near the coast of South America in October.

The final precession experiment, AE, is the only one which displays reduced seasonality compared to preindustrial in much of the equatorial Pacific cold tongue (Fig. 15a). Relative to the preindustrial experiment, the eastern

equatorial Pacific in AE shows a cooling of up to ~2°C in April/May and a warming of ~2°C in September-November, flattening out the seasonal cycle to a large extent (Fig. 13a). Similar temperature variations also account for the increase in seasonality just north of and along the equator; the preindustrial seasonal cycle is weak in that region, so the temperature changes are actually big enough to reverse the timing of the seasonal cycle and strengthen its magnitude. Compared the eastern equatorial Pacific, temperature changes in the western Pacific warm pool are comparatively smaller in magnitude and a few months later in the year, despite the zonally uniform insolation forcing. This asynchronous temperature response between the eastern and western Pacific is present not just in AE-preind, but in all four precession experiments: almost without exception, temperature changes in the eastern equatorial Pacific are larger in magnitude and precede temperature changes in the west. This asynchronous response suggests that SST changes are not a simple thermodynamic response to changes in insolation everywhere in the equatorial Pacific. As a point of comparison, the next section explores the climate response to precession in the slab ocean model.

3.2.b. SM2.1 simulations

The SM2.1 lacks any vertical or horizontal ocean transport, so the climate response to precessional forcing is largely determined by atmospheric processes and surface fluxes alone. Because of this, a comparison between CM2.1 and SM2.1 results should help reveal the role of ocean dynamics in shaping orbitally-

forced climate response.

In the preindustrial and zero eccentricity simulations (Fig. 16b,c), the SST patterns are characterized by maximum eastern Pacific warmth during boreal spring and cooler SSTs during the latter half of the year. This temperature pattern closely matches observed SSTs in the ERSST.v3b temperature dataset (Fig. 16a), helped by the prescribed heat flux which approximates the real-world ocean heat transport. The equatorial Pacific SST pattern in the SM2.1 preindustrial simulation is generally more realistic than that in the CM2.1 preindustrial simulation, but it is unclear to what extent this difference in climatology between the two models affects the climate changes in perturbation experiments. Compared to the zero eccentricity simulation, preindustrial SSTs in the SM2.1 model are ~0.3°C warmer during boreal spring and ~0.2°C cooler during boreal autumn on average, with the sign of this temperature response being somewhat zonally uniform across the basin.

Compared to preindustrial, SST anomalies in each of the four remaining precession simulations are positive during the half-year beginning within approximately one month of perihelion and negative during the other half of the year (Fig. 17). Anomalies exceed 1°C in several experiments and are generally largest in the eastern Pacific or the western Pacific warm pool. The sign of the changes are somewhat zonally uniform across the Pacific, with the east and west Pacific appearing to respond directly to the orbital forcing. In the eastern Pacific, the WS experiment shows the largest increase in seasonality, SS shows the largest decrease in seasonality, and the two equinox experiments show shifts in

the timing of the seasonal cycle. Because the western equatorial Pacific has a relatively small seasonal cycle in the preindustrial simulation, these SST anomalies result in increased western equatorial Pacific seasonality in all experiments.

3.2.c. Comparison of CM2.1 and SM2.1 results

By comparing the CM2.1 (Fig. 13) and SM2.1 (Fig. 17) results, several important differences become clear. Most noticeably, eastern Pacific SST anomalies in the CM2.1 precession experiments are generally larger in magnitude and occur up to two months earlier in the year compared to SM2.1 results. CM2.1 anomalies show a distinct zonal asymmetry, while SM2.1 anomalies are much more zonally uniform, with comparatively smaller eastern Pacific SST anomalies. The models feature identical atmospheric models, so these differences should arise primarily because of the use of a full or slab ocean. While some of the change in timing may potentially be attributed to the models' differing values of mixed-layer depth, which is shallower in the east than the west equatorial Pacific in the CM2.1 but constant at 50 m in the SM2.1, analysis later in this paper suggests that surface heat fluxes are not the primary means of temperature change in the eastern equatorial Pacific. Therefore, the main response does not appear to simply result from differential lag to a zonally-uniform forcing. When looked at regionally, the strengthening and advanced timing of the eastern SST anomalies in the CM2.1 is more pronounced within a few degrees of the equator than in most of the subtropical and mid-latitude

Pacific, suggesting a robust mechanism in the equatorial ocean. SST anomalies in the western Pacific show less consistent, but still noticeable, differences between the CM2.1 and SM2.1 results.

Analysis of the cause of these differences in the following subsection will focus on the AE-preind experiment alone for the sake of simplicity. Aspects of the responses in the other precession experiments do not seem to simply be time-shifted versions of the AE-preind response (especially when comparing equinox and solstice experiments), but there are still considerable similarities. Additionally, because longitude of perihelion in the AE experiment (0°) is similar to the mid-Holocene (0.87°), the AE simulation provides an interesting analogue to a recent time period and will allow for better comparisons to CMIP5 models later on.

3.2.d. Mechanisms of change in the CM2.1 autumnal equinox simulation

To determine the cause of the asynchronous temperature response in the CM2.1 AE-preind experiment, surface heat fluxes as well as horizontal and vertical ocean heat fluxes over the upper 75m of the equatorial Pacific are considered. This top 75m should be deep enough to include climatically important thermocline processes but shallow enough to remain relevant to SST. Temperature changes in the top 75m are shown in Fig. 18a, revealing anomalies similar to the surface, and the change in total heat flux into this layer (i.e., the change in the time-tendency of layer heat content, due to both surface heat fluxes and interior ocean fluxes) is shown in Fig. 18b. The zonal asymmetry of

the total heat flux change, in contrast to the zonal uniformity of the TOA insolation change, reinforces the hypothesis that a simple thermodynamic response to changes in TOA insolation is insufficient to explain the entire SST response. To better diagnose the cause of these changes, a heat budget is useful.

The total heat flux can be broken down into the surface heat flux and the zonal, meridional, and vertical ocean heat fluxes (Fig. 19a,b,c,d). To a large extent, the heat fluxes in the western Pacific warm pool are dominated by the surface heat flux, suggesting that temperature changes in the western Pacific can be primarily explained as a direct thermodynamic response to changes in insolation. Surface fluxes become much smaller in the east, however, failing to account for much of the temperature change in that region.

To explain the pronounced reduction in surface heat flux in the eastern Pacific, surface flux is further broken down into changes in net shortwave (SW) radiation, net longwave (LW) radiation, sensible heat flux, and latent heat flux (Fig. 19e,f,g,h). This breakdown shows that SW radiation and latent heat flux are the largest terms, while LW radiation and sensible heat flux are comparatively small. The explanation for reduced surface heat flux in the eastern equatorial Pacific is two-fold. First, an increase in high clouds in the eastern equatorial Pacific and a decrease in clouds in the western equatorial Pacific during boreal autumn allows less SW radiation to reach the surface in the east compared to the west. Second, the SW which does make it to the surface is largely balanced by changes in latent heat flux. As changes in latent heat flux are primarily a result of

SST change, however, with warmer waters losing more heat to evaporation, the latent heat flux term should be considered a response rather than a forcing. Therefore, changes in SW radiation contribute to, or at least maintain, SST anomalies. However, SW heat fluxes occur too late in the year to account for the initial changes in eastern equatorial Pacific SST, so other parts of the heat budget must be analyzed to determine the primary cause of the SST anomalies.

The remaining three aspects of the heat budget – changes in zonal, meridional, and vertical ocean heat fluxes (Fig. 19b,c,d) – all affect ocean temperature in different ways. In the eastern equatorial Pacific, the largest fluxes are due to the vertical heat flux (occurring earlier in the year and closer to the coast of South America), but significant fluxes also occur in the zonal and meridional directions. The following analysis suggests that these fluxes occur by means of an equatorial thermocline signal propagating from the west, which likely originates through two mechanisms: changes in the strength of the subtropical anticyclones associated with monsoonal heating anomalies, and shifts in convection over the Maritime Continent and western Pacific region.

In the AE-preind experiments, subtropical anticyclones in the Pacific and Atlantic Oceans are generally weakened in May and strengthened in November. While this change is more pronounced in the CM2.1 model, changes of the same sign are seen in most regions in the slab ocean model, indicating that at least part of this response is not driven by ocean dynamics. According to Rodwell and Hoskins (2001), differential heating of land and ocean in monsoon regions can remotely affect the strength of subtropical anticyclones, with boreal summertime

winds in the equatorial Pacific responding largely to heating in the Asian monsoon region. In the AE-preind experiments, weakened subtropical anticyclones in May appear to result in westerly wind anomalies in the western equatorial Pacific, while strengthened subtropical anticyclones in November result in easterly anomalies. Detailed analysis of the effect of precession on subtropical anticyclones can be found in Mantsis et al. (2013).

On a more local scale, there appears to be an enhancement of the anomalous flow in the western equatorial Pacific associated with shifts in convection. The present-day monsoonal circulation over the Maritime Continent is characterized by a largely annual component of rainfall and a somewhat weaker semi-annual component, with the annual cycle resulting primarily from the interaction of the seasonally reversing monsoonal winds with the terrain of the Maritime Continent (Chang et al. 2005). In the AE-preind experiment, changes in local insolation appear to affect this circulation pattern. In boreal spring, reduced insolation cools the Maritime Continent more than the western Pacific warm pool, shifting convection from the Maritime continent toward the western Pacific and enhancing the westerly wind anomalies mentioned above. In November, convection is shifted from the South Pacific Convergence Zone toward Australia and the Maritime Continent. Temperature, precipitation, and wind anomalies are shown in Fig. 20, and the anomalous diabatic heating of the atmosphere, which is heavily influenced by changes in convection, is shown in Fig. 21. Positive heating anomalies correspond well with areas of wind speed convergence and vise versa. Other mechanisms may be partially responsible for

these zonal wind anomalies as well, but as of yet remain undiagnosed in this research.

Because the Coriolis parameter changes sign across the equator, anomalous westerly winds in May promote convergence of surface water and anomalous downwelling along the equator, deepening the local thermocline and resulting in a positive temperature anomaly at depth (Fig. 22c). This warm anomaly propagates eastward along the thermocline, possibly influenced by Kelvin waves, and surfaces in the east in boreal summer, warming SSTs in the eastern equatorial Pacific (Fig. 22d,e). Anomalous easterly winds result in an analogous cold response which propagates along the thermocline during boreal autumn and winter (Fig. 22f,a,b).

Because the equatorial temperature anomaly only takes about five months to traverse the Pacific, a cooling in the west Pacific can result in a warming in the eastern equatorial Pacific before local insolation anomalies would produce warming. These equatorial temperature signals partially explain the calculated zonal and vertical ocean heat fluxes, which together account for a large part of the total heat fluxes in the eastern equatorial Pacific. In short, while SST changes in the western Pacific warm pool are driven more by the direct thermodynamic effect of insolation changes, SST changes in the eastern equatorial Pacific are primarily a response to wind anomalies due to changes in the Pacific subtropical anticyclones as well as shifts in convection near the Maritime Continent, which work to transmit temperature anomalies to the east as equatorial thermocline signals. Insolation changes in the eastern Pacific reinforce this initial change,

resulting in the large amplitude and asynchronous timing of eccentricity-driven SST anomalies in the eastern equatorial Pacific. Because the SM2.1 model lacks this oceanic advective heat transport, changes in SST in that model are primarily a direct thermodynamic response to insolation anomalies, resulting in more zonally uniform SST anomalies across the Pacific. These results are similar in part to that of Luan et al. (2012), but a more complete mechanism to explain the wind anomalies is presented here.

3.3. Effects of obliquity on equatorial Pacific seasonality

Current hypotheses for the cause of the present day equatorial Pacific seasonal cycle, mentioned in section 1, suggest that much of the cycle ultimately stems from the seasonal shifts in the insolation gradient at the equator, which are determined by the obliquity of the Earth. It is interesting, therefore, to see how much the seasonal temperature cycle might respond to the ~2.4° shifts in obliquity which have occurred over the past 600 kyr. To investigate this relationship, simulations with low and high obliquity are explored.

A change in obliquity from high (24.480°) to low (22.079°) obliquity results in reduced summer insolation and slightly increased winter insolation in the mid-latitudes of both hemispheres. The change in annual-mean insolation is -13.2 W m^{-2} over the polar regions and +3.2 W m^{-2} in the tropics. However, despite this increased equator-to-pole insolation gradient, changes to equatorial Pacific seasonality are relatively small in both the CM2.1 and SM2.1 experiments, consisting of a few tenths of a degree warming from approximately October-May

and a cooling during the remainder of the year in the CM2.1. Spatially, this is a slight decrease in seasonality throughout much of the tropical Pacific in the CM2.1, with a small increase confined to eastern equatorial Pacific and part of the western Pacific warm pool (Fig. 15b). In the CM2.1, decreases in seasonality become larger away from the equator due to the reduced seasonal insolation cycle in both hemispheres.

Compared to changes in equatorial Pacific seasonality driven by precession (Fig. 15a), the obliquity-driven anomalies are quite small, suggesting that changes in obliquity over the past 600 kyr have played little role in altering equatorial Pacific seasonality. While the tilt of the Earth undoubtedly determines much of the present-day equatorial Pacific seasonality, this response does not appear to be very sensitive to the small obliquity variations that occurred in the recent past. Larger obliquity variations might be capable of producing large changes in equatorial Pacific seasonality, but as the Earth system is currently incapable of obliquity variations outside of the range ~22.1°-24.5°, larger changes in obliquity have not been analyzed in this dissertation.

3.4. Comparison with CMIP5 6ka results

The idealized orbital experiments conducted with the GFDL CM2.1 and SM2.1 suggest that changes in longitude of the perihelion can produce large changes in equatorial Pacific seasonality, driven primarily by local insolation anomalies and the transport of heat anomalies from the western Pacific as equatorial thermocline signals. To test this mechanism of precession-driven

seasonality change, a mid-Holocene experiment from the CM2.1 was compared against output from the following 10 CMIP5 models: BCC-CSM1.1, CCSM4, CNRM-CM5, CSIRO-Mk3.6.0, GISS-E2-R, HadGEM2-ES, IPSL-CM5A-LR, MIROC-ESM, MPI-ESM-P, and MRI-CGCM3. These 10 CMIP5 models were the ones with all necessary data publically accessible at the time of this research. All results were analyzed as 100 year monthly-mean climatologies. The mid-Holocene (6ka) is analyzed because it presents an approximate analogue to AE; Ice sheets and atmospheric composition are similar to AE and perihelion is very close to the autumnal equinox (longitude of perihelion is 0.87° vs. 0° at AE), although 6ka simulations have increased obliquity compared to the AE simulation (24.1° vs. 23.4°) and eccentricity is more similar to present day. Using these 6ka experiments, the mechanism which explains changes in seasonality in the CM2.1 precession experiments may be tested for robustness in 10 CMIP5 models.

In the GFDL CM2.1 results, the 6ka-preind experiment produces results similar to the AE-preind experiment. SSTs in the eastern equatorial Pacific are up to ~1°C cooler from approximately January to June and up to ~1°C warmer during the rest of the year. SST changes in the western Pacific warm pool generally show a slight cooling. An analysis of the heat budget reveals that, like AE-preind, western Pacific changes are largely a direct thermodynamic response to insolation changes, while eastern equatorial Pacific SSTs respond to eastward-propagating thermocline signals reinforced by local insolation changes. Changes in winds near the Maritime Continent result in the thermocline signal propagation (Fig. 23a,b,c,d,e,f), similar to the AE-preind experiment.

SST changes in the 10 model CMIP5 ensemble are similar to those in the CM2.1, though generally smaller in magnitude. Eastern equatorial Pacific SSTs are up to 1°C cooler from December-June and up to 0.5°C warmer from July-November. West Pacific SSTs show a slight cooling throughout the year. The CMIP5 ensemble has a decrease in seasonality in the eastern equatorial Pacific of up to 1.5°C, compared to 2°C in the CM2.1 experiment.

As in the CM2.1 experiment, the CMIP5 ensemble shows zonal wind changes in the western equatorial Pacific. Anomalous westerly winds in boreal spring create a warm thermocline signal that travels east along the thermocline (Fig. 23e,f,g) while anomalous easterly winds in boreal autumn create a cold signal (Fig. 23h,i,d). These temperature anomalies, coupled with the thermodynamic effect of local insolation forcing, lead to the SST changes in the eastern equatorial Pacific. Among the individual models, there is some variation in this response, but all 10 models show a weakening of the seasonal cycle over much of the eastern equatorial Pacific and 9 of the models show anomalous westerly winds during boreal spring and anomalous easterly winds during boreal autumn in at least some of the western equatorial Pacific. The one model which does not match this pattern (MIROC-ESM) has anomalous easterly winds year-round in the western equatorial Pacific, though the anomalies are stronger in boreal autumn than in boreal spring. This model has the most zonally uniform seasonality change of any of the models, offering further evidence that the thermocline signals affect seasonality primarily in the eastern Pacific.

This general consensus between the CM2.1 and these 10 CMIP5 models

suggests that the ocean response to orbital forcing is not overly model dependent. Furthermore, it lends support to the hypothesis that precession affects equatorial Pacific seasonality not just through the direct thermodynamic effect of insolation anomalies, but by means of thermocline signals traveling at depth from the west Pacific.

3.5. Discussion

Changes in equatorial Pacific seasonality due to orbital forcing may have implications in several areas. First, teleconnections should be analyzed. Because equatorial Pacific teleconnections are strong in the present day climate, it is possible that teleconnections from equatorial Pacific seasonality explain some of the Earth's climate response to precession. However, if changes in equatorial Pacific seasonality are producing a remote response, it is possible that the signal is obscured by the direct climate response to local insolation changes in those regions or by teleconnections from other regions. Experiments in which equatorial Pacific seasonality is prescribed but no direct forcing is applied to other climate regions would be ideal to investigate this, but such experiments are beyond the scope of this dissertation.

Another implication of this work concerns the study of paleo variations, which are helping to constrain projections of future tropical Pacific climate and ENSO (Wittenberg 2009; Vecchi and Wittenberg 2010; Emile-Geay et al. 2013a,b; McGregor et al. 2013). Because precession can result in significant changes to equatorial Pacific seasonality at the same time that ENSO variations

are occurring, and because these changes may even be related (Luan et al. 2012), scientists must be careful to distinguish one from the other. Proxy records which only reveal changes in extreme temperature events, but lack the time-resolution necessary to isolate year to year variations, may be insufficient to distinguish between enhanced ENSO and enhanced seasonality, or a combination of the two. For example, a core which shows a temperature distribution similar to today may either be showing a climate similar to today or the offsetting effects of opposite changes in seasonality and ENSO. Because of this, it is important that proxies that show year to year variations (e.g., sediment cores in areas with high sedimentation rates) are used rather than proxies with lower temporal resolution. Alternately, Fig. 14 of this dissertation, which shows regional sensitivity of SSTs to precessional changes, may be useful for the selection of proxy locations. Cores taken from areas with large sensitivity to precession-forced seasonality changes, such as the eastern Pacific cold tongue, may be less ideal for studies of ENSO variation due to the potential for confusion between the two signals. Instead, areas where the influence of precession on seasonality is low, but the standard deviation of interannual temperature change is high (see Fig. 14 in Wittenberg et al. 2006), may be better suited for studies of paleo ENSO. While there is unfortunately some overlap of regions where both of these quantities are high, parts of the central Pacific, or even the eastern Pacific north of the equator, may be good regions for this purpose, barring other shortcomings of those locations.

As a final note, biases in the CM2.1's simulation of the equatorial Pacific,

such as the existence of the double ITCZ (which persists in the orbital simulations), may potentially influence the climate response to orbital forcing. Simulations with models which have reduced biases would help alleviate uncertainties in this regard.

4. WATER TABLE AND SOIL MOISTURE

This section focuses on the response of the water table and soil moisture to orbital forcing. Section 4.1 discusses the experimental design. Section 4.2 examines some characteristics of the CM2.1 and water table model, and section 4.3 explores the response of water table and soil moisture to orbital forcing, focusing on similarities and differences between the two quantities. Section 4.4 provides additional discussion of the response of tropical wetlands, and section 4.5 addresses advantages and shortcomings of each modeling approach.

4.1. Experimental Design

The GFDL CM2.1, like many other coupled GCMs, uses a bucket type groundwater model (Anderson et al. 2004), so it is paired with the water table model described in Fan and Miguez-Macho (2010) to better explore the response of groundwater to orbital forcing. Lo and Hi obliquity CM2.1 simulations are analyzed, as well as AE, WS, VE, and SS precession simulations. These precession simulations were run on a slightly older version of the CM2.1 than those described in section 2.1, but climate results between the two sets of simulations appear to be similar. Some features of the obliquity simulations have been explored in Mantsis et al. (2011), Erb et al. (2013), and Erb et al. (in preparation), while these precession simulations have been studied in Mantsis et al. (2013). The newer set of precession simulations are examined in Erb et al. (2013) and Erb et al. (in preparation). In addition to these idealized simulations,

modern and 6ka simulations will be looked at to some degree. Orbital parameters used in all of these simulations can be seen in Table 1.

Output from the CM2.1 simulations was used to drive the water table model. Recharge, which is calculated according to equation 3 below, and winter surface air temperature, which helps determine soil freezing characteristics and therefore ground permeability, are the only two forcings which vary between simulations.

$$Recharge = recharge_{modern} + \left[(precip - evap)_{pert} - (precip - evap)_{control}\right] \quad (3)$$

The $recharge_{modern}$ field in equation 3 is an average of two Döll-Fiedler datasets (Fan et al. 2013, supplemental materials; Döll and Fiedler 2007), and is used to drive the modern water table simulation shown in this dissertation. Some features of this modern simulation were explored in Fan et al. (2013). To calculate the recharge used in the other simulations, the change in precipitation-evapotranspiration (P-E) between perturbation and modern CM2.1 simulations is added to the $recharge_{modern}$ field. This calculation was performed instead of simply calculating recharge as precipitation-evapotranspiration-surface runoff (Fan and Miguez-Macho 2010) because the CM2.1 does not distinguish between surface runoff and groundwater discharge. On the other hand, P-E alone gave values that would make recharge unrealistically high. After calculating recharge with equation 3, negative recharge was regarded as zero by the water table model (H. Li, personal communication).

Changes in sea level and topography can also be used to influence the water table model, but these variables were not changed in the present water

table simulations. Some commentary about the possible roles of these forcings on influencing the water table will be given in section 4.5.

The model was run at coarse, then medium, then fine vertical resolution, with a horizontal resolution of 30 arc seconds, which made grid cells just smaller than 1 km by 1 km at the equator (Fan et al. 2013). While not all grid cells had reached equilibrium by the end of these simulations, the number of grid cells still out of equilibrium in the largest domain appeared to have leveled off to an acceptable degree.

For the modern simulation, Fan et al. (2013) found that the water table model results are fairly consistent with global wetland distribution. At higher resolutions, the model may be able to capture smaller wetlands as well (Fan and Miguez-Macho 2010). It should be noted that the experimental design used in this section is only a first order approach to modeling wetlands with a water table model. Since the water table model is not fully coupled to the CM2.1, but rather driven by it, the resultant water table is not capable of having any effect on the atmosphere through evapotranspiration or other mechanisms. Full, two-way coupling of this model to a GCM is not done in the current research.

4.2. Groundwater in the GFDL CM2.1 and water table model

The land model in the CM2.1 is based on a model described in Milly and Shmakin (2002), with additional changes described in Anderson et al. (2004). Land water is divided into water frozen as snow, water at the “root zone”, and deeper groundwater. Water may enter this system as liquid precipitation or

snowfall, and may leave through evapotranspiration (including sublimation) or through groundwater discharge. Snow can melt into root zone water, excess water in the root zone drains into the groundwater once the root zone volume is full, and groundwater discharges to the ocean in proportion to the amount of groundwater (Fig. 1 in Milly and Shmakin 2002; Anderson et al. 2004). Soil consists of 18 vertical levels down to a depth of 6 m, increasing in thickness from 0.02 m to 1 m as depth increases. Both sensible and latent heat are simulated at almost all of these levels (Anderson et al. 2004).

P-E, root zone water, groundwater, and snow are shown for a modern CM2.1 simulation in Fig. 24. P-E is a net positive over most continental regions (Fig. 24a), since runoff is a positive quantity, while ocean regions (not shown) are generally negative over much of the low latitudes outside of the ITCZ, as they tend to provide a large source of water to the atmosphere. The liquid part of the water flux to the land can initially be stored in the root zone water (Fig. 24b), which shows large values in the mid and high northern latitudes and in regions of high P-E in the tropics and subtropics, with root zone water having an average value of 43.5 kg m^{-2} in the tropics in this simulation. Groundwater values match reasonably well with regions of high P-E (Fig. 24c). Snow has its largest values over the northern high latitudes, some mountain ranges, and most noticeably over Antarctica and part of Greenland (Fig. 24d).

In the water table model, the water table is forced with annual-mean recharge and winter surface air temperature (Fig. 25), among other things, and the model adjusts each cell toward a balance between recharge, horizontal

transport of water, sea level height near the coasts, and discharge when the water table rises above the land surface (Fig. 4a in Fan and Miguez-Macho 2010). Water table depth for a modern simulation is shown in Fig. 26a, with a more detailed view for part of North America in Fig. 26b. A comparison between results from this simulation and observations from across the globe can be found in Fan et al. (2013).

One point of comparison is in the differences in model resolution, as seen in the topography in Fig. 27. CM2.1 resolution is 2.5° longitude by 2° latitude, while horizontal resolution in these water table model simulations is less than 1 km (Fan et al. 2013), which lets the water table model have a much more realistic topography and allows finer features in the groundwater to be resolved. This difference, as well as other differences mentioned in the introduction, should be kept in mind when comparing the responses of these two models to orbital forcing in the next section.

4.3. Response to orbital forcing

To explore the response of soil moisture and the water table to orbital forcing in these two models, three idealized orbital experiments are examined. The first is low obliquity minus high obliquity (Lo-Hi), which spans the range of obliquity values over the past 600,000 years (Berger and Loutre 1991). The other two are perihelion at NH autumnal versus vernal equinox (AE-VE), and perihelion at NH winter versus summer solstice (WS-SS), which look at different aspects of the precession cycle.

Because the CM2.1 and water table model output different land water variables -- mass of water per square meter for different regions in the CM2.1 and water table depth in the water table model -- a direct comparison between identical variables is not possible. Instead, the primary quantities that will be analyzed are “root zone” water for the CM2.1 and, in the water table model, the percentage of grid points with water level shallower than 50 cm in each 2° by 2.5° box (the same resolution as the CM2.1) or, later in this section, each 1° by 1° box, to show more detail. This water table quantity will hereafter be called “shallow water table coverage”. A depth of 50 cm was chosen because it appears to be a good cutoff for wetlands. Lehner and Döll (2004) compile a number of sources to create a map of global lakes, reservoirs, and wetlands and find that global wetland coverage of non-glaciated land is 6.2-7.6%, with lakes additionally covering as much as 2.4%. Including estimates of even smaller lakes could increase that percentage even more (Downing et al. 2006). In the modern simulation, 9.6% percent of the water table is shallower than 50 cm, which is approximately in line with those numbers. Although deeper groundwater also plays a role in the climate system, this research focuses on shallow water, which is important for atmosphere interactions and vegetation. Because of the difference in these variables, a one-to-one correspondence is not expected, and it is unclear to what degree these two variables should be similar. Patterns of change, rather than exact values, will be the focus of much of this analysis.

Annual-mean changes in P-E, root zone water, and shallow water table coverage are shown for the Lo-Hi experiment in Fig. 28. Lowered obliquity results

in an annual-mean increase in insolation at low latitudes and a decrease at higher latitudes, with a decrease in seasonality in both hemispheres. In the tropics, the change in meridional insolation gradient results in a slight strengthening of the Hadley circulation averaged over the year, mentioned in section 2. P-E is generally increased at the equator and reduced in the outer tropics and subtropics, with smaller P-E changes in the mid-latitudes. Root zone water (Fig. 28b) increases along the equator and decreases off the equator, but relatively large increases in root zone water are also seen in North America, eastern Europe, and northern Asia, in contrast to the relatively modest changes in annual-mean P-E there. In comparison, the largest changes in shallow water table coverage (Fig. 28c) are reductions over northern Africa and other parts of the subtropics. Increases along the equator and in the northern middle and high latitudes are generally smaller.

In the two precession experiments, changing the date of perihelion primarily has an effect on the seasonal cycle of insolation. In the AE-VE experiment, changing perihelion from the NH vernal to the NH autumnal equinox results in increased insolation for the half-year centered on the autumnal equinox and reduced insolation for the rest of the year. Analogous changes occur in the WS-SS experiment. Like in the Lo-Hi experiment, global, annual-mean insolation change is 0 W m^{-2} for both the AE-VE and WS-SS experiments.

The largest precipitation changes in the precession experiments are associated with stronger or weaker monsoon circulations in the tropics and subtropics, most notably over Africa, where annual-mean P-E anomalies may

reach magnitudes of 1.5 mm day^{-1} or more (Fig. 29). The largest anomalies are in WS-SS, in which insolation changes generally weaken the seasonal temperature cycle in the NH and strengthen it in the SH, leading to weaker NH monsoons and stronger SH monsoons (Table 3). The changes in root zone water and shallow water table coverage in the AE-VE and WS-SS experiments are broadly consistent with these changes in precipitation, although changes in shallow water table coverage appear to be more confined to places where the water table is closer to the surface (Fig 26a). Changes in root zone water are relatively high in the NH mid and high latitudes, but the reason for this is not clear at this time.

It should be noted that the changes in P-E shown in the figures are not identical to the changes in recharge as felt by the water table model. This is due to the calculation of recharge. Any grid cells which would have negative recharge according to equation 3 have zero recharge instead, since negative recharge would imply that the area is a net source of water, which is unrealistic for a long term average over land (H. Li, personal communication). While this difference does not reverse the sign of changes, it can reduce the magnitude of changes, so it should be kept in mind when comparing changes in root zone water and shallow water table coverage. Changes in recharge are not shown, but look relatively similar to the maps of changes in P-E in most areas.

In these experiments, P-E anomalies do not always lead to root zone water and shallow water table coverage anomalies of the same sign. To better show these differences, Fig. 30 maps the regions where the sign of changes are

consistent or inconsistent with P-E. Maps are separated into regions of positive (or zero) change in P-E (Fig. 30, left column) and negative change in P-E (Fig. 30, right column). Regions where changes in P-E, root zone water, and shallow water table coverage are all the same sign are shaded gray. Places where only root zone water is different are blue, places where only shallow water table coverage is different are red, and places where both are different from P-E anomalies are black. A breakdown of the spatial percentage of each case is given in Table 4.

In general, changes in root zone water and shallow water table coverage are mostly consistent with changes in P-E, with areas where all three are positive representing 38.5% of all cases and areas where all three are negative representing 31.0% of all cases among the three experiments. In regions where differences in sign do appear, the mean P-E anomaly is smaller than in regions where all signs are the same. Averaged across all three experiments, the mean magnitude of P-E anomalies is 0.29 mm day^{-1} in regions of where all three quantities have the same sign and 0.13 mm day^{-1} in regions where at least one differs in sign. This difference in means suggests that if P-E anomalies are high, root zone water and shallow water table coverage typically have the same sign as changes in P-E, regardless of other factors at work in these experiments. However, the reasons for the differences in sign are still worth exploring.

Some of the differences between P-E anomalies and root zone water anomalies (ignoring the water table for now) may be attributed to the seasonal timing of P-E anomalies relative to the water capacity of the root zone in the

model. While only annual-mean values are analyzed in Figs. 28, 29, and 30, root zone water responds to the seasonally varying changes in P-E. If P-E anomalies are positive for part of the year and negative for another part, the annual-mean sign of the response can be determined by how much more water the root zone bucket can hold. For example, a large increase in P-E in a season where root zone water is already near its maximum value (i.e. the “bucket” is nearly full) will not lead to large changes in root zone water due to the extra water being drained into the deeper groundwater, and smaller decreases in another time of year may lead to a larger change. Likewise, if a decrease in P-E occurs in a season where P-E already exceeds the root zone water capacity, this decrease will not be fully reflected in the change in root zone water. In both of these cases, some of the P-E anomaly will be transferred to the deeper groundwater instead. When comparing P-E anomalies to the sum of root zone water and groundwater anomalies, the signs are generally more similar (not shown). However, deeper groundwater is not the focus of this section because, while it influences the climate system by way of freshwater river discharge into oceans, it does not exchange water and energy fluxes with the atmosphere at the land surface (Anderson et al. 2004), which is of more interest in this research.

When looking at the shallow water table coverage, the sign of anomalies differ from P-E anomalies in 11.5% of cases across the three experiments (compared to 23.3% of regions where P-E and root zone water anomalies differ). Because the water table is driven by annual-mean recharge values, seasonal changes in P-E cannot be the explanation for these changes in sign. While a

seasonal recharge forcing would be more realistic, the current version of the water table model focuses on long-term average values rather than having an annual cycle (Fan and Miguez-Macho 2010). Instead, other features must account for these differences. One such feature is relief, which has a mean value of 0.0250 in regions where the signs of P-E and shallow water table coverage anomalies are consistent, but 0.0301 where the signs are not consistent (Table 5). This finding suggests that changes in shallow water table coverage are generally less likely to respond with the same sign as changes in P-E in areas with a steeper slope. To look at this another way, Table 6 divides mean 2° by 2.5° relief into six ranges, and the percentage of grid cells with inconsistent signs is given for each range. This shows minimum inconsistencies in the lowest relief range and, except for somewhat large values in the 0.005-0.01 range, a general trend toward a higher percentage of inconsistencies at higher reliefs. Because steeper slopes should lead to higher rates of horizontal water transport (Fan et al. 2007), this difference could point to a greater influence from changes in P-E in nearby upslope regions. Other land properties which might explain some of the differences are topographic elevation, saturation conductivity, which depends on ground properties, and hydraulic conductivity e-folding depth, which describes the rate of decrease of hydraulic conductivity with depth (H. Li, personal communication; Fan et al. 2013, supplemental materials) (Table 5). These three quantities do show some differences, most notably in the case of hydraulic conductivity e-folding depth, which has a smaller mean value in regions with differences in sign. Future analysis into the potential mechanisms of interaction

between the water flux and these properties should help determine if these differences are meaningful.

Scatter plots comparing root zone water anomalies (x axis) and shallow water table coverage anomalies (y axis) are shown in Fig. 31. Colors show changes in P-E. The Lo-Hi experiment, which has smaller changes in P-E, has the most condensed scatter plot, while WS-SS, which has significant monsoon changes associated with changes in the strength of the season insolation cycle, shows the largest anomalies. In each of these scatter plots, the correlation between changes in root zone water and shallow water table coverage is positive. Correlation (r) values are 0.31 for Lo-Hi, 0.35 for AE-VE, and 0.44 for WS-SS, with the experiments with larger anomalies having larger correlation values (Table 7). These scatter plots appear to show two types of response: one in which small changes in root zone water correspond to large changes in shallow water table coverage, and one where the opposite is true. This may be seen most strongly in the WS-SS scatter plot, which appears to show points clustered along two different lines, one with a high slope and one with a low slope. The reason for this apparent duel response appears to relate to the mean depth of the water table. In regions with a deep water table, large changes in P-E can result in large changes to root zone water without correspondingly large changes in shallow water table coverage. On the other hand, if the water table is near the 50 cm value used to distinguish shallow wetlands, a P-E anomaly which does not produce large root zone water changes may still produce shallow water table coverage anomalies. Further research is needed to validate this and better

explore these relationships.

Correlation values between changes in P-E and root zone water, and between changes in recharge and shallow water table coverage, are given in Table 7. In both cases, mean correlation values are 0.50, suggesting noticeable, but not exact, correlations. Zonal-mean changes in both of these quantities, smoothed with a 5° boxcar filter, are shown in Fig. 32. Since these are different quantities, the magnitude of values in Fig. 32 should not be compared directly. The zonal-means show fair degrees of similarities and differences.

With this comparison done, the following section looks at changes in the water table at low latitudes, due to the importance of tropical wetlands to past climate changes.

4.4. Response of tropical wetlands to orbital forcing

Wetlands may be divided into three simple categories based upon their general location: high latitude, boreal wetlands, where permafrost can keep soils from draining; tropical wetlands, which form due to high precipitation rates; and coastal wetlands, which receive water from rivers and are maintained by the influence of sea level on the water table (Bartlett and Harris 1993; Fan and Miguez-Macho 2010; Fan, personal communication). Of these, high latitude wetlands respond largely to changes in glacial extent, and coastal wetlands are influenced by changes in the sea level. While both of these processes are important in paleoclimate, neither are altered in the idealized orbital experiments, so this section looks at changes in tropical wetland alone, which vary with

changes in P-E. Because methanogenic bacteria in wetlands are the largest natural emitter of methane, and because some methane variations in ice cores occur at the periods of precession and obliquity (Loulergue et al. 2008; Spahni et al. 2005; Ruddiman 2003), changes in tropical wetlands caused by orbitally-induced changes in the ITCZ and monsoons may have had a role in driving some past climate changes (Loulergue et al. 2008).

Methane increased significantly between the last glacial maximum (LGM) and mid-Holocene. Though other mechanisms might account for some of the change, an increase in the size of tropical wetlands is a good candidate to explain this methane increase (Chappellaz et al. 1993a,b; Blunier et al. 1995). To test the response of the water table model to mid-Holocene forcing, changes in modeled shallow water table coverage at the mid-Holocene are compared against observations from the Global Lake Level Status Grids (Viau and Gajewski 2001). The Global Lake Level Status Grids dataset classifies lake height relative to the total range of each lake's variability, with a value of 1 being relatively low and 3 being relatively high (Viau and Gajewski 2001). The difference between 6ka and 0ka reconstructions is compared against the difference between 6ka and modern simulations run with the water table model (Fig. 33). Because the modern water table simulation was conducted using Global Land Data Assimilation System (GLDAS) temperature data (Fan et al. 2013, supplemental materials) and the 6ka simulation uses CM2.1 output, the experimental design is not consistent here, so these results should be taken with a grain of salt. Despite this, the 6ka simulation is interesting because it

represents an actual period in the Earth's past. Unlike the idealized orbital simulations, which are interesting for other reasons, the 6ka simulation may be compared against proxy records and can be used to more directly study past changes in the climate system.

When comparing the 6ka experiment with the Global Lake Level Status Grids reconstructions, a few similarities and differences can immediately be observed. Increased wetness over northern Africa in the reconstructions coincides with the increase in the shallow water table coverage in the model results. Similar increases over the Himalayas are observed, with decreases over parts of Canada. More subtle changes over Europe are also relatively consistent between the model and reconstruction. However, the model shows decreases in shallow water table coverage over much of South America, southern Africa, and Australia, places where the reconstruction generally shows increases. While the spatial coverage of the reconstruction is somewhat limited in the SH, this mismatch is apparent. The reasons for this inconsistency are unclear.

Looking more broadly, Fig. 34 shows shallow water table coverage in the tropics for eight simulations individually: the modern and 6ka simulations, as well as the six idealized orbital simulations explored in the last section: Lo, Hi, AE, WS, VE, and SS. The mean tropical shallow water table coverage for each simulation is listed on each panel. A comparison between the modern and 6ka simulations shows a distinct increase in the extent of shallow water table coverage over northern Africa at 6ka. Decreases in shallow water table coverage at 6ka occur over parts of South America, southern Africa, and over Indonesia

and the surrounding landmasses, as was seen in the previous figure. Net changes in the 6ka simulation are still positive, with shallow water table coverage at 9.3% at modern, but 10.0% at 6ka.

In the obliquity simulations, the primary change is decreased shallow water table coverage in northern and southern Africa at low obliquity. Land areas near the equator show a slight increase in shallow water table coverage, which can also be seen in the zonal mean changes in Fig. 32a, but the mean change over the whole tropics is still negative: 9.8% at high obliquity compared to 8.9% at low obliquity.

The precession simulations also show large changes in the shallow water table coverage, especially over Africa, northern Australia, and parts of South America. The shallow water table coverage in AE (and SS, to a lesser degree) is similar to the extent at 6ka. Because longitude of perihelion in these two experiments is similar (0° in AE vs. 0.87° in 6ka), this suggests that precession may have played a large role in determining wetland extent at the mid-Holocene. In general, the shallow water table coverage in the precession experiments shows something of a cycle in the tropics, with largest extents in the northern tropics in the SS and AE simulations and largest extents in the southern tropics in the WS and VE simulations. Averaged over the whole tropics, the largest values for shallow water table coverage occur in the SS simulation, with mean values decreasing in AE, then WS, then VE. Interestingly, the range in values for tropical mean shallow water table coverage in the precession simulations (8.7% to 10.2%) is larger than that in the obliquity simulations (8.9% to 9.8%). The

European Project for Ice Coring in Antarctica (EPICA) Dome C ice core shows stronger methane variations at the period of obliquity than at the periods of precession (Loulergue et al. 2008), but the present results suggest that, at high eccentricity, precession can potentially have a greater effect on tropical wetland extent. Between 150 and 75 kya, precession signals have been observed in proxy records from African lakes (Scholz et al. 2007), which is near regions of pronounced water table variability in these experiments.

4.5. Discussion

Comparison of the root zone water in the CM2.1 and shallow water table coverage in the water table model reveals large regional similarities but also some differences. The CM2.1 model shows relatively large changes of root zone water in mid and high latitudes compared to the shallow water table coverage anomalies, though further research is needed to understand these regional responses. When considering seasonal differences, the bucket nature of the land model causes some P-E anomalies to be drained into the groundwater. The CM2.1's deeper groundwater region does not have a direct effect on land surface fluxes, and is simply discharged into the ocean in proportion to its amount. Additionally, the lack of lateral transport keeps the CM2.1 root zone water and groundwater from being affected by P-E anomalies in neighboring grid cells, a mechanism which appears to affect results in the water table model, influencing the sign of the response more in areas of high relief. On the other hand, the CM2.1 groundwater responds to seasonal changes, interacts with the

atmosphere in a fully coupled manner, and does not require the running of additional model simulations.

The water table model has some benefits and negatives of its own. Being driven by annual-mean recharge values means that it cannot respond to seasonal variations, which may be important to the annual-mean response in areas with highly seasonal precipitation patterns. The water table model is also not fully coupled to a GCM in these simulations and it is computationally expensive to run. However, because this model contains the effect of a water table and lateral transport of water, among other things, it presents a more realistic approach to modeling the water table.

The water table model should also be better suited to modeling groundwater response when changes in topography or sea level are applied. The sea level affects coastal wetlands by keeping the coastal water table near the land surface (Fan and Miguez-Macho 2010). Between the LGM and today, sea level has varied by over 100 m (Lambeck and Chappell 2001), due mostly to the retreat of ice sheets, but also due to the slight expansion of water under warmer temperatures. Future melting of ice sheets and thermal expansion of the oceans under anthropogenic warming will likely lead to further changes in the sea level and coastal water table. Because the coastal water table can respond to sea level changes, the water table model is equipped to respond to this kind of forcing. On a long timescale, changes in topography can also affect the water table, partly through the effect of relief on horizontal water transport, a relationship which may be poorly modeled in the CM2.1.

A potential way to combine the strengths of these two models is to couple the water table model, or one like it, directly to a climate model, which is something that may be done in the future (Fan and Miguez-Macho 2010). The ECMWF model, for example, has been run with more advanced land hydrology. While horizontal transport of groundwater is still not included in those simulations, the more complex hydrology improves some aspects of the climate response (Balsamo et al. 2008).

On the subject of methane, the analysis presented in this dissertation does not try to quantify orbitally-forced changes in methane emission directly, but examines changes in water table depth, which should be related to wetland extent. Future research may attempt to approximate methane emissions by applying a relationship between water table depth, temperature, and methane emission to these results. While such an approximation would only be a first order estimate, it may be sufficient to serve as the basis for further discussion on the topic of orbitally-forced methane emissions.

5. CONCLUSIONS

The role of orbital cycles in influencing past climate variations has been the subject of much discussion over the past decades, and better understanding the response of the climate system to this forcing remains an intriguing question. This dissertation research has focused on the response of three aspects of the climate system to orbital forcing: radiative feedbacks, equatorial Pacific seasonality, and groundwater.

To isolate and explore the response of the climate system to orbital forcing, this research forced an AOGCM with idealized orbital forcings, where obliquity and longitude of the perihelion are varied without the competing effects of changes in ice sheets and atmospheric composition. The effects of feedbacks in these simulations were analyzed and compared with those estimated from a doubled CO_2 experiment to determine whether feedbacks behave consistently under orbital and anthropogenic forcing. Changes in the seasonal cycle of the Pacific Ocean were quantified and compared with results from a slab ocean model, and the response at the mid-Holocene was compared to ten CMIP5 simulations. Finally, the AOGCM simulations were used to drive a water table model, and changes in soil moisture and shallow water table coverage under various orbital forcing was explored.

From the results, the following statements may be made regarding radiative feedbacks:

- Global-mean climate change can result from a simple redistribution of insolation, even when global-mean insolation change is zero and radiative forcing is small, because of the influence of radiative feedbacks. Furthermore, ΔT does not have to be the same sign as the radiative forcing, either locally or globally, if the effects of feedbacks are sufficient to overwhelm the direct radiative forcing.
- The relative importance of each feedback to the global-mean climate response is contingent on the temporal and spatial distribution of the forcing. While the water vapor feedback results in the largest global-mean ΔR_{net} in the doubled CO_2 experiment (Table 2), it provides the smallest global-mean ΔR_{net} in both orbital experiments. The lapse rate and cloud feedbacks prove most important in both orbital experiments, together accounting for over 70% of the global-mean ΔR_{net} from feedbacks.
- While many aspects of the feedbacks may be considered a simple response to local ΔT, some are not, especially in the water vapor, lapse rate, and cloud feedbacks. Circulation changes, which are largely dependent on the seasonal and spatial patterns of forcing, affect regional feedbacks in important ways. Monsoon circulations are especially important, playing a large role in influencing WS-SS feedbacks and a smaller role in influencing Lo-Hi feedbacks.
- Vertical variations in the meridional transport of MSE anomalies may play a role in extending the reach of local climate anomalies to more distant areas. In the Lo-Hi experiment, increases in MSE in the tropics may be

transported poleward at altitude while negative MSE anomalies from the high latitudes are transported equatorward near the surface, increasing the large-scale stability of the atmosphere and encouraging global-mean cooling through impacts on the lapse rate and cloud feedbacks.

- Cloud feedbacks partially counteract changes in summer insolation over some NH high-latitude ocean and continental regions during times most favorable for ice sheet expansion. However, it is unclear how clouds would react to ice sheet expansion or reduction as the CM2.1 lacks dynamic ice sheets.

Regarding the equatorial Pacific seasonal cycle, the following results were found:

- Variations in longitude of the perihelion can result in large changes to the timing and magnitude of the equatorial Pacific seasonal temperature cycle in the CM2.1. The eastern cold tongue region is most sensitive to this precession forcing and, according to a first harmonic fit, the Niño 3 region should have maximum seasonal amplitude of SSTs when longitude of the perihelion is around 155° (i.e., perihelion is in late February). SST changes in the western Pacific warm pool are comparatively smaller. The SM2.1, a slab ocean model, exhibits smaller changes in eastern equatorial Pacific SSTs, suggesting that the CM2.1 response is heavily influenced by ocean dynamics.
- While precession-driven SST changes in the western Pacific warm pool are primarily a direct thermodynamic response to changes in insolation,

changes in the east Pacific in the CM2.1 initially result from thermocline signal propagation from the west. In boreal spring, a weakening of the Pacific subtropical anticyclones, together with an eastward shift in convection in the western equatorial Pacific, appears to cause anomalous westerly winds which promote convergence of surface water and downwelling. This results in a warm temperature anomaly which travels along the thermocline to the east. A complementary cold thermocline response occurs during the other half of the year. These temperature fluxes surface in the east later in the year and, reinforced by local insolation change, affect eastern equatorial Pacific seasonality.

- Obliquity variations result in little change to equatorial Pacific seasonality in either the CM2.1 or SM2.1 results, suggesting that the seasonal cycle has not been very sensitive to changes in obliquity during at least the past 600 kyr.
- Mid-Holocene experiments using the GFDL CM2.1 and 10 CMIP5 models show reductions in the eastern equatorial Pacific seasonal cycle, similar to the AE-preind experiment. Furthermore, nine of the ten CMIP5 models replicate the changes in the western equatorial Pacific zonal winds and the thermocline signal mechanism that produces the temperature anomaly in the GFDL CM2.1, indicating that this response is robust across the models considered.
- Because precession can result in significant changes to equatorial Pacific seasonality, it may be difficult to discern past ENSO variations from proxy

records which reveal changes in extreme temperature events but lack the time-resolution necessary to show year to year variations.

Concerning the water table and soil moisture:

- Changes in water flux to the land surface generally produce root zone water and shallow water table coverage anomalies of the same sign, but differences do occur. For root zone water, this may be caused by the bucket nature of the land model, in which water anomalies are transferred to the deeper groundwater when the root zone region is overfilled. For the water table, regions with differences in sign have a higher mean relief, perhaps due to higher rates of horizontal water transport on steeper slopes.
- Correlations between changes in water flux, root zone water, and shallow water table coverage are all positive, with correlation (r) values between 0.31 and 0.57. The comparisons between root zone water and shallow water table coverage appear to show a duel response, with higher root zone anomalies often corresponding to lower shallow water table coverage anomalies and vice versa, perhaps depending on the mean depth of the water table.
- Changes in relative lake levels between 6ka and 0ka, reconstructed from proxy records (Vaiu and Gajewski 2001), agree reasonably well with changes in shallow water table coverage in a 6ka-modern water table model experiment. The AE and SS simulations produce similar results to

the 6ka simulation, suggesting that much of the mid-Holocene response may be driven by changes in precession.

- Shallow water table coverage in the tropics can be significantly affected by changes in obliquity and precession. Because tropical wetlands are a large natural source of methane, this may support the hypothesis that changes in wetland extent, driven by orbitally-forced P-E anomalies, drive (or at least contribute to) the methane variations with obliquity and precession periodicities observed in ice cores.

These results explore the response of three aspects of the climate system to orbital forcing. They emphasize the significant role of radiative feedbacks in shaping orbitally forced climate change, the ability of precession to affect the strength and timing of equatorial Pacific SSTs, and the response of the water table and soil moisture to orbital forcing.

By no means do these findings present a complete picture of the climate system response to orbital forcing, but represent three interesting aspects which may have played important roles in influencing climate in the past. Many other parts of the climate response have not yet been thoroughly explored in these simulations, and undoubtedly there are interesting features yet to be studied. Orbitally forced changes in energy transport of the oceans, for instance, which are responsible for a considerable portion of the Earth's meridional heat transport (e.g., Johns et al. 2011), might be an interesting course of study. Ocean transport of energy has been studied somewhat in the obliquity simulations (Mantsis et al.

2011), but not in the precession simulations. In particular, the meridional overturning circulation in the Atlantic has been the subject of significant research in other studies, but its response to past climate changes are still not completely clear. Model simulations from phase 2 of the Paleoclimate Modeling Comparison Project (PMIP2) disagree on even the sign of the change at the LGM (Weber et al. 2007). Understanding how this feature responds to orbital forcing may shed some light on the role of ocean heat transport throughout the Quaternary.

On a smaller scale, climate conditions which affect storminess in various regions of the world could be interesting. While the CM2.1 resolution is too course to resolve many features of storms themselves, analysis could focus on changes in the quantities that encourage storm development. Of relevance to the United States, changes in the factors influencing tornadoes in the midwest, or nor'easters along the East Coast, or tropical storm development and strengthening in the low latitude oceans could make for interesting research. Research on climate induced changes in storm surge in the New York area from tropical and extratropical storms is currently getting underway at Rutgers University using other models, and the influence of orbital forcing on such factors could accompany such work nicely.

Over approximately the next two years, these idealized orbital simulations, and others which help isolate the climate response to ice sheets and CO_2, will also be used to help identify the orbital, ice sheet, and greenhouse gas signals in proxy records. This comparison between model results and proxy records should help explain some of the observed variations in the proxy record, as well as

comment on the linear and nonlinear aspects of the climate response. Before that research gets underway, some additional research will be conducted on the topics discussed in this dissertation.

In addition to the ideas mentioned here, it is hoped that these idealized orbital simulations, or ones like them, will be useful in understanding many aspects of the climate system. Future modeling studies may also help resolve some of the limitations of these simulations, such as the lack of two slower feedback mechanisms which affect glacial/interglacial cycles: the growth and decay of ice sheets and the response of the carbon cycle. In many paleoclimate simulations, ice sheets and greenhouse gases are prescribed as forcings and not allowed to change. However, orbital theory suggests that these two mechanisms are actually slow feedbacks, which respond in complex ways to orbital forcings and other features of the climate system (Abe-Ouchi et al. 2013). Idealized orbital simulations performed on a model with interactive ice sheet and carbon cycle components would likely produce much larger climate variations than those presented here, and would help in understanding the climate system's large responses to orbital forcing during the Quaternary. Progress is being made in modeling ice sheets (e.g., Ganopolski et al. 2010), so simulations of this sort should be possible in the future. Such simulations may also help in research of the changing role of orbital cycles at around 800 kya, when glacial cycles transitioned between periods of roughly 40 kyr and 100 kyr, a shift which likely depended on complex Earth system interactions.

While the scope of such questions can be daunting, the prospect of

learning more about such vast climate system responses, and many other features of the climate system, is compelling. It is hoped that this research of radiative feedbacks, equatorial Pacific seasonality, and wetland extent will lead to further research into relationships in the climate system, both in past climate and the potential responses of the climate system in the future.

REFERENCES

Abe-Ouchi, A., F. Saito, K. Kawamura, M. E. Raymo, J. Okuno, K. Takahashi, and H. Blatter, 2013: Insolation-driven 100,000-year glacial cycles and hysteresis of ice-sheet volume. *Nature*, **500**, 190-193, doi:10.1038/nature12374.

Anderson, J. L., and Coauthors, 2004: The new GFDL global atmosphere and land model AM2-LM2: Evaluation with prescribed SST simulations. *J. Climate*, **17**, 4641-4673.

Ashkenazy, Y., I. Eisenman, H. Gildor, and E. Tziperman, 2010: The effect of Milankovitch variations in insolation on equatorial seasonality. *J. Climate*, **23**, 6133-6142, doi:10.1175/2010JCLI3700.1.

Balsamo, G., P. Viterbo, A. Beljaars, B. van den Hurk, M. Hirschi, A. K. Betts, and K. Scipal, 2008: A revised hydrology for the ECMWF model: Verification from field site to terrestrial water storage and impact in the integrated forecast system. *J. Hydrometeor.*, **10**, 623-643, doi:10.1175/2008JHM1068.1.

Bartlett, K. B., and R. C. Harriss, 1993: Review and assessment of methane emissions from wetlands. *Chemosphere*, **26**, 261-320.

Berger, A., 1978: Long-term variations of daily insolation and quaternary climatic changes. *J. Atmos. Sci.*, **35**, 2362-2367.

Berger, A., and M. F. Loutre, 1991: Insolation values for the climate of the last 10 million years. *Quat. Sci. Rev.*, **10**, 297-317.

Blunier, T., J. Chappellaz, J. Schwander, B. Stauffer, and D. Raynaud, 1995: Variations in atmospheric methane concentration during the Holocene epoch. *Nature*, **374**, 46-49, doi:10.1038/374046a0.

Bony, S., R. Colman, V. M. Kattsov, R. P. Allan, C. S. Bretherton, J.-L. Dufresne, A. Hall, S. Hallegatte, M. M. Holland, W. Ingram, D. A. Randall, B. J. Soden, G. Tselioudis, and M. J. Webb, 2006: How well do we understand and evaluate climate change feedback processes? *J. Climate*, **19**, 3445-3482.

Braconnot, P., Y. Luan, S. Brewer, and W. Zheng, 2012: Impact of Earth's orbit and freshwater fluxes on Holocene climate mean seasonal cycle and ENSO characteristics. *Clim. Dyn.*, **38**, 1081-1092, doi:10.1007/s00382-011-1029-x.

Capotondi, A., A. Wittenberg, and S. Masina, 2006: Spatial and temporal structure of tropical Pacific interannual variability in 20th century coupled simulations. *Ocean Modelling*, **15**, 274-298. doi:10.1016/j.ocemod.2006.02.004.

Chang, C.-P., Z. Wang, J. McBride, and C.-H. Liu, 2005: Annual cycle of southeast Asia-Maritime Continent rainfall and the asymmetric monsoon transition. *J. Climate*, **18**, 287-301.

Chappellaz, J. A., and I. Y. Fung, 1993a: The atmospheric CH4 increase since the Last Glacial Maximum. *Tellus*, **45B**, 228-241.

Chappellaz, J., T. Blunier, D. Raynaud, J. M. Barnola, J. Schwander, and B. Stauffer, 1993b: Synchronous changes in atmospheric CH4 and Greenland climate between 40 and 8 kyr BP. *Nature*, **366**, 443-445.

Chen, G.-S., J. E. Kutzbach, R. Gallimore, and Z. Liu, 2010: Calendar effect on phase study in paleoclimate transient simulation with orbital forcing. *Clim. Dyn.*,

doi:10.1007/s00382-010-0944-6.
Clark, P. U., J. J. Clague, B. B. Curry, A. Dreimanis, S. R. Hicock, G. H. Miller, G. W. Berger, N. Eyles, M. Lamothe, B. B. Miller, R. J. Mott, R. N. Oldale, R. R. Stea, J. P. Szabo, L. H. Thorleifson, and J. S. Vincent, 1993: Initiation and development of the Laurentide and Cordilleran ice sheets following the last interglaciation. *Qua. Sci. Rev.*, **12**, 79-114, doi:10.1016/0277-3791(93)90011-A.
Clark, P. U., R. B. Alley, and D. Pollard, 1999: Northern Hemisphere ice-sheet influences on global climate change. *Science*, **286**, 1104-1111, doi:10.1126/science.286.5442.1104.
Clement, A. C., R. Seager, and M. A. Cane, 1999: Orbital controls on the El Niño/Southern Oscillation and the tropical climate. *Paleoceanography*, **14**, 441-456.
Clement, A. C., A. Hall, and A. J. Broccoli, 2004: The importance of precessional signals in the tropical climate. *Clim. Dyn.*, **22**, 327-341, doi:10.1007/s00382-003-0375-8.
Clement, A. C., R. Burgman, and J. R. Norris, 2010: Response to comment on "Observational and model evidence for positive low-level cloud feedback". *Science*, **329**, 277-b, doi:10.1126/science.1187667.
Collins, M., S.-I. An, W. Cai, A. Ganachaud, E. Guilyardi, F.-F. Jin, M. Jochum, M. Lengaigne, S. Power, A. Timmermann, G. Vecchi, and A. Wittenberg, 2010: The impact of global warming on the tropical Pacific and El Niño. *Nature Geoscience*, **3**, 391-397. doi:10.1038/ngeo868.
Colman, R., 2003: A comparison of climate feedbacks in general circulation models. *Clim. Dyn.*, **20**, 865-873, doi:10.1007/s00382-003-0310-z.
Delworth, T. L., et al., 2006: GFDL's CM2 global coupled climate models. Part I: Formulation and simulation characteristics. *J. Climate*, **19**, 643-674.
Diaz, H. F., M. P. Hoerling, and J. K. Eischeid, 2001: ENSO variability, teleconnections and climate change. *Int. J. Climatol.*, **21**, 1845-1862, doi:10.1002/joc.631.
Downing, J. A., Y. T. Prairie, J. J. Cole, C. M. Duarte, L. J. Tranvik, R. G. Striegl, W. H. McDowell, P. Kortelainen, N. F. Caraco, J. M. Melack, and J. J. Middelburg, 2006: The global abundance and size distribution of lakes, ponds, and impoundments. *Limnol. Oceanogr.*, **51**, 2388-2397.
Döll, P., and K. Fiedler, 2007: Global-scale modeling of groundwater recharge. *Hydrol. Earth Syst. Sci. Discuss.*, **4**, 4069-4124.
Emile-Geay, J., K. Cobb, M. Mann, and A. T. Wittenberg, 2013a: Estimating central equatorial Pacific SST variability over the past millennium. Part 1: Methodology and validation. *J. Climate*, 26, 2302-2328. doi:10.1175/JCLI-D-11-00510.1.
Emile-Geay, J., K. Cobb, M. Mann, and A. T. Wittenberg, 2013b: Estimating central equatorial Pacific SST variability over the past millennium. Part 2: Reconstructions and implications. J. Climate, 26, 2329-2352. doi:10.1175/JCLI-D-11-00511.1.
Erb, M. P., A. J. Broccoli, and A. C. Clement, 2013: The contribution of radiative feedbacks to orbitally-driven climate change. *J. Clim.*, **26**, 5897-5914, doi:10.1175/JCLI-D-12-00419.1.
Erb, M. P., A. J. Broccoli, N. T. Graham, A. C. Clement, A. T. Wittenberg, and G. A.

Vecchi, 2013: Response of the equatorial Pacific seasonal cycle to orbital forcing. *In preparation.*

Ganopolski, A., R. Calov, and M. Claussen, 2010: Simulation of the last glacial cycle with a coupled climate ice-sheet model of intermediate complexity. *Clim. Past*, **6**, 229-244, doi:10.5194/cp-6-229-2010.

Guilyardi, E., A. Wittenberg, A. Fedorov, M. Collins, C. Wang, A. Capotondi, G. J. van Oldenborgh, and T. Stockdale, 2009: Understanding El Nino in ocean-atmosphere general circulation models. *Bull. Amer. Meteor. Soc.*, 325-340.

Fan, Y., and G. Miguez-Macho, 2010: A simple hydrologic framework for simulating wetlands in climate and earth system models. *Clim. Dyn.*, 26pp., doi:10.1007/s00382-010-0829-8.

Fan, Y., G. Miguez-Macho, C. P. Weaver, R. Walko, and A. Robock, 2007: Incorporating water table dynamics in climate modeling: 1. Water table observations and equilibrium water table simulations. *J. Geophys. Res.*, **112**, 17pp., doi:10.1029/2006JD008111.

Fan, Y., H. Li, and G. Miguez-Macho, 2013: Global patterns of groundwater table depth. *Science*, **339**, 940-943, doi:10.1126/science.1229881.

Fleitmann, D., S. J. Burns, A. Mangini, M. Mudelsee, J. Kramers, I. Villa, U. Neff, A. A. Al-Subbary, A. Buettner, D. Hippler, A. Matter, 2007: Holocene ITCZ and Indian monsoon dynamics recorded in stalagmites from Oman and Yemen (Socotra). *Qua. Sci. Rev.*, **26**, 170-188, doi:10.1016/j.quascirev.2006.04.012.

Friborg, T., H. Soegaard, T. R. Christensen, C. R. Lloyd, and N. S. Panikov, 2003: Siberian wetlands: Where a sink is a source. *Geophys. Res. Lett.*, **30**, 4pp., doi:10.1029/2003GL017797.

Hall, A., 2004: The role of surface albedo feedback in climate. *J. Climate*, **17**, 1550-1568.

Hall, A., A. C. Clement, D. W. J. Thompson, A. J. Broccoli, and C. S. Jackson, 2005: The importance of atmospheric dynamics in the northern hemisphere wintertime climate response to changes in the earth's orbit. *J. Climate*, **18**, 1315-1325, doi:10.1175/JCLI3327.1.

Harrison, D. E., A. M. Chiodi, and G. A. Vecchi, 2009: Effects of surface forcing on the seasonal cycle of the eastern equatorial Pacific. *J. Mar. Res.*, **67**, 701-729.

Hays, J. D., J. Imbrie, and N. J. Shackleton, 1976: Variations in the Earth's orbit: Pacemaker of the ice ages. *Science*, **194**, 1121-1132.

Herweijer, C., R. Seager, M. Winton, and A. Clement, 2005: Why ocean heat transport warms the global mean climate. *Tellus*, **57A**, 662-675.

Huybers, P., 2006: Early pleistocene glacial cycles and the integrated summer insolation forcing. *Science*, **313**, 508-511, doi:10.1126/science.1125249.

Huybers, P. and E. Tziperman, 2008: Integrated summer insolation forcing and 40,000-year glacial cycles: The perspective from an ice-sheet/energy-balance model. *Paleoceanography*, **23**, 18pp., doi:10.1029/2007PA001463.

Imbrie, J., et al., 1993: On the structure and origin of major glaciations cycles 2. The 100,000-year cycle. *Paleoceanography*, **8**, 699-735.

Jackson, C. S., and A. J. Broccoli, 2003: Orbital forcing of Arctic climate: Mechanisms of climate response and implications for continental glaciations. *Clim. Dyn.*, **21**, 539-557, doi:10.1007/s00382-003-0351-3.

Johns, W. E., M. O. Baringer, L. M. Beal, S. A. Cunningham, T. Kanzow, H. L. Bryden, J. J. M. Hirschi, J. Marotzke, C. S. Meinen, B. Shaw, and R. Curry, 2011: Continuous, array-based estimates of Atlantic Ocean heat transport at 26.5°N. *J. Climate*, **24**, 2429-2449, doi:10.1175/2010JCLI3997.1.

Joseph, R., and S. Nigam, 2006: ENSO evolution and teleconnections in IPCC's twentieth-century climate simulations: Realistic representation? *J. Climate*, **19**, 4360-4377.

Joussaume, S., and P. Braconnot, 1997: Sensitivity of paleoclimate simulation results to season definitions. *J. Geophys. Res.*, **102**, 1943-1956, doi:10.1029/96JD01989.

Jouzel, J., et al., 2007: Orbital and millennial Antarctic climate variability over the past 800,000 years. *Science*, **317**, 793-796, doi:10.1126/science.1141038.

Kayranli, B., M. Scholz, A. Mustafa, Å. Hedmark, 2010: Carbon storage and fluxes within freshwater wetlands: A critical review. *Wetlands*, **30**, 111-124, doi:10.1007/s13157-009-0003-4.

Khodri, M., M. A. Cane, G. Kukla, J. Gavin, and P. Braconnot, 2005: The impact of precession changes on the Arctic climate during the last interglacial-glacial transition. *Earth Planet. Sci. Lett.*, **236**, 285-304, doi:10.1016/j.epsl.2005.05.011.

Kug, J.-S., J. Choi, S.-I. An, F.-F. Jin, and A. T. Wittenberg, 2010: Warm pool and cold tongue El Niño events as simulated by the GFDL CM2.1 coupled GCM. *J. Climate*, **23**, 1226-1239. doi:10.1175/2009JCLI3293.1.

Lambeck, K., and J. Chappell, 2001: Sea level change through the last glacial cycle. *Science*, **292**, 679-686, doi:10.1126/science.1059549.

Lee, S.-Y., and C. J. Poulsen, 2005: Tropical Pacific climate response to obliquity forcing in the Pleistocene. *Paleoceanography*, **20**, 10pp., doi:10.1029/2005PA001161.

Lee, S.-Y., and C. J. Poulsen, 2008: Amplification of obliquity forcing through mean annual and seasonal atmospheric feedbacks. *Clim. Past*, **4**, 515-534, doi:10.5194/cpd-4-515-2008.

Lehner, B., and P. Döll, 2004: Development and validation of a global database of lakes, reservoirs and wetlands. *J. Hydrology*, **296**, 22pp., doi:10.1016/j.jhydrol.2004.03.028.

Lengaigne, M. and G.A. Vecchi, 2009: Contrasting the termination of moderate and extreme El Niño events in Coupled General Circulation Models. *Clim. Dyn.*, **35**, 299-313, doi:10.1007/s00382-009-0562-3.

Lin, J.-L., 2007: The double-ITCZ problem in IPCC AR4 coupled GCMs: Ocean-atmosphere feedback analysis. *J. Climate*, **20**, 4497-4525, doi:10.1175/JCLI4272.1.

Loulergue, L., A. Schilt, R. Spahni, V. Masson-Delmotte, T. Blunier, B. Lemieux, J.-M. Barnola, D. Raynaud, T. F. Stocker, and J. Chappellaz, 2008: Orbital and millennial-scale features of atmospheric CH_4 over the past 800,000 years. *Nature*, **453**, 383-386, doi:10.1038/nature06950.

Luan, Y., P. Braconnot, Y. Yu, W. Zheng, and O. Marti, 2012: Early and mid-Holocene climate in the tropical Pacific: seasonal cycle and interannual variability induced by insolation changes. *Clim. Past*, **8**, 1093-1108, doi:10.5194/cp-8-1093-2012.

Manabe, S., and R. J. Stouffer, 1980: Sensitivity of a global climate model to an increase of CO_2 concentrations in the atmosphere. *J. Geophys. Res.*, **85**, 5529-5554.

Mantsis, D. F., A. C. Clement, A. J. Broccoli, and M. P. Erb, 2011: Climate feedbacks in response to changes in obliquity. *J. Climate*, **24**, 2830-2845, doi:10.1175/2010JCLI3986.1.

Mantsis, D. F., A. C. Clement, B. Kirtman, A. J. Broccoli, and M. P. Erb, 2013: Precessional cycles and their influence on the north Pacific and north Atlantic summer anticyclones. *J. Climate*, **26**, 4596-4611, doi:10.1175/JCLI-D-12-00343.1.

McGregor, S., A. Timmermann, M. H. England, O. Elison Timm, and A. T. Wittenberg, 2013: Inferred changes in El Niño-Southern Oscillation variance over the past six centuries. *Clim. Past,* **9**, 2269-2284. doi:10.5194/cp-9-2269-2013.

Meehl, G. A., C. Covey, T. Delworth, M. Latif, B. McAvaney, J. F. B. Mitchell, R. J. Stouffer, and K. E. Taylor, 2007: The WCRP CMIP3 multimodel dataset: A new era in climate change research. *Bull. Amer. Meteor. Soc.*, **88**, 1383-1394, doi:10.1175/BAMS-88-9-1383.

Merryfield, W J, 2006: Changes to ENSO under CO_2 doubling in a multimodel ensemble. *J. Climate*, **19**, 4009-4027.

Miguez-Macho, G., H. Li, and Y. Fan, 2008: Simulated water table and soil moisture climatology over North America. *Bull. Amer. Meteor. Soc.*, 663-672, doi:10.1175/BAMS-89-5-663.

Milankovitch, M., 1941: Kanon der erdbestrahlung und seine anwendung auf das eiszeitenproblem (Canon of insolation and the ice-age problem). *Royal Serbian Academy, Special Publication*, **133**, 1-633.

Milly, P. C. D., and A. B. Shmakin, 2002: Global modeling of land water and energy balances. Part I: The land dynamics (LaD) model. *J. Hydrometeor.*, **3**, 283-299.

Mitchell, T. D., and P. D. Jones, 2005: An improved method of constructing a database of monthly climate observations and associated high-resolution grids. *Int. J. Climatol.*, **25**, 693-712, doi:10.1002/joc.1181.

Oldenborgh, G. J. van, S. Y. Philip, and M. Collins, 2005: El Niño in a changing climate: A multi-model study. *Ocean Sci.*, **1**, 81-95.

Otto-Bliesner, B., and A. C. Clement, 2004: The sensitivity of the Hadley circulation to past and future forcings in two climate models. In *The Hadley Circulation: Past, Present and Future*. H.F. Diaz and R.S. Bradley, Eds., Advances in Global Change Research, vol. 21. Springer Verlag, 437-464.

Petit, J. R., et al., 1999: Climate and atmospheric history of the past 420,000 years from the Vostok ice core, Antarctica. *Nature*, **399**, 429-436.

Phillipps, P. J., and I. M. Held, 1994: The response to orbital perturbations in an atmospheric model coupled to a slab ocean. *J. Climate*, **7**, 767-782.

Pollard, D., and D. B. Reusch, 2002: A calendar conversion method for monthly mean paleoclimate model output with orbital forcing. *J. Geophys. Res.*, **107**, 7pp., doi:10.1029/2002JD002126.

Prell, W. L., and J. E. Kutzbach, 1987: Monsoon variability over the past 150,000 years. *J. Geophys. Res.*, **92**, 8411-8425.

Ramaswamy, V., et al., 2001: Radiative forcing of climate change. *Climate Change*

2001: The Scientific Basis. Intergovernmental Panel on Climate Change, Third Assessment Report. Cambridge University Press, Cambridge, United Kingdom and New York, NY, USA, 349-416.

Raymo, M. E., and K. Nisancioglu, 2003: The 41 kyr world: Milankovitch's other unsolved mystery. *Paleoceanography*, **18**, 6pp., doi:10.1029/2002PA000791.

Reichler, T., and J. Kim, 2008: How well do coupled models simulate today's climate? *Bull. Amer. Meteor. Soc.*, **89**, 303-311, doi:10.1175/BAMS-89-3-303.

Rind, D., and J. Perlwitz, 2004: The response of the Hadley circulation to climate changes, past and future. In *The Hadley Circulation: Past, Present and Future*. H.F. Diaz and R.S. Bradley, Eds., Advances in Global Change Research, vol. 21. Springer Verlag, 399-435.

Robock, A., 1983: Ice and snow feedbacks and the latitudinal and seasonal distribution of climate sensitivity. *J. Atmos. Sci.*, **40**, 986-997.

Rodwell, M. J., and B. J. Hoskins, 2001: Subtropical anticyclones and summer monsoons. *J. Climate*, **14**, 3192-3211.

Ruddiman, W. F., 2003: Orbital insolation, ice volume, and greenhouse gases. *Quat. Sci. Rev.*, **22**, 1597-1629, doi:10.1016/S0277-3791(03)00087-8.

Scholz, C. A., T. C. Johnson, A. S. Cohen, J. W. King, J. A. Peck, J. T. Overpeck, M. R. Talbot, E. T. Brown, L. Kalindekafe, P. Y. O. Amoako, R. P. Lyons, T. M. Shanahan, I. S. Casteñeda, C. W. Heil, S. L. Forman, L. R. McHargue, K. R. Beuning, J. Gomez, and J. Pierson, 2007: East African megadroughts between 135 and 75 thousand years ago and bearing on early-modern human origins. *PNAS*, **104**, 16416-16421, doi:10.1073/pnas.0703874104.

Smith, T. M., R. W. Reynolds, T. C. Peterson, and J. Lawrimore, 2008: Improvements to NOAA's historical merged land-ocean surface temperature analysis (1880-2006). *J. Climate*, **21**, 2283-2296, doi:10.1175/2007JCLI2100.1.

Soden, B. J., A. J. Broccoli, and R. S. Hemler, 2004: On the use of cloud forcing to estimate cloud feedback. *J. Climate*, **17**, 3661-3665.

Soden, B. J., and I. M. Held, 2006: An assessment of climate feedbacks in coupled ocean-atmosphere models. *J. Climate*, **19**, 3354-3360, doi:10.1175/JCLI3799.1.

Soden, B. J., I. Held, R. Colman, K. M. Shell, J. T. Kiehl, and C. A. Shields, 2008: Quantifying climate feedbacks using radiative kernels. *J. Climate*, **21**, 3504-3520, doi:10.1175/2007JCLI2110.1.

Soden, B. J., and G. A. Vecchi, 2011: The vertical distribution of cloud feedback in coupled ocean-atmosphere models. *Geophys. Res. Lett.*, **38**, 6pp., doi:10.1029/2011GL047632.

Spahni, R., J. Chappellaz, T. F. Stocker, L. Loulergue, G. Hausammann, K. Kawamura, J. Flügkiger, J. Schwander, D. Raynaud, V. Masson-Delmotte, and J. Jouzel, 2005: Atmospheric methane and nitrous oxide of the late Pleistocene from Antarctic ice cores. *Science*, **310**, 1317-1321, doi:10.1126/science.1120132.

Stouffer, R. J., A. J. Broccoli, T. L. Delworth, K. W. Dixon, R. Gudgel, I. Held, R. Hemler, T. Knutson, H.-C. Lee, M. D. Schwarzkopf, B. Soden, M. J. Spelman, M. Winton, and F. Zeng, 2006: GFDL's CM2 global coupled climate models. Part IV: Idealized climate response. *J. Climate*, **19**, 723-740.

Timm, O., A. Timmerman, A. Abe-Ouchi, F. Saito, and T. Segawa, 2008: On the

definition of seasons in paleoclimate simulations with orbital forcing. *Paleoceanography*, **23**, 12pp., doi:10.1029/2007PA001461.

Timmermann, A., S. J. Lorenz, S.-I. An, A. C. Clement, and S.-P. Xie, 2007: The effect of orbital forcing on the mean climate and variability of the tropical Pacific. *J. Climate*, **20**, 4147-4159, doi:10.1175/JCLI4240.1.

Tuenter, E., S. L. Weber, F. J. Hilgen, and L. J. Lourens, 2003: The response of the African summer monsoon to remote and local forcing due to precession and obliquity. *Global Planet. Change*, **36**, 219-235, doi:10.1016/S0921-8181(02)00196-0.

Tuenter, E., S. L. Weber, F. J. Hilgen, and L. J. Lourens, 2005a: Sea-ice feedbacks on the climatic response to precession and obliquity forcing. *Geophys. Res. Lett.*, **32**, 4pp., doi:10.1029/2005GL024122.

Tuenter, E., S. L. Weber, F. J. Hilgen, L. J. Lourens, and A. Ganopolski, 2005b: Simulation of climate phase lags in response to precession and obliquity forcing and the role of vegetation. *Clim. Dyn.*, **24**, 279-295, doi:10.1007/s00382-004-0490-1.

Tziperman, E., L. Stone, M. A. Cane, and H. Jarosh, 1994: El Niño chaos: Overlapping of resonances between the seasonal cycle and the Pacific Ocean-Atmosphere oscillator. *Science*, **264**, 72-74.

Tziperman, E., S. E. Zebiak, and M. A. Cane, 1997: Mechanisms of seasonal - ENSO interaction. *J. Atmos. Sci.*, **54**, 61-71.

Vecchi, G.A., 2006: The termination of the 1997-98 El Niño. Part II: Mechanisms of atmospheric change. *J. Climate*, **19**, 2647-2664.

Vecchi, G. A., and A. T. Wittenberg, 2010: El Niño and our future climate: Where do we stand? *Wiley Interdisciplinary Reviews: Climate Change*, **1**, 260-270. doi:10.1002/wcc.33.

Viau, A. E., and K. Gajewski, 2001: Holocene variations in the global hydrological cycle quantified by objective gridding of lake level databases. *J. Geophys. Res.*, **106**, 31703-31716, doi:10.1029/2000JD000237.

Wang, Y., H. Cheng, R. L. Edwards, X. Kong, X. Shao, S. Chen, J. Wu, X. Jiang, X. Wang, and Z. An, 2008: Millennial- and orbital-scale changes in the East Asian monsoon over the past 224,000 years. *Nature*, **451**, 1090-1093, doi:10.1038/nature06692.

Weber, S. L., S. S. Drijfhout, A. Abe-Ouchi, M. Crucifix, M. Eby, A. Ganopolski, S. Murakami, B. Otto-Bliesner, and W. R. Peltier, 2007: The modern and glacial overturning circulation in the Atlantic ocean in PMIP coupled model simulations. *Clim. Past*, **3**, 51-64.

Wetherald, R. T., 2010: Changes of time mean state and variability of hydrology in response to a doubling and quadrupling of CO_2. *Clim. Change*, **102**, 651-670, doi:10.1007/s10584-009-9701-4.

Wittenberg, A. T., 2009: Are historical records sufficient to constrain ENSO simulations? *Geophys. Res. Lett.*, **36**, L12702. doi:10.1029/2009GL038710.

Wittenberg, A. T., A. Rosati, N.-C. Lau, and J. J. Ploshay, 2006: GFDL's CM2 global coupled climate models. Part III: Tropical Pacific climate and ENSO. *J. Climate*, **19**, 698-722.

Wyrwoll, K.-H., Z. Liu, G. Chen, J. E. Kutzbach, and X. Liu, 2007: Sensitivity of the

Australian summer monsoon to tilt and precessional forcing. *Quat. Sci. Rev.*, **26**, 3043-3057, doi:10.1016/j.quascirev.2007.06.026.

Yoshimori, M, and A. J. Broccoli, 2008: Equilibrium response of an atmosphere-mixed layer ocean model to different radiative forcing agents: Global and zonal mean response. *J. Climate*, **21**, 4399-4423, doi:10.1175/2008JCLI2172.1.

Ziegler, M., E. Tuenter, and L. J. Lourens, 2010: The precession phase of the boreal summer monsoon as viewed from the eastern Mediterranean (ODP Site 968). *Quat. Sci. Rev.*, **29**, 1481-1490, doi:10.1016/j.quascirev.2010.03.011.

TABLES

	Eccentricity	Longitude of the Perihelion	Obliquity
AE	0.0493	0°	*23.439*°
WS	0.0493	90°	*23.439*°
VE	0.0493	180°	*23.439*°
SS	0.0493	270°	*23.439*°
0Ecc	0.0	---	*23.439*°
Lo	*0.01671*	*102.932*°	22.079°
Hi	*0.01671*	*102.932*°	24.480°
Preind	*0.01671*	*102.932*°	*23.439*°
6ka	0.0187	0.87°	22.949°

Table 1. Orbital values for the precession, obliquity, and time-slice simulations. The first four precession simulations represent times with perihelion at the NH autumnal equinox (AE), winter solstice (WS), vernal equinox (VE), and summer solstice (SS), with increased eccentricity to amplify the signal. The fifth simulation (0Ecc) has zero eccentricity and therefore no perihelion. Obliquity simulations represent low (Lo) and high (Hi) obliquity of the past 600 kyr (Berger and Loutre 1991), and values for the preindustrial (Preind) and mid-Holocene (6ka) simulations are also shown. Numbers in italics are preindustrial values. Note: There are two different sets of precession simulations and two different

preindustrial simulations, one run with the CM2.1 and one run with the slightly updated CM2.1R. Precession simulations in sections 2 and 3 use the CM2.1R, while precession simulations in section 4 use the CM2.1, to be consistent with other simulations in that section. Mid-Holocene and obliquity simulations only use the CM2.1. The CM2.1 preindustrial simulation is used when comparing it to the mid-Holocene. Differences between CM2.1 and CM2.1R simulations appear to be minor on the whole.

	Lo-Hi	WS-SS	Doubled CO_2
Surface Albedo	-0.27 (-0.28)	0.31 (0.18)	0.61
Water Vapor	-0.20 (-0.61)	0.19 (0.61)	4.02
Lapse Rate	-0.90 (-0.12)	0.47 (-0.24)	-0.70
Cloud	-0.67 (0.14)	0.74 (0.15)	1.06
Total	-2.03 (-0.87)	1.72 (0.69)	4.99

Table 2. Global annual-mean values for the effect of each feedback on ΔR_{net} (W m^{-2}). Estimated values, which are discussed in section 5, are given in parentheses for the sake of comparison. Note that different lengths of months between NH winter and NH summer solstice perihelion simulations may affect annual-mean differences.

Monsoon	Change in summer precipitation (mm day^{-1})	Region	
		Latitudes	Longitudes
North American	-0.28	0°-40°N	130°-60°W
South American	2.64	40°S-0°	90°-30°W
North African	-2.37	0°-40°N	20°W-45°E
South African	2.55	40°S-0°	0°-60°E
Asian	-1.65	0°-40°N	60°-150°E
Australian	3.00	40°S-0°	100°-160°E

Table 3. Changes in summer precipitation (mm day^{-1}) for six monsoon regions in the WS-SS experiment. Values are calculated for respective summers in each hemisphere (June-August in the NH and December-February in the SH). Monsoon regions are defined as the land areas between the given latitudes and longitudes. Results show a weakening of NH monsoons and a strengthening of SH monsoons in the WS-SS experiment.

	Lo-Hi	AE-VE	WS-SS	Mean
P → PP	35.9	40.1	39.5	38.5
P → PN	0.8	5.4	4.2	3.5
P → NP	6.9	12.2	6.0	8.4
P → NN	1.1	1.6	0.9	1.2
N → NN	32.0	25.6	35.3	31.0
N → NP	5.5	3.0	2.7	3.7
N → PN	12.2	10.1	9.5	10.6
N → PP	5.6	2.0	1.8	3.1

Table 4. Percentage of land grid cells (%) in the Lo-Hi, AE-VE, and WS-SS experiments which meet the given criteria. The three letters in the left column represent the sign of changes in precipitation-evapotranspiration, root zone water, and shallow water table coverage, respectively, with “P” meaning positive (or zero) and “N” meaning negative. For example, the second entry (P → PN), means that positive (or zero) change in precipitation-evapotranspiration leads to positive (or zero) change in root zone water but negative change in shallow water table coverage. The right column shows mean values of the three experiments. Columns may not add to exactly 100% due to rounding.

	Same sign	Different signs
Relief	0.0250	0.0301
Topographic elevation (m)	591	516
Saturation conductivity (m s^{-1})	9.20×10^{-5}	9.72×10^{-5}
Hydraulic conductivity e-folding depth (m)	39.1	28.2

Table 5. Mean values (averaged regionally and across all three simulations) of relief, topographic elevation (m), saturation conductivity (m s^{-1}), and hydraulic conductivity e-folding depth (m) (Fan et al. 2013, supplemental materials; H. Li, personal communication) for regions where P-E and shallow water table coverage are the same sign and where they are different signs.

Relief range	Percentage of grid cells with inconsistent signs (%)			
	Lo-Hi	AE-VE	WS-SS	Mean
<0.005	7.2	6.8	5.6	6.5
0.005-0.01	11.6	12.5	11.9	12.0
0.01-0.02	12.6	10.8	8.6	10.7
0.02-0.04	14.0	11.2	8.0	11.1
0.04-0.08	15.1	12.7	8.9	12.2
>0.08	12.7	15.5	12.1	13.4

Table 6. Percentage of grid cells in each range of relief values (averaged over 2° by 2.5° boxes) in which changes in P-E and shallow water table coverage have different signs for Lo-Hi, AE-VE, WS-SS, and the mean of all three experiments. For reference, the percentage of total boxes in the given relief ranges, from shallowest to steepest slope, are: 20.6%, 19.3%, 18.7%, 18.0%, 17.2%, and 6.3%.

	Root zone water vs. shallow water table coverage anomalies	P-E vs. root zone water anomalies	Recharge vs. shallow water table coverage anomalies
Lo-Hi	0.31	0.48	0.41
AE-VE	0.35	0.53	0.51
WS-SS	0.44	0.49	0.57

Table 7. Correlation (r) values for changes in the following quantities: root zone water vs. shallow water table coverage, P-E vs. root zone water, and recharge vs. shallow water table coverage. Change in recharge is used instead of change in P-E in the final column because of differences that arise when the water table model sets negative values of recharge to 0. All quantities are regridded to a 2° by 2.5° grid.

FIGURES

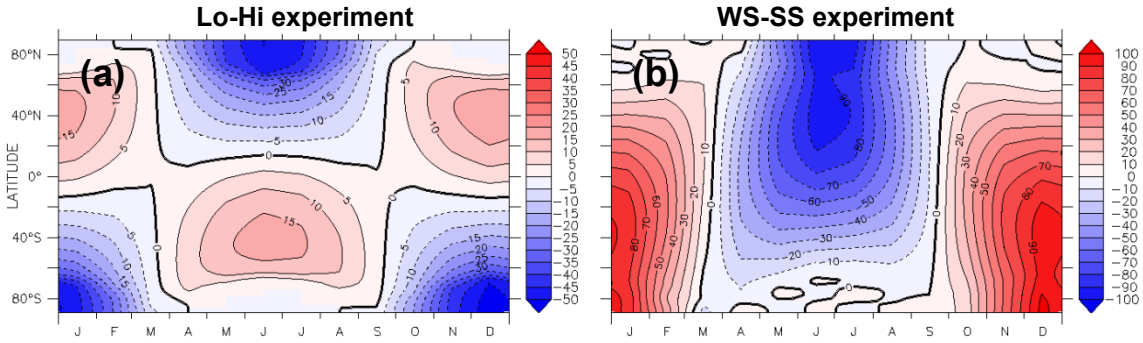

Figure 1. Seasonal changes in zonal-mean insolation (W m^{-2}) for the (a) Lo-Hi and (b) WS-SS experiments as a function of latitude.

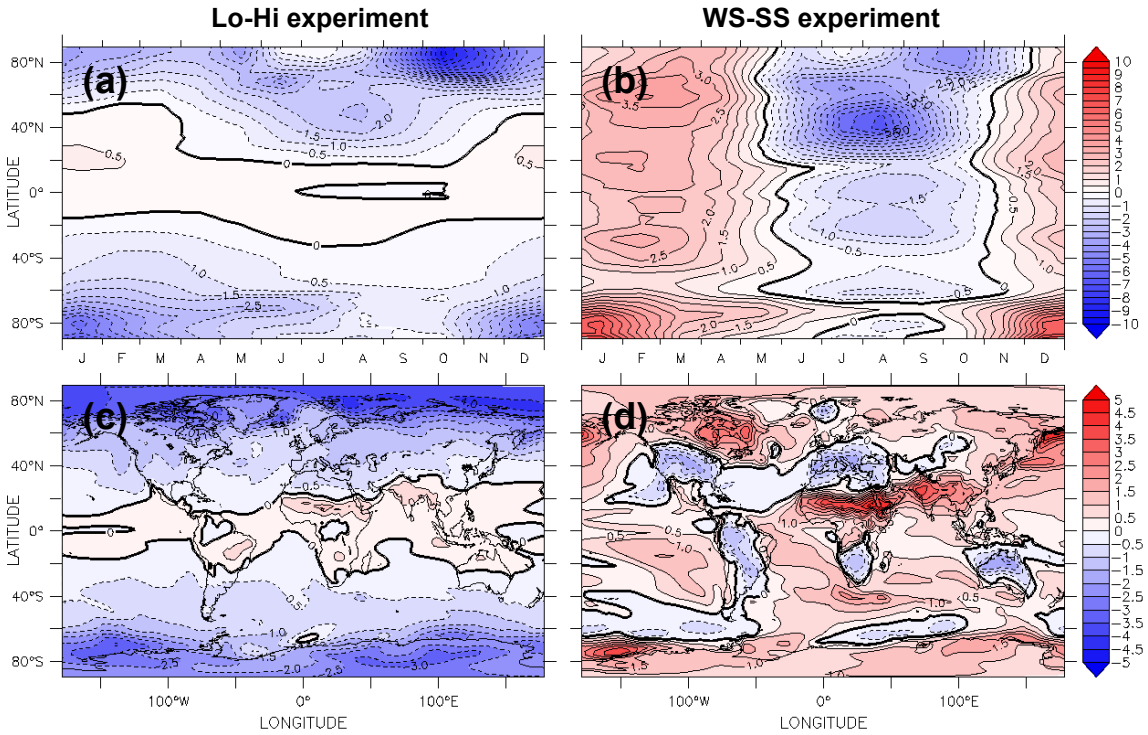

Figure 2. Change in (a),(b) zonal-mean surface air temperature (K) and (c),(d) annual-mean surface air temperature (K) for the (left) Lo-Hi and (right) WS-SS experiments.

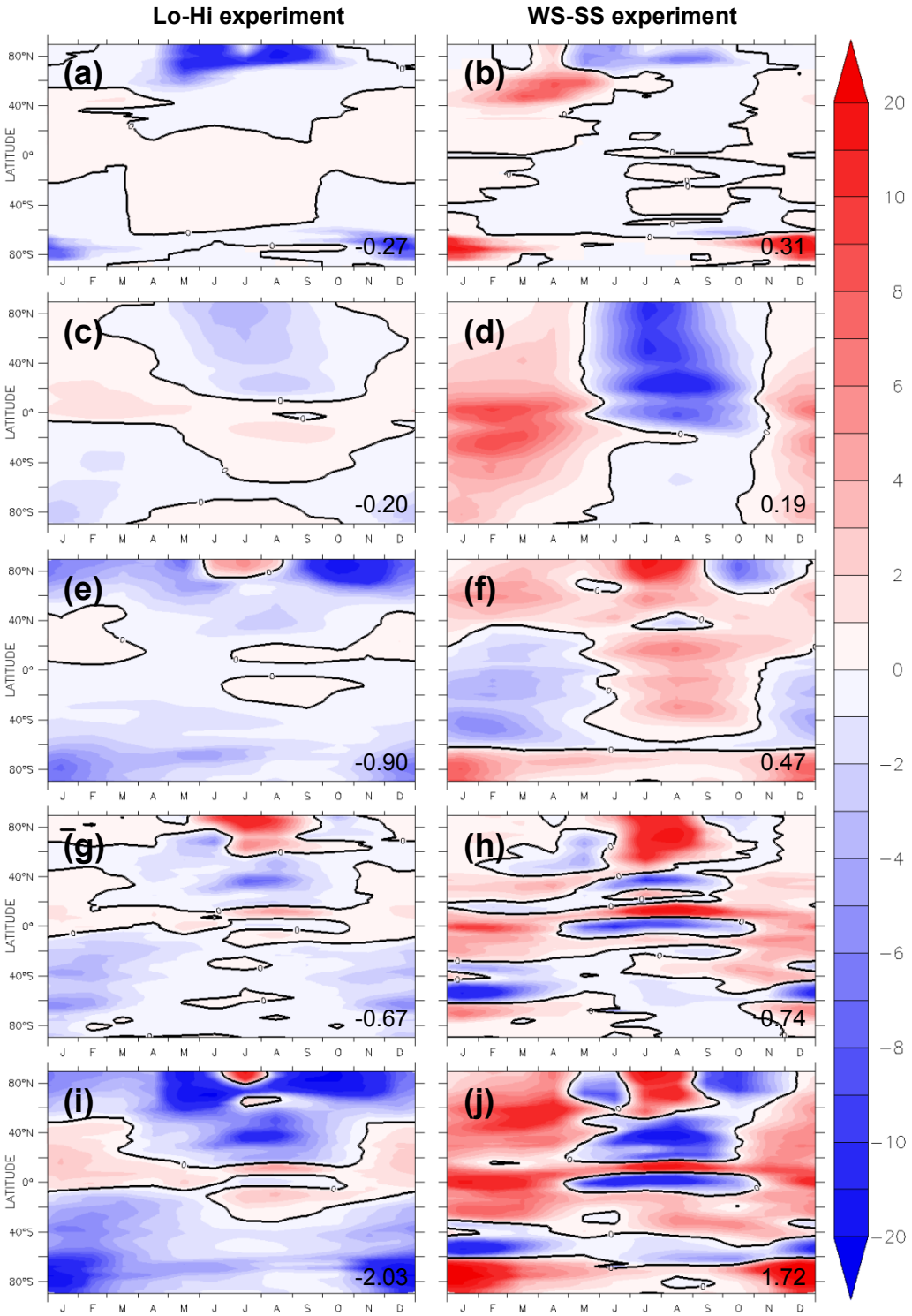

Figure 3. Effect of feedbacks on zonal-mean ΔR_{net} (W m^{-2}) caused by (a),(b) surface albedo, (c),(d) water vapor, (e),(f) lapse rate, (g),(h) clouds, and (i),(j) the sum of all four for the Lo-Hi and WS-SS experiments, respectively. Positive

values represent increased net downward radiation. Global-mean values (W m^{-2}) are given in the bottom right of each panel.

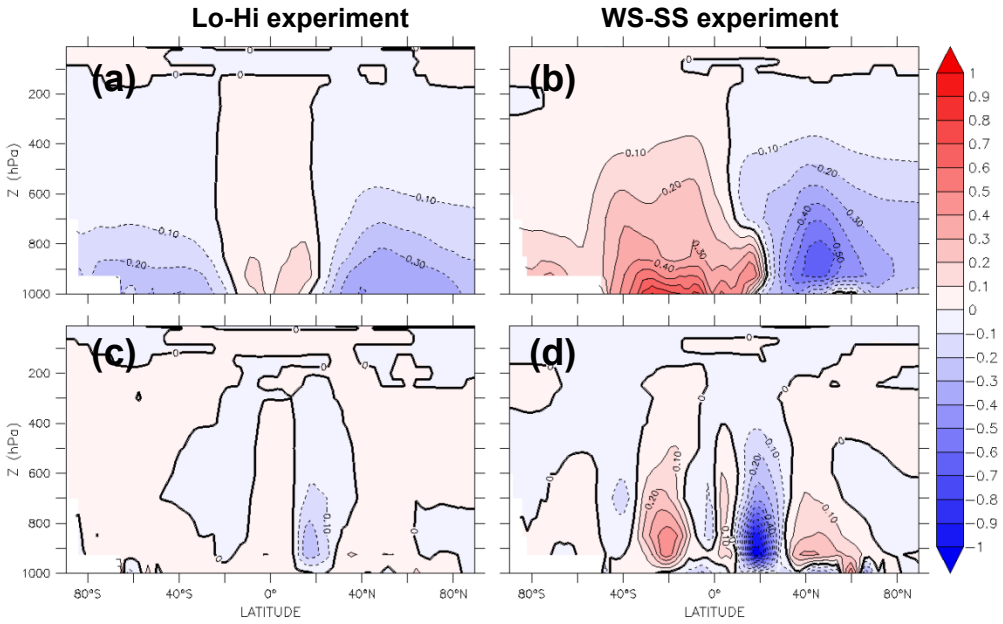

Figure 4. Change in (a),(b) thermodynamic and (c),(d) dynamic components of specific humidity (g kg^{-1}) for the Lo-Hi and WS-SS experiments. The thermodynamic component is calculated as the change in specific humidity that would result from ΔT at a fixed RH. The dynamic component is approximated as the difference between the thermodynamic component and the actual change in specific humidity (Herweijer et al. 2005).

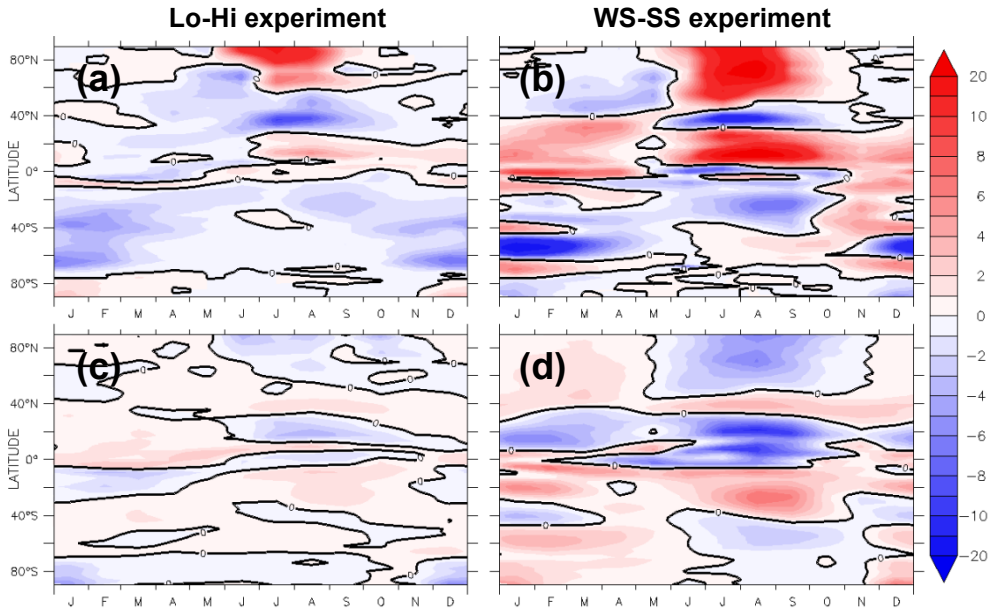

Figure 5. Effect of the cloud feedback on zonal-mean net TOA radiation (W m^{-2}) broken down into (a),(b) SW and (c),(d) LW effects in the Lo-Hi and WS-SS experiments.

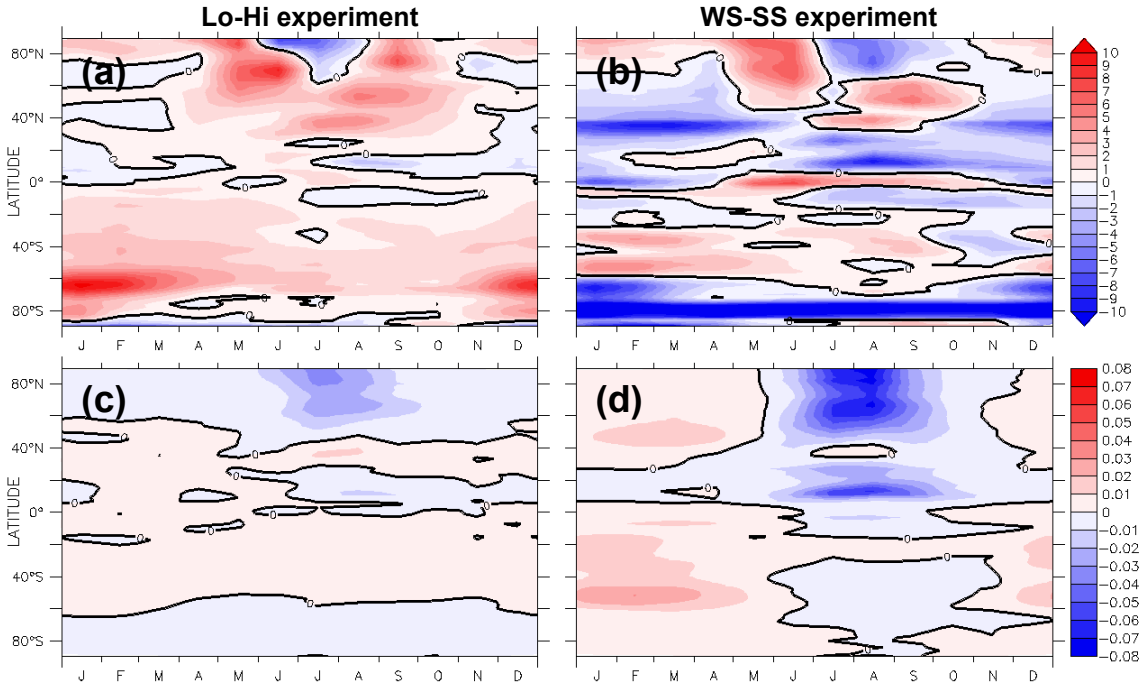

Figure 6. Change in (a),(b) zonal-mean low-cloud sky fraction (%) and (c),(d) vertically integrated cloud water (kg m^{-2}) for the Lo-Hi and WS-SS experiments.

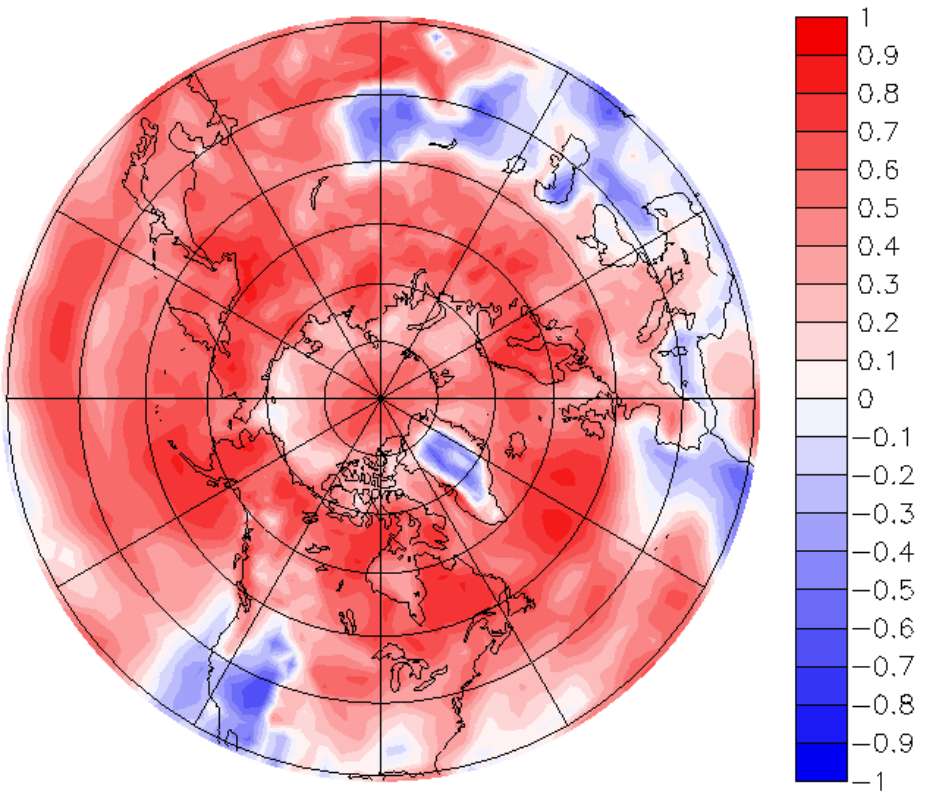

Figure 7. Temporal correlation between cloud water content and stability for July at 30°-90°N. The correlation is computed using 100 Julys of a preindustrial simulation and shows how water content varies with stability during Arctic Julys.

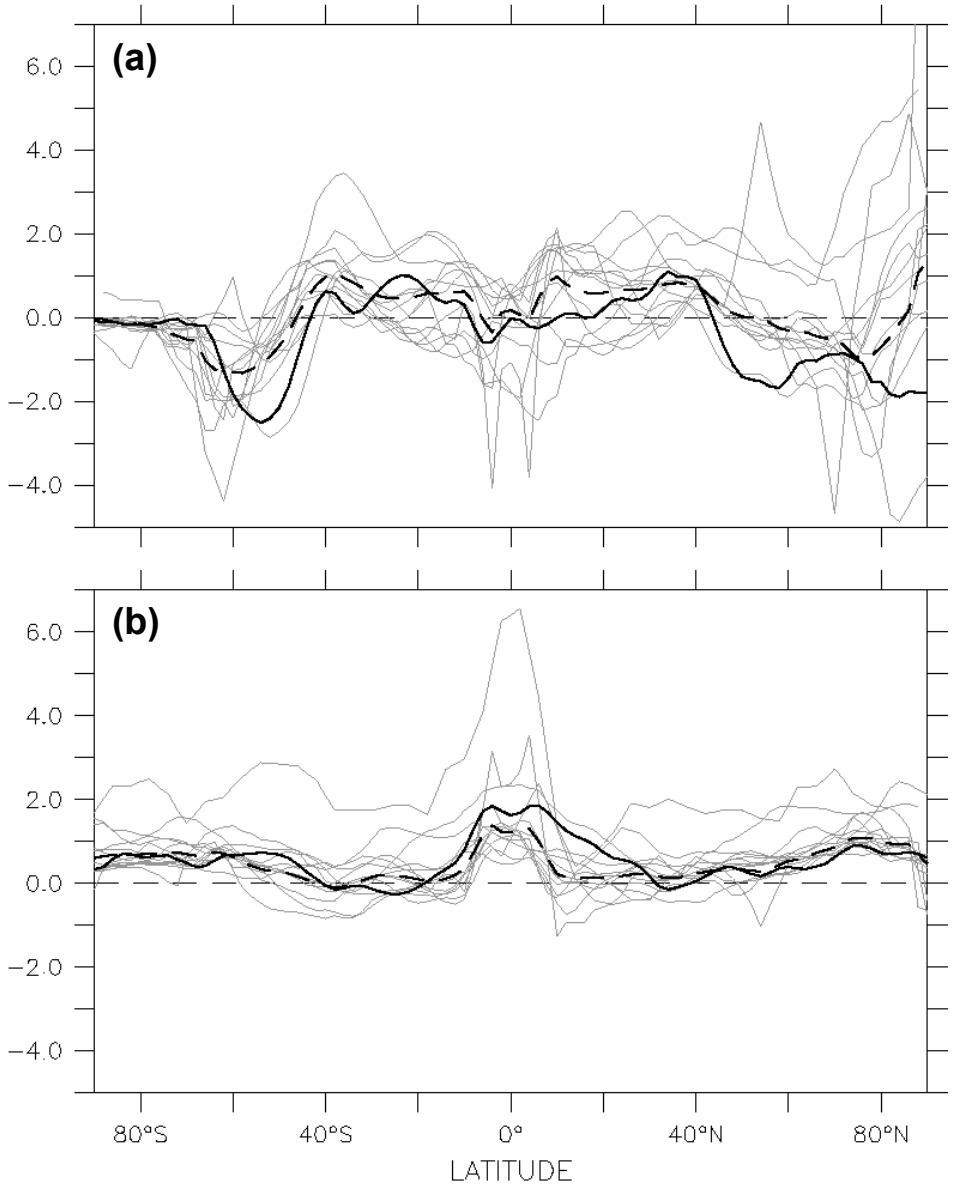

Figure 8. Annual zonal-mean (a) SW and (b) LW cloud feedbacks (W m^{-2} K^{-1}) from the CM2.1 (solid black) and 13 other CMIP3 models in a doubled CO_2 run (gray). Also shown is the ensemble of the models (dashed black).

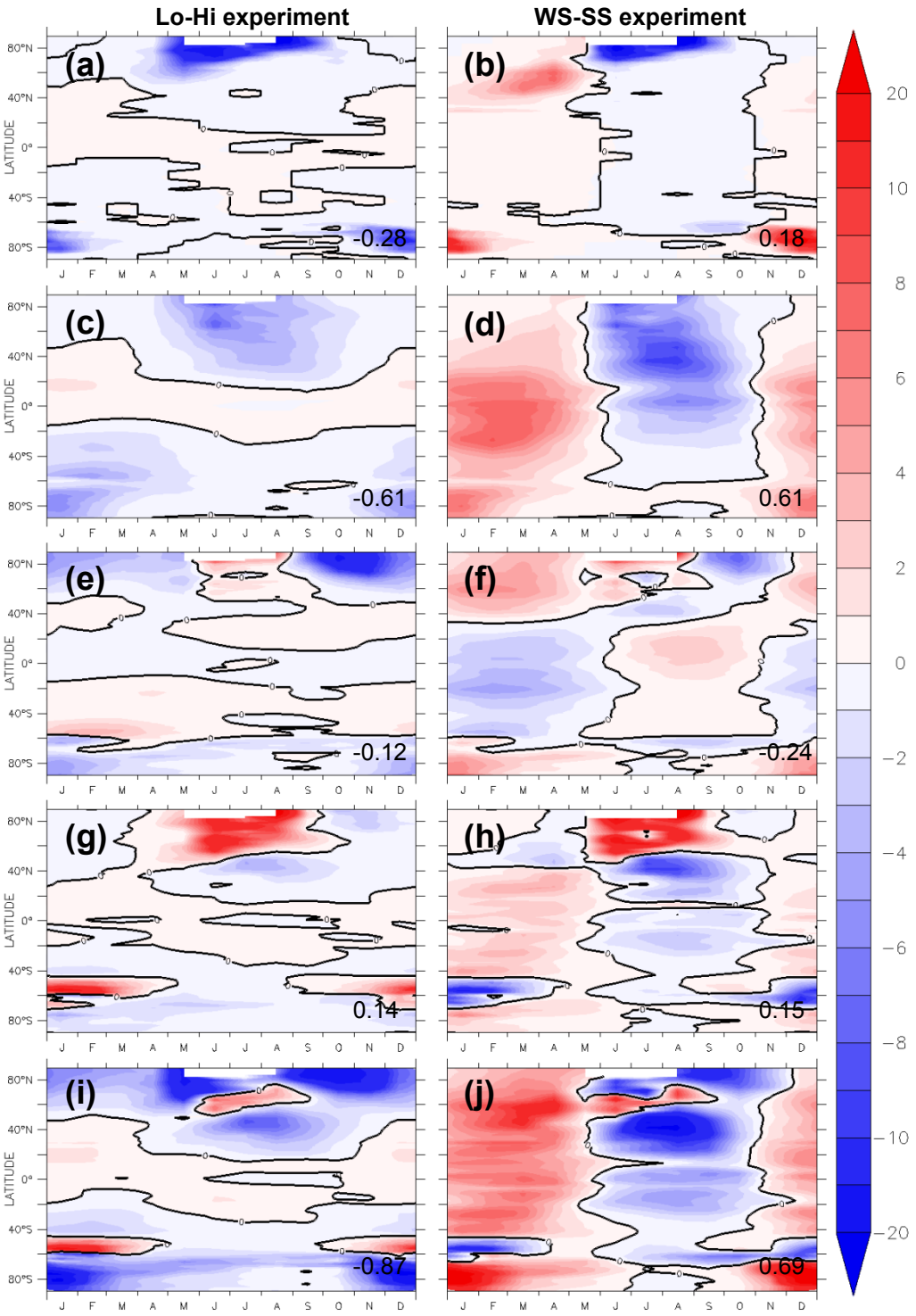

Figure 9. Effect of feedbacks on zonal-mean ΔR_{net} (W m^{-2}) estimated as the product of the doubled CO_2 feedback and the ΔT in each orbital experiment. As in Fig. 3, plots are shown for ΔR_{net} caused by (a),(b) surface albedo, (c),(d) water

vapor, (e),(f) lapse rate, (g),(h) clouds, and (i),(j) the sum of all four for the Lo-Hi and WS-SS experiments. Positive values represent increased net downward radiation. Global-mean values (W m^{-2}) are given in the bottom right of each panel.

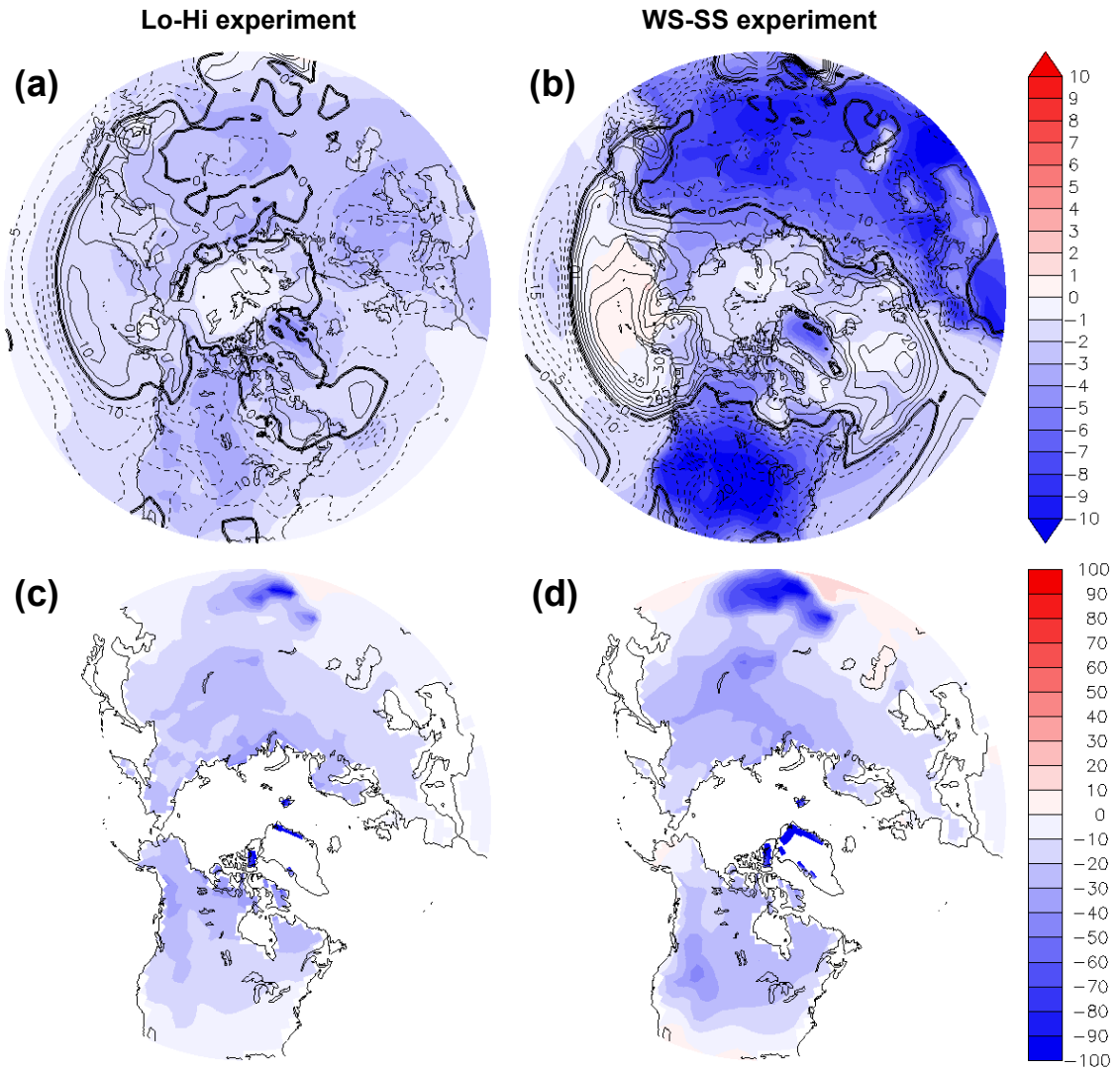

Figure 10. (top) Mean June-August ΔT poleward of 30°N in the (a) Lo-Hi and (b) WS-SS experiments (K; shaded). Contours are the ΔR_{net} from the mean June-August cloud radiative feedback (W m^{-2}). (bottom) Percent change in annual melting degree-days over land for (c) Lo-Hi and (d) WS-SS. Melting degree-days are calculated from climatological monthly values as the product of monthly temperature (for months that are above zero, in °C) and number of days per month. White areas over Greenland remain below freezing year round, so they have no melting degree-days in either simulation.

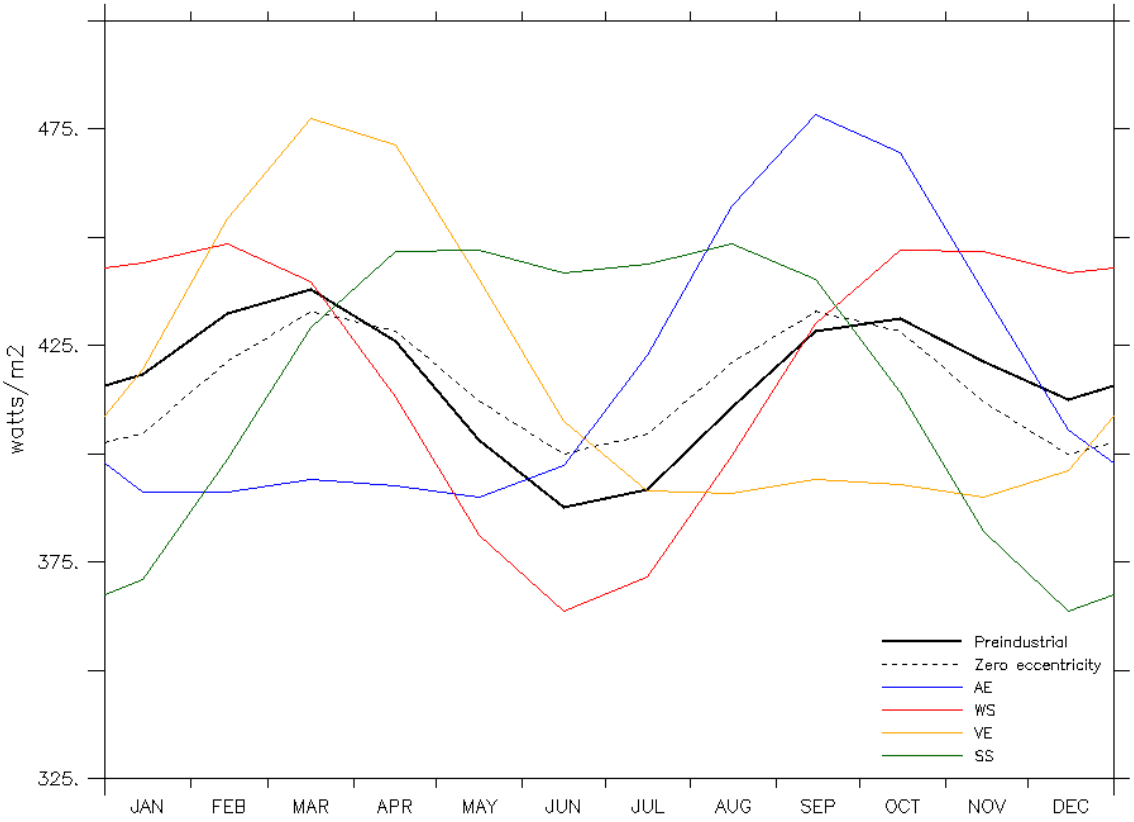

Figure 11. Mean 5°S-5°N incoming SW radiation at TOA (W m^{-2}) for preindustrial (black), zero eccentricity (dotted black), AE (blue), WS (red), VE (orange), and SS (green) simulations.

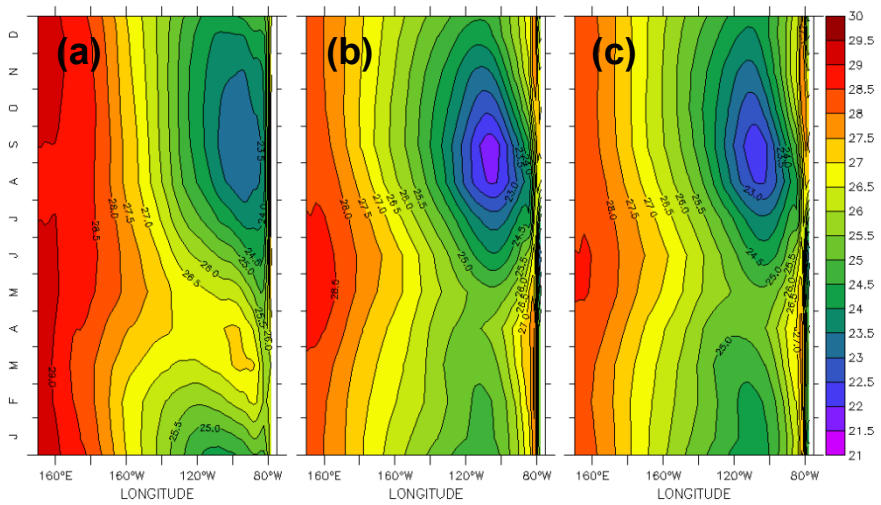

Figure 12. Mean 5°S-5°N Pacific SSTs (°C) for (a) ERSST.v3b observations as well as (b) preindustrial and (c) zero eccentricity CM2.1 simulations.

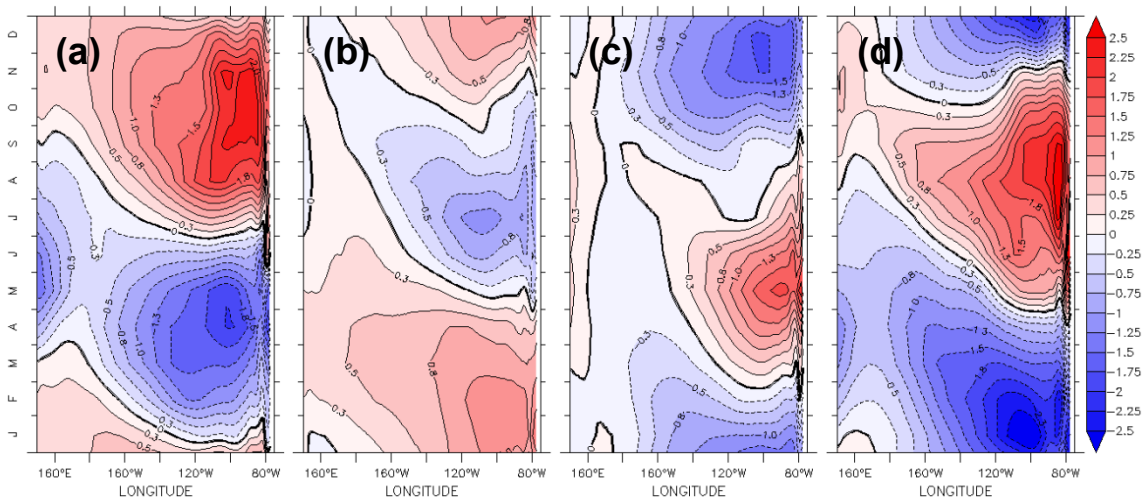

Figure 13. Change, relative to the preindustrial control run, in mean 5°S-5°N Pacific SSTs (K) for (a) AE, (b) WS, (c) VE, and (d) SS.

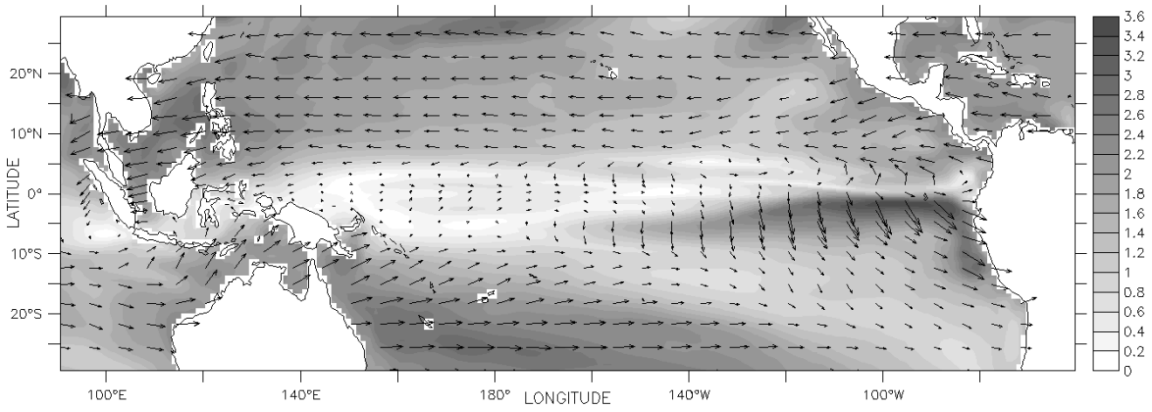

Figure 14. Longitude of perihelion of maximum seasonality (vectors), computed by fitting a first harmonic to the SST data of the four precession simulations. Vectors pointing toward 12, 3, 6, and 9 o'clock represent maximum response at longitudes of perihelion of 0° (AE), 90° (WS), 180° (VE), and 270° (SS), respectively. Shading shows the amplitude of the harmonic (K), so that darker gray represents areas where the magnitude of SST seasonality is more sensitive to a single phase of precession.

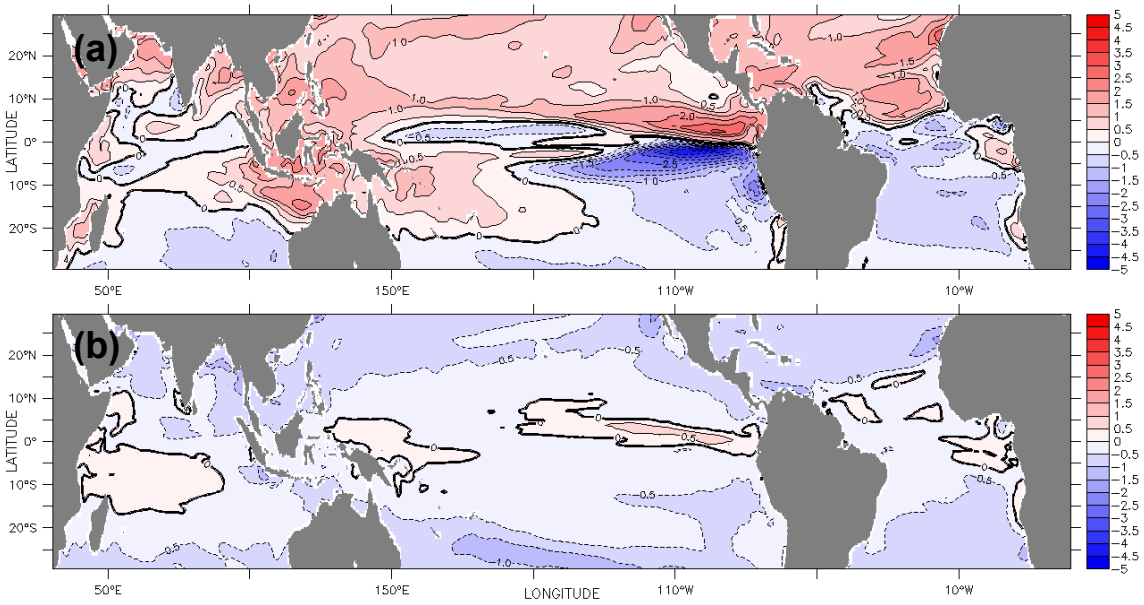

Figure 15. Change in annual temperature range (K), defined as the maximum-minimum monthly mean SST at each location, for the (a) AE-preind and (b) Lo-Hi experiments.

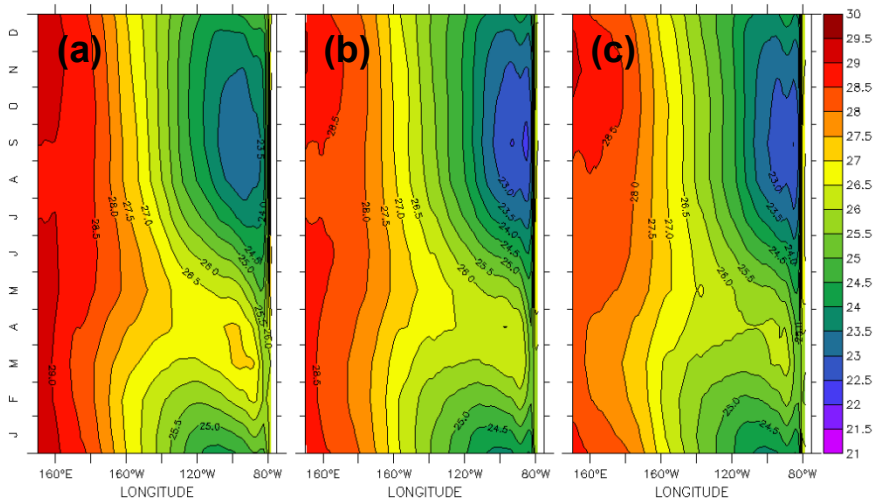

Figure 16. Like Fig. 12, but for SM2.1 simulations in (b) and (c). Mean 5°S-5°N Pacific SSTs (°C) for (a) ERSST.v3b observations as well as (b) preindustrial and (c) zero eccentricity simulations. Fig. 16a is the same as Fig. 12a.

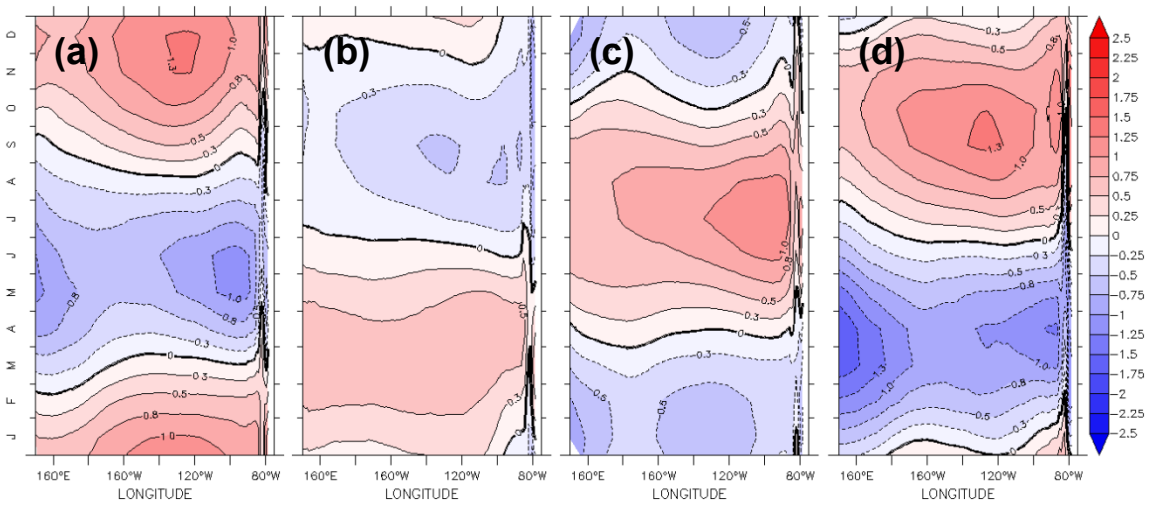

Figure 17. Like Fig. 13, but for SM2.1 simulations. Change, relative to the preindustrial control run, in mean 5°S-5°N Pacific SSTs (K) for (a) AE, (b) WS, (c) VE, and (d) SS.

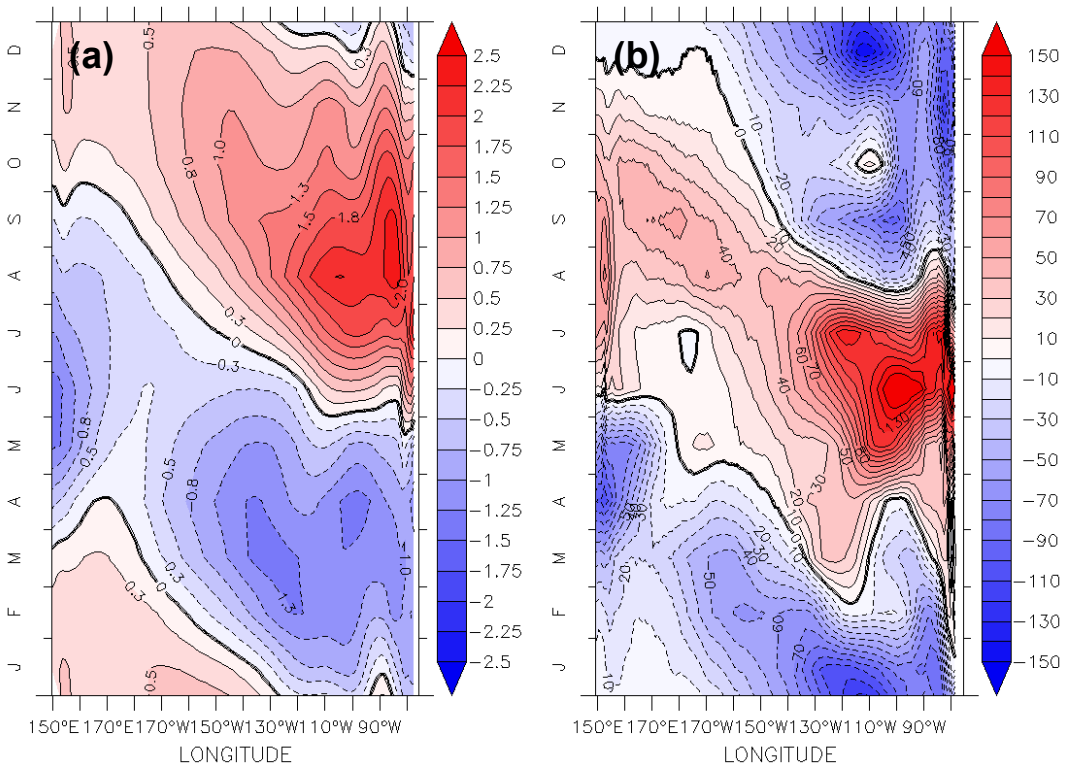

Figure 18. Longitude-time plots of (a) the change in ocean temperature (K) for the AE-preind experiment averaged over 5°S-5°N and the top 75m of ocean, and (b) the total change in heat flux (W m^{-2}) into that layer, including both surface and interior ocean fluxes.

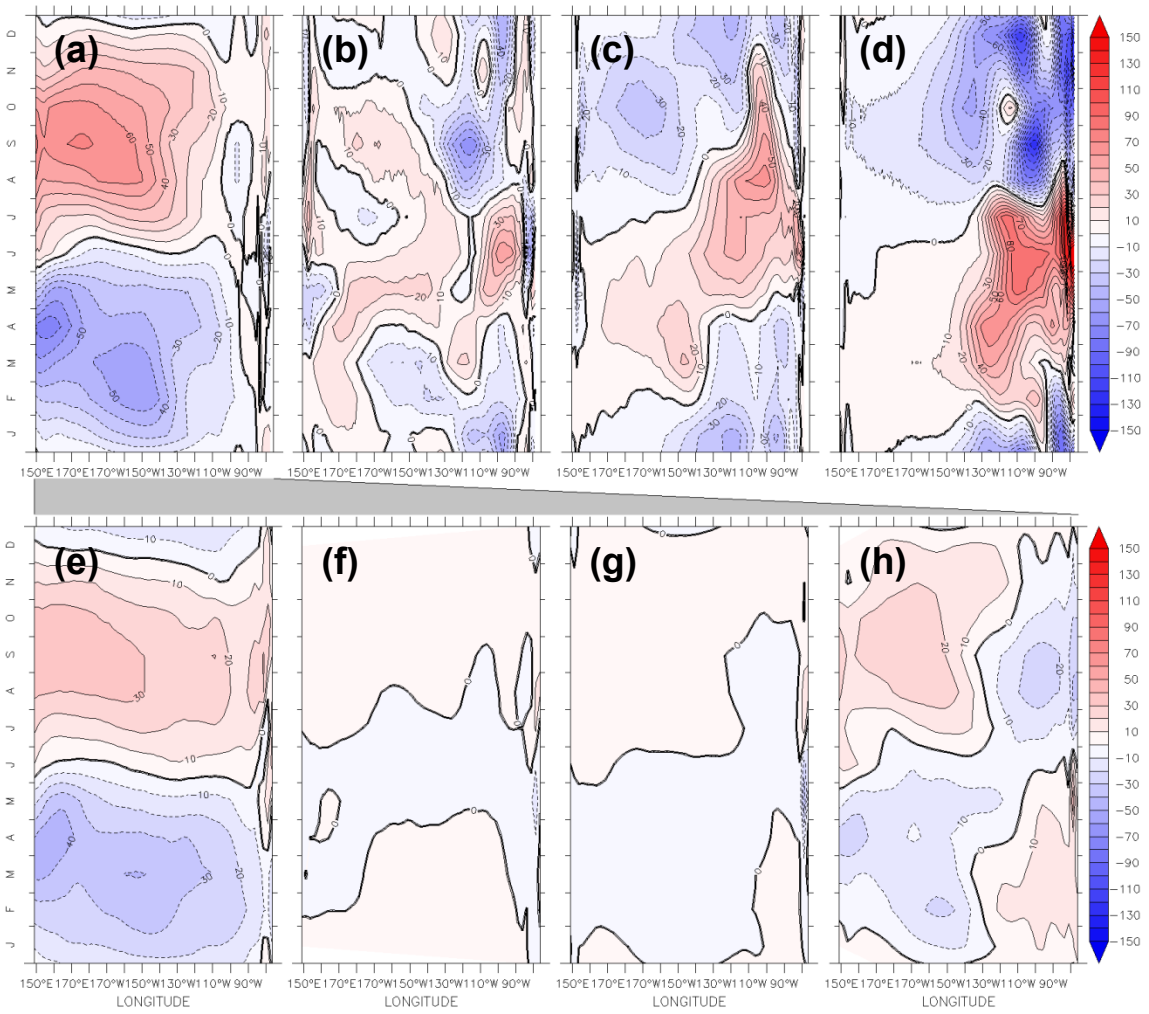

Figure 19. Longitude-time plots of changes in heat flux (W m^{-2}) for the AE-preind experiment resulting from (a) surface heat flux, (b) zonal ocean heat flux, (c) meridional ocean heat flux, and (d) vertical ocean heat flux. Together, these four fluxes equal the total heat flux in Fig. 18b. Surface heat flux is further broken down into changes in (e) net shortwave radiation, (f) net longwave radiation, (g) sensible heat flux, and (h) latent heat flux.

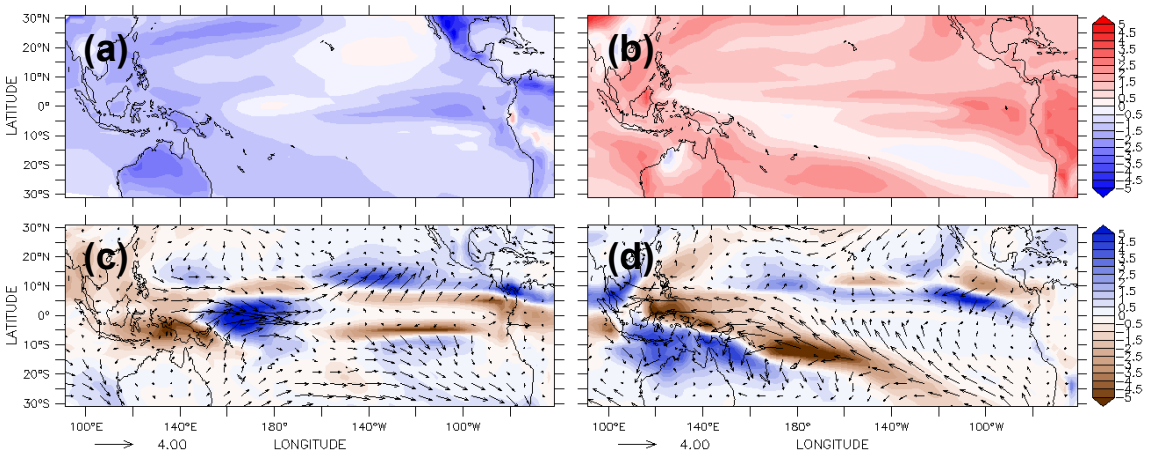

Figure 20. Change in the surface temperature (K) in (a) May and (b) November for the AE-preind experiment. Change in precipitation (shaded, mm day^{-1}) and surface wind (vectors, m s^{-1}) in (c) May and (d) November for the AE-preind experiment. May and November represent approximate months of maximum westerly and easterly wind anomalies in the western equatorial Pacific. The reference vectors in the lower left of each lower panel show the scale for a change in surface wind of 4 m s^{-1}.

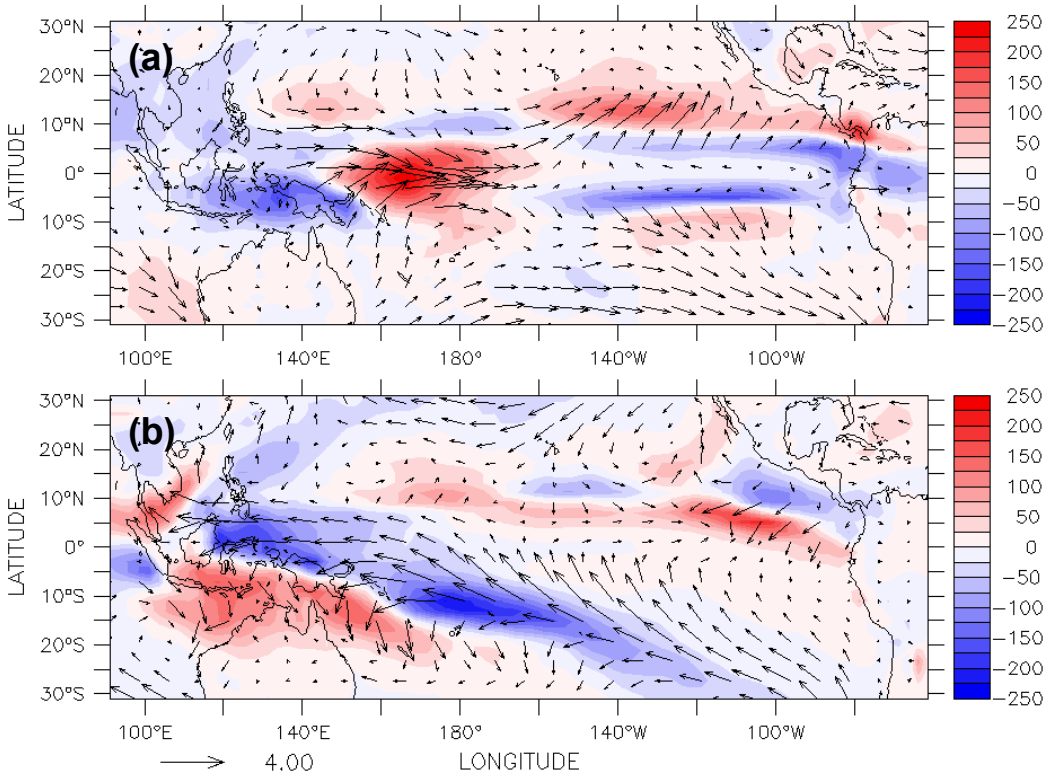

Figure 21. Change in atmospheric diabatic heating (shaded, W m^{-2}) and 10 m wind (vectors, m s^{-1}, as in Fig. 20) in (a) May and (b) November for the AE-preind experiment. Atmospheric diabatic heating is computed as the sum of contributions from SW radiation, LW radiation, convection, stratiform clouds, and sensible heat flux. Heating from convection is generally the largest component.

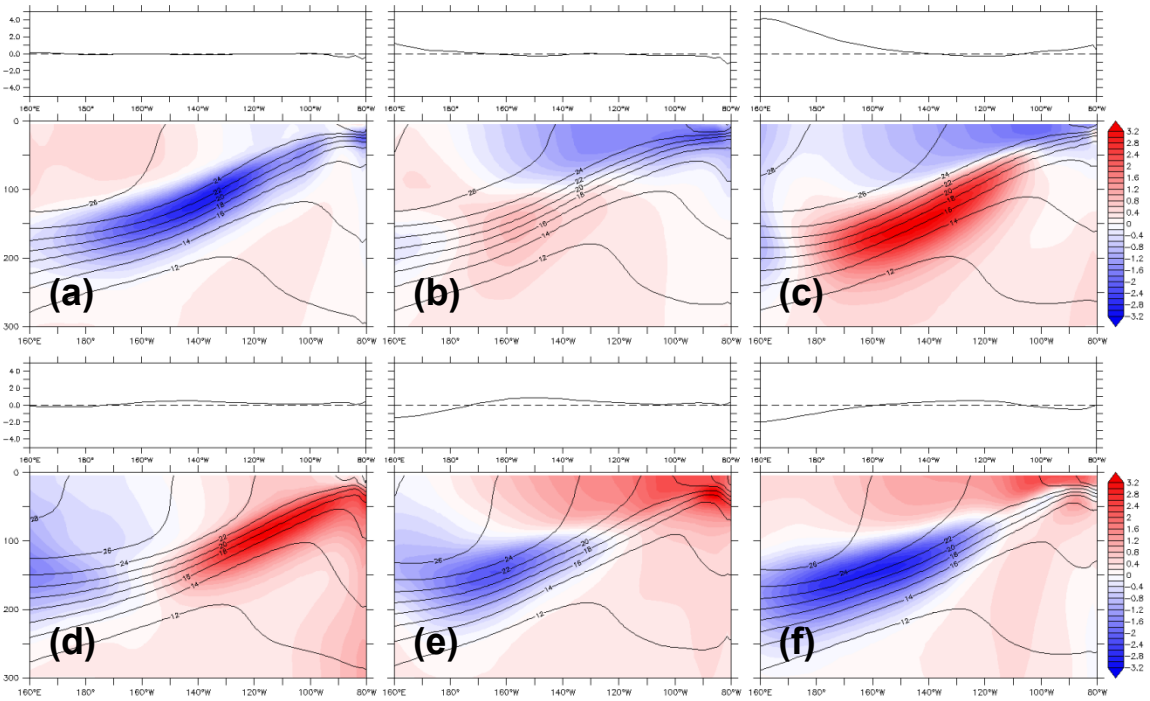

Figure 22. Change in mean 5°S-5°N zonal wind (top, m s^{-1}) and ocean temperature over the top 300 m (bottom, shaded, K) in the AE-preind experiment for (a) January, (b) March, (c) May, (d) July, (e) September, and (f) November. Contours show the isotherms of the preindustrial simulation for the same months, helping to show the depth of the thermocline.

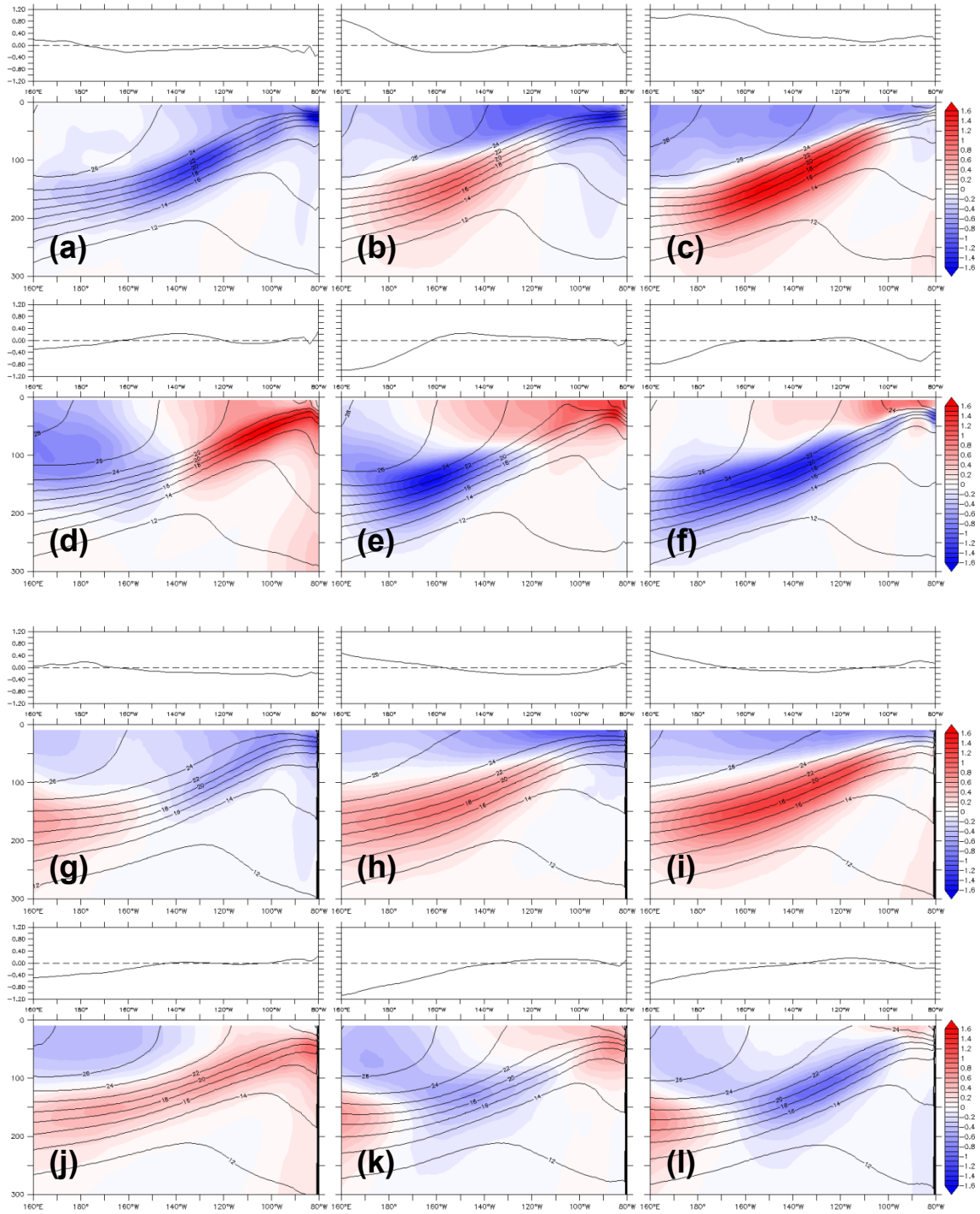

Figure 23. Like Fig. 22, but for the 6ka-preind experiments in (a)-(f) the GFDL CM2.1 and (g)-(l) the 10 model CMIP5 ensemble.

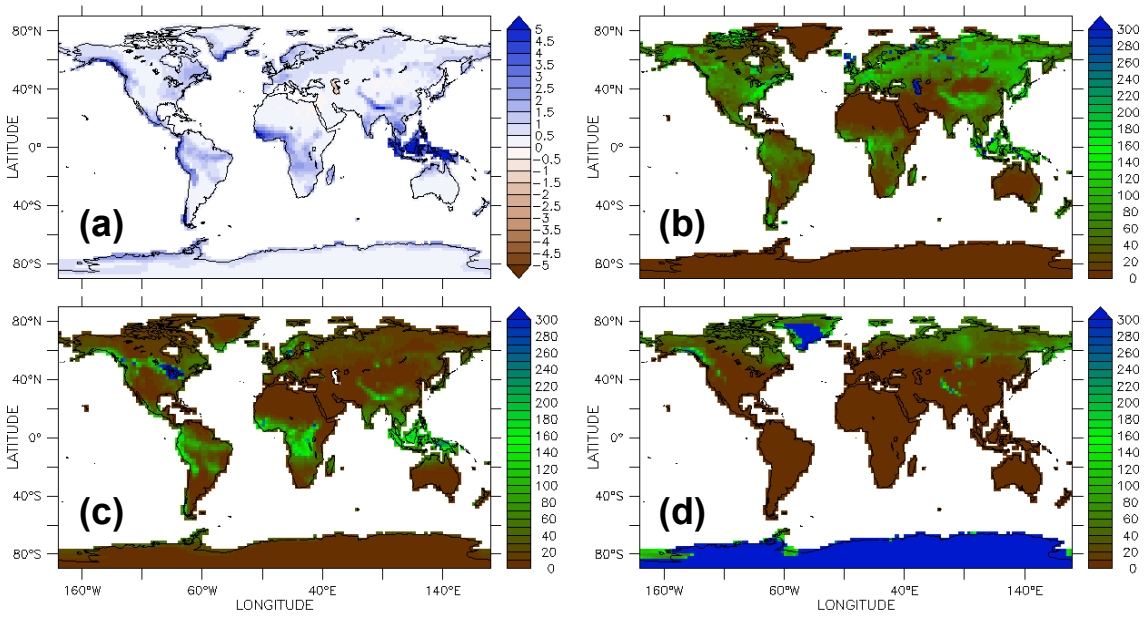

Figure 24. (a) Precipitation-evapotranspiration (mm day^{-1}), as well as (b) root zone water (kg m^{-2}), (c) deeper groundwater (kg m^{-2}), and (d) snow (kg m^{-2}) from the modern simulation of the GFDL CM2.1.

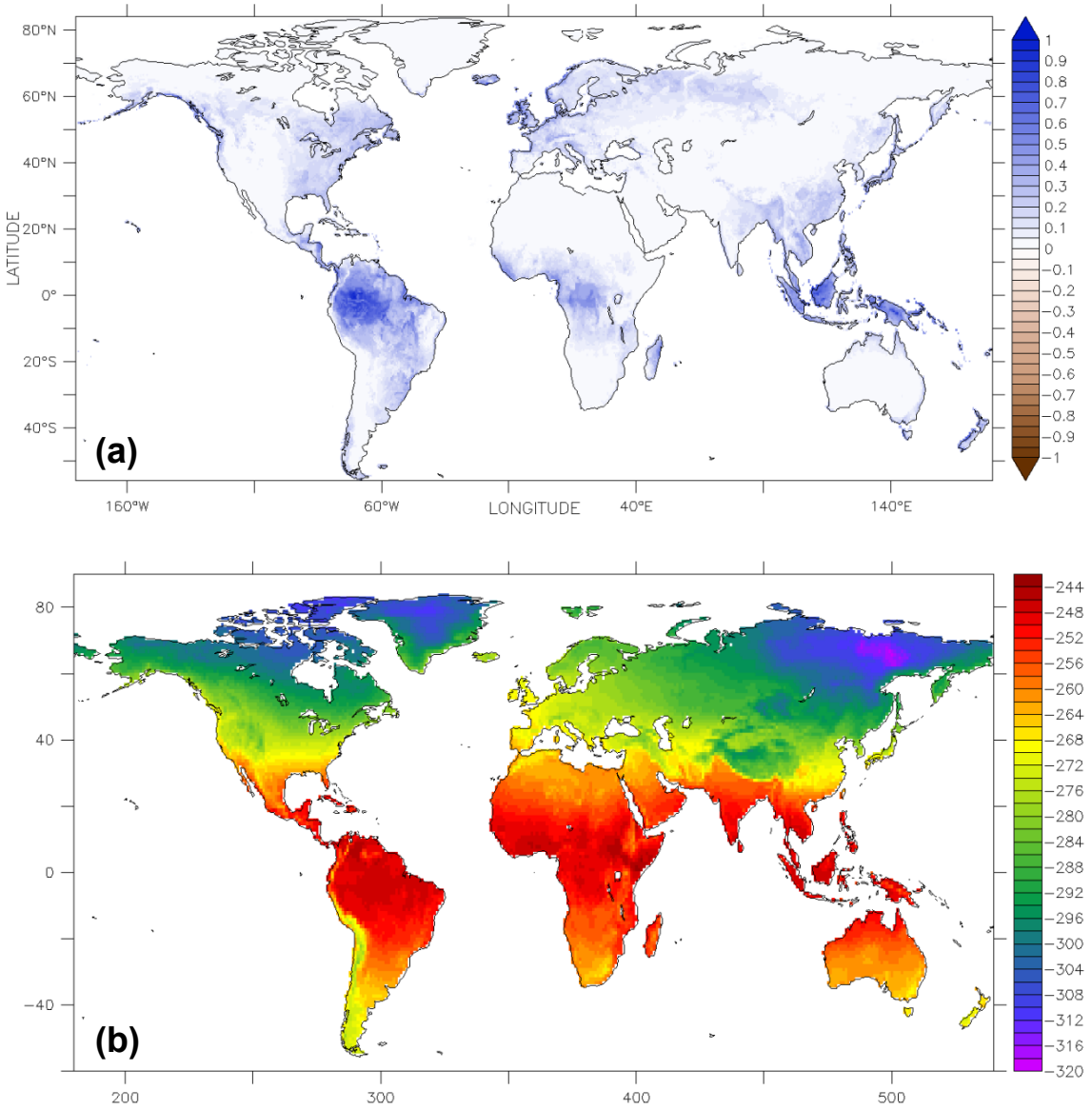

Figure 25. (a) Recharge (m/year) from Döll and Fiedler (2007), and (b) Global Land Data Assimilation System (GLDAS) winter surface air temperature (K) for the modern water table simulation (Fan et al. 2013, supplemental materials). Because the CM2.1 has a larger grid resolution, recharge values for the orbital and mid-Holocene simulations are a mix of the high resolution modern recharge in and courser 2° by 2.5° resolution P-E anomalies from the CM2.1. Areas with

negative recharge are set to zero in the model, since negative recharge values over the land is unrealistic (H. Li, personal communication).

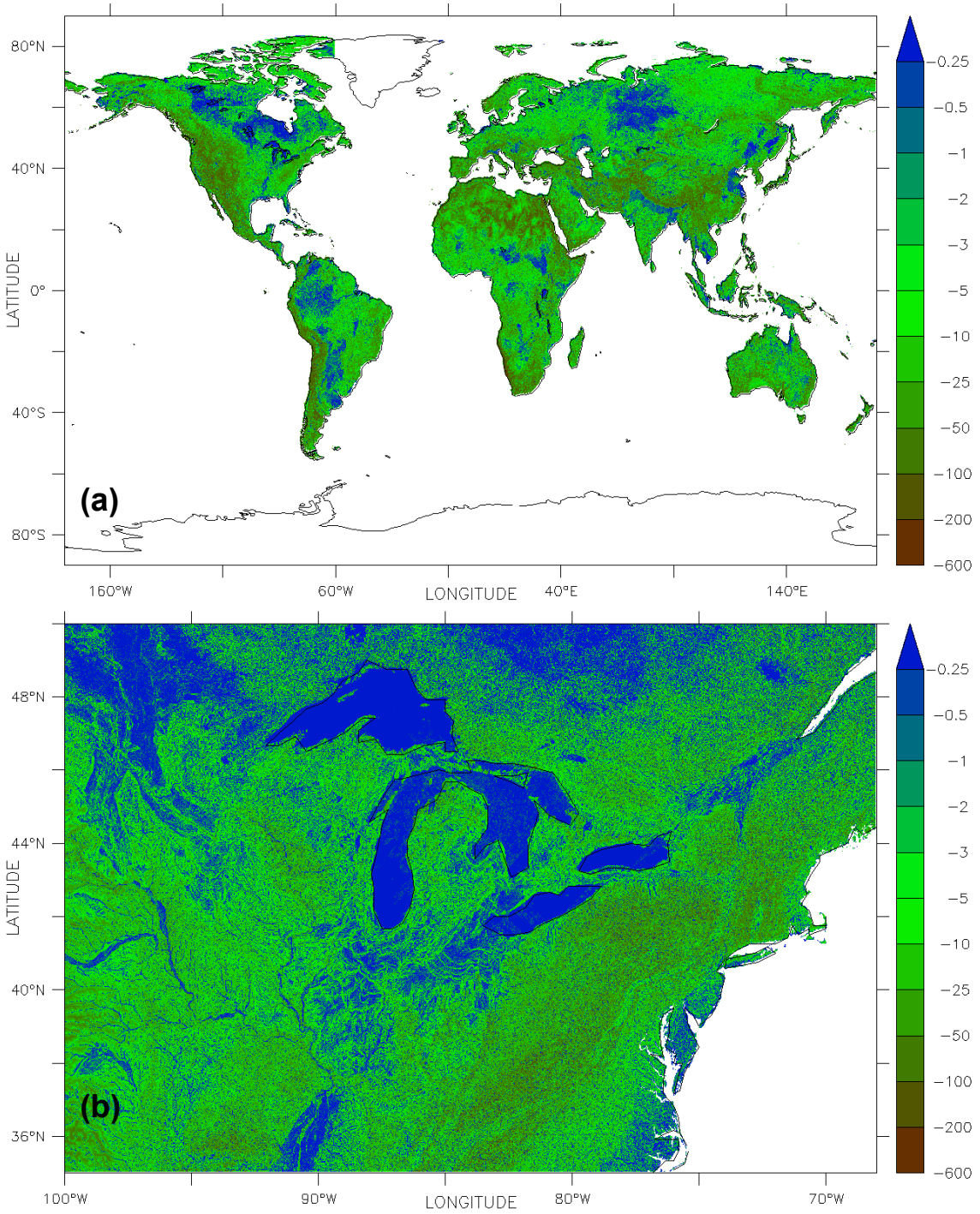

Figure 26. (a) Water table depth (m) from the modern simulation of the water table model. (b) A more detailed view of a region from (a). Negative values are deeper. Note: This is not driven by results from the modern CM2.1 simulation.

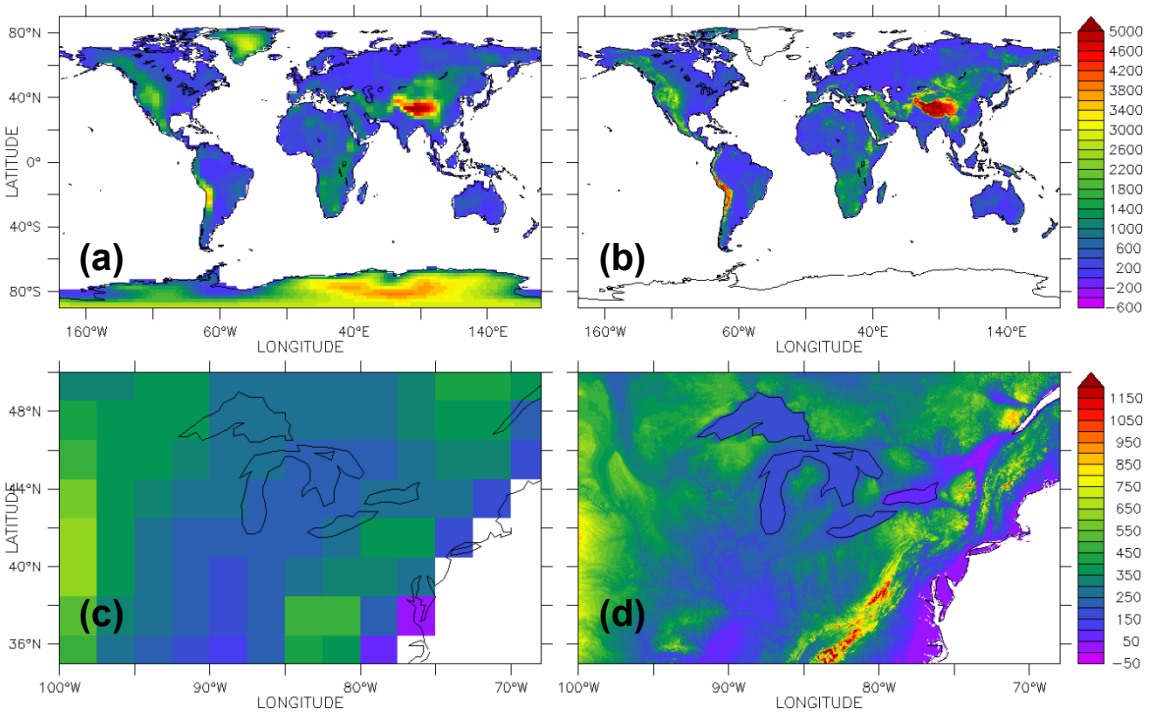

Figure 27. Topography (m) in the (a) GFDL CM2.1 and (b) water table model. (c,d) A more detailed view of part of North America for the GFDL CM2.1 and the water table model, respectively.

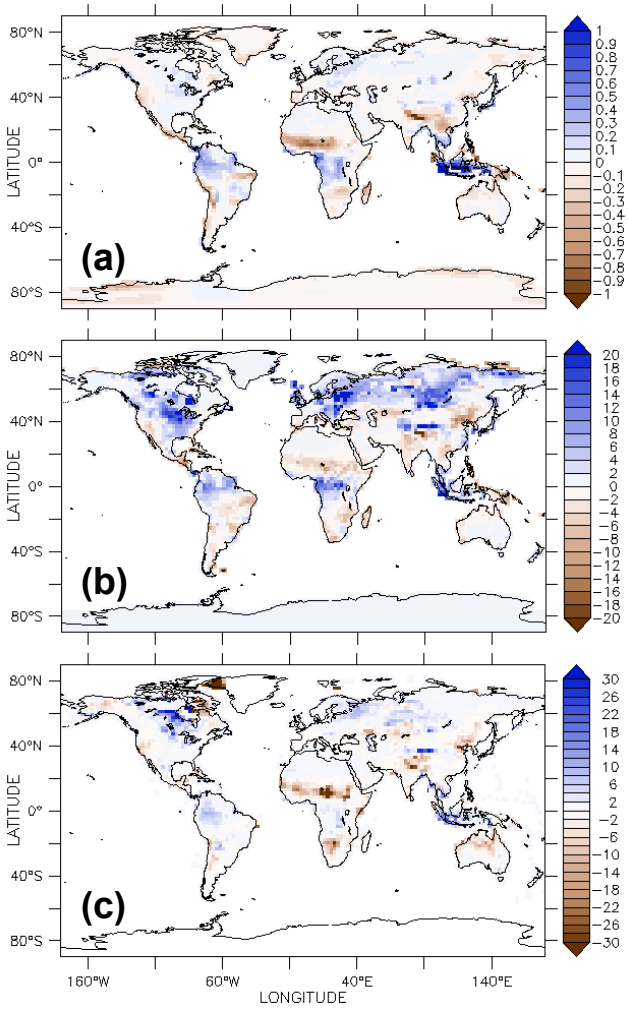

Figure 28. Changes in (a) P-E (mm day^{-1}), (b) root zone water (kg m^{-2}), and (c) shallow water table coverage (%) for the Lo-Hi experiment.

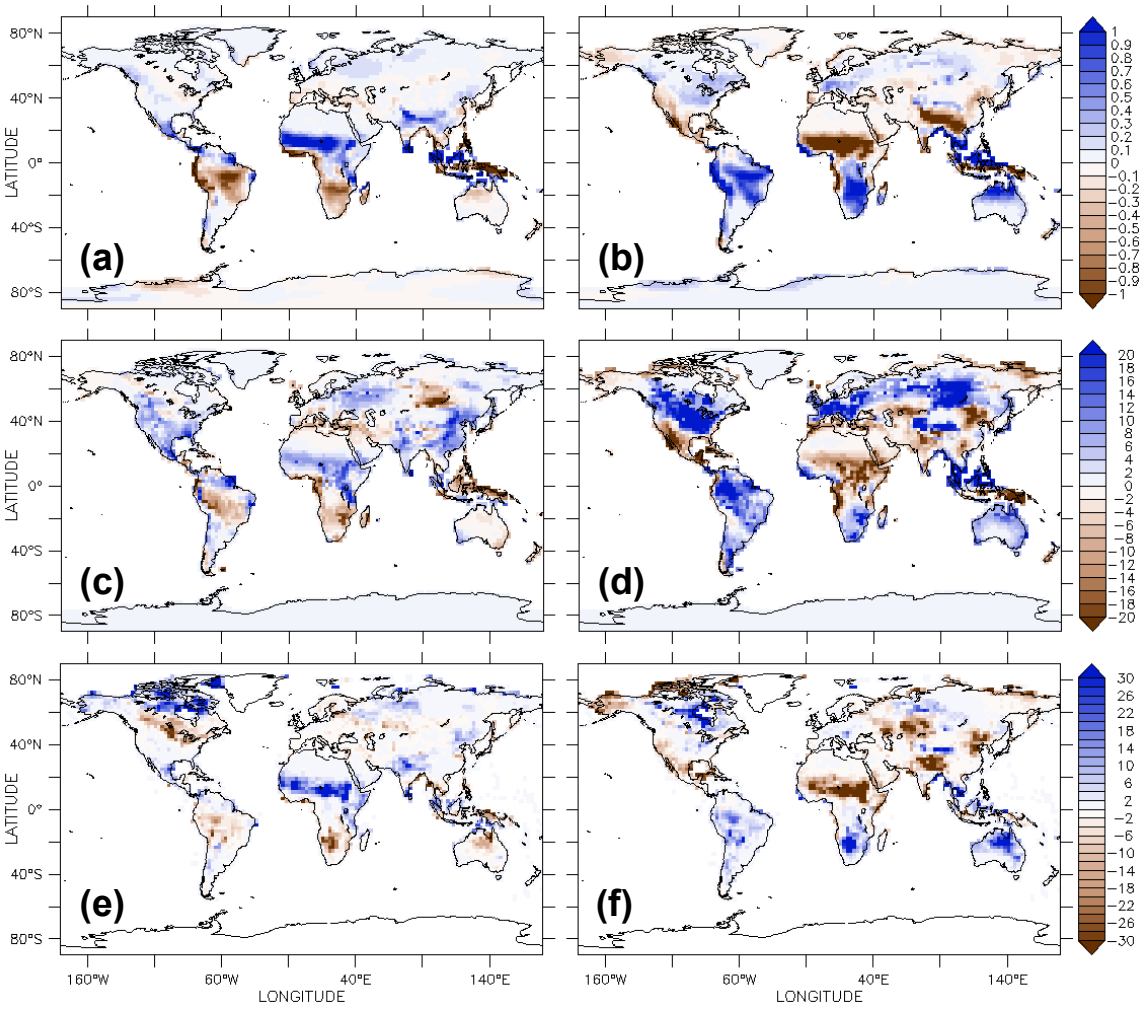

Figure 29. Changes in (a) P-E (mm day^{-1}), (c) root zone water (kg m^{-2}), and (e) shallow water table coverage (%) for the AE-VE experiment. (b,d,f) The same quantities for the WS-SS experiment.

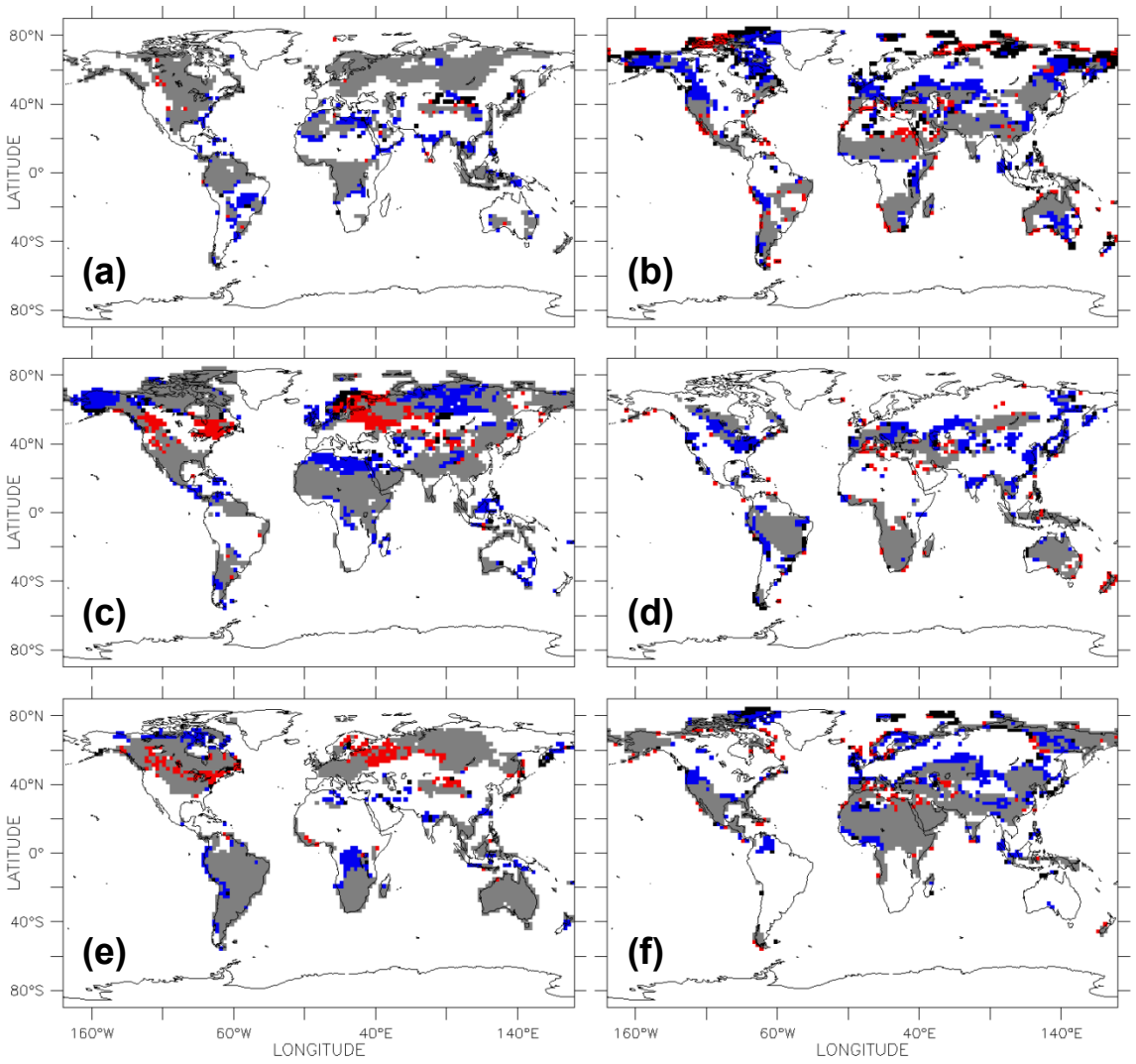

Figure 30. Similarities and differences in sign between changes in P-E, root zone water, and shallow water table coverage for (a,b) Lo-Hi, (c,d) AE-VE, and (e,f) WS-SS experiments. Left column shows areas of increased P-E and right column shows areas of decreased P-E. The four colors represent areas where changes in root zone water and shallow water table coverage are the same sign as changes in P-E (gray), where only root zone water is different (blue), where only shallow water table coverage is different (red), and where both are different from P-E (black).

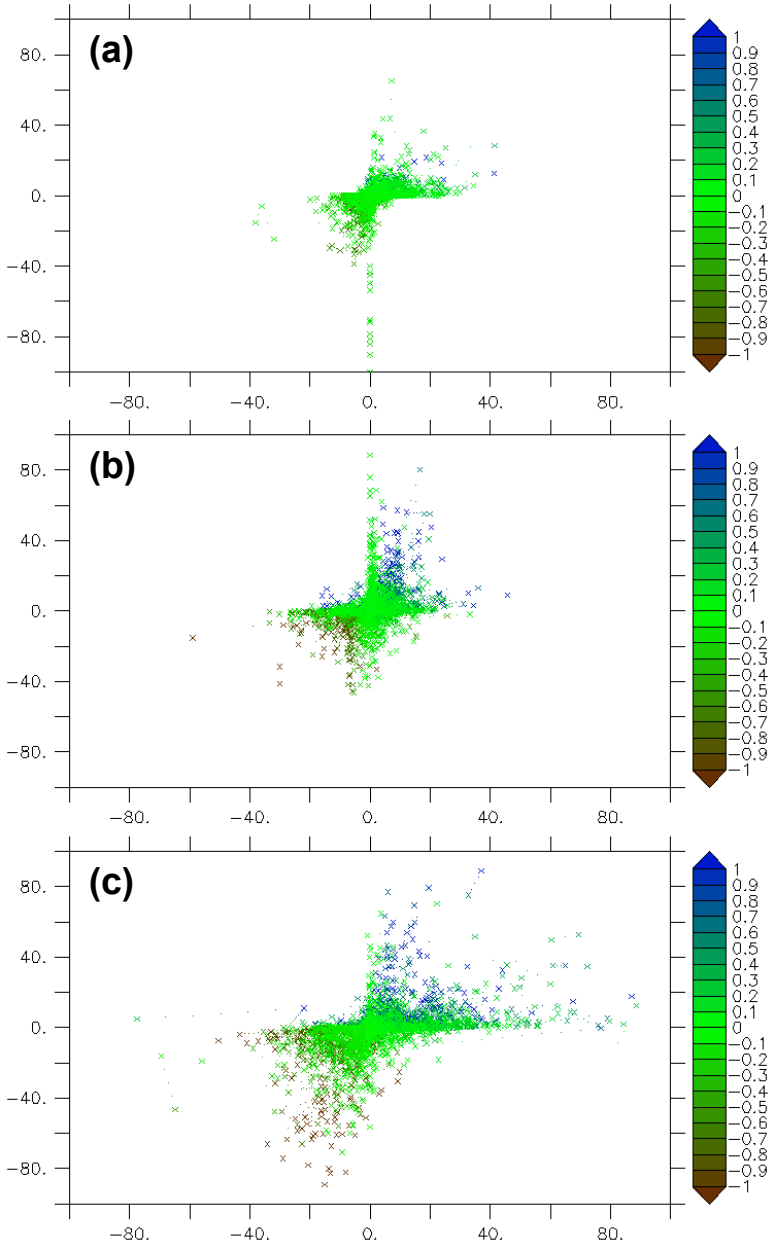

Figure 31. Scatter plots showing the relationship between changes in root zone water (x axis, kg m^{-2}) and changes in shallow water table coverage (y axis, %) for the (a) Lo-Hi, (b) AE-VE, and (c) WS-SS experiments. Correlation (r) values are shown in Table 7. Lo-Hi and WS-SS experiments each have one value with change in root zone water greater than 100 kg m^{-2}, which are not shown in order to present a better viewing area.

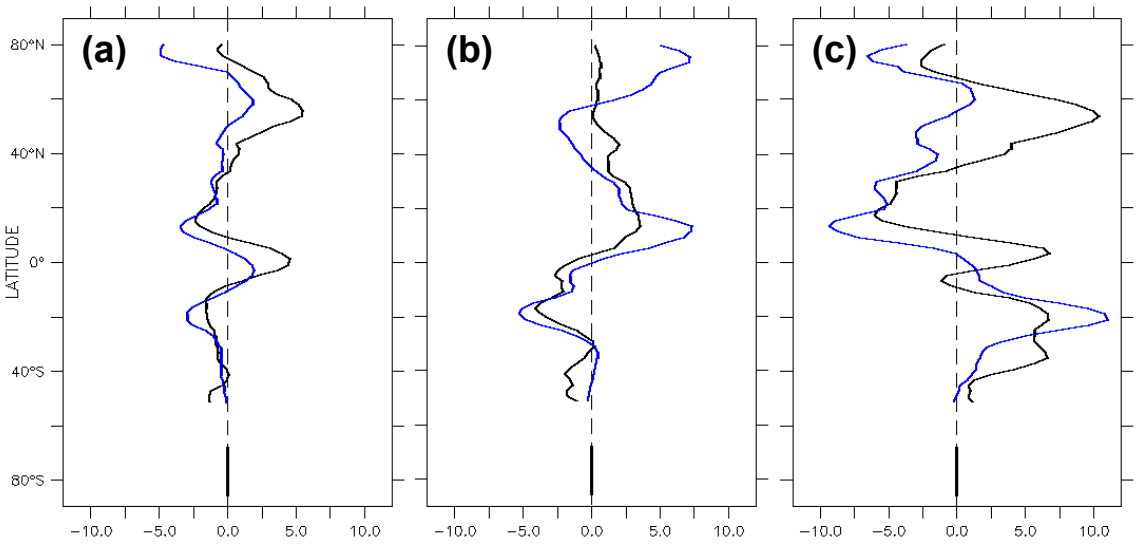

Figure 32. Zonal mean changes in root zone water (black, kg m^{-2}) and shallow water table coverage (blue, %) for the (a) Lo-Hi, (b) AE-VE, and (c) WS-SS experiments.

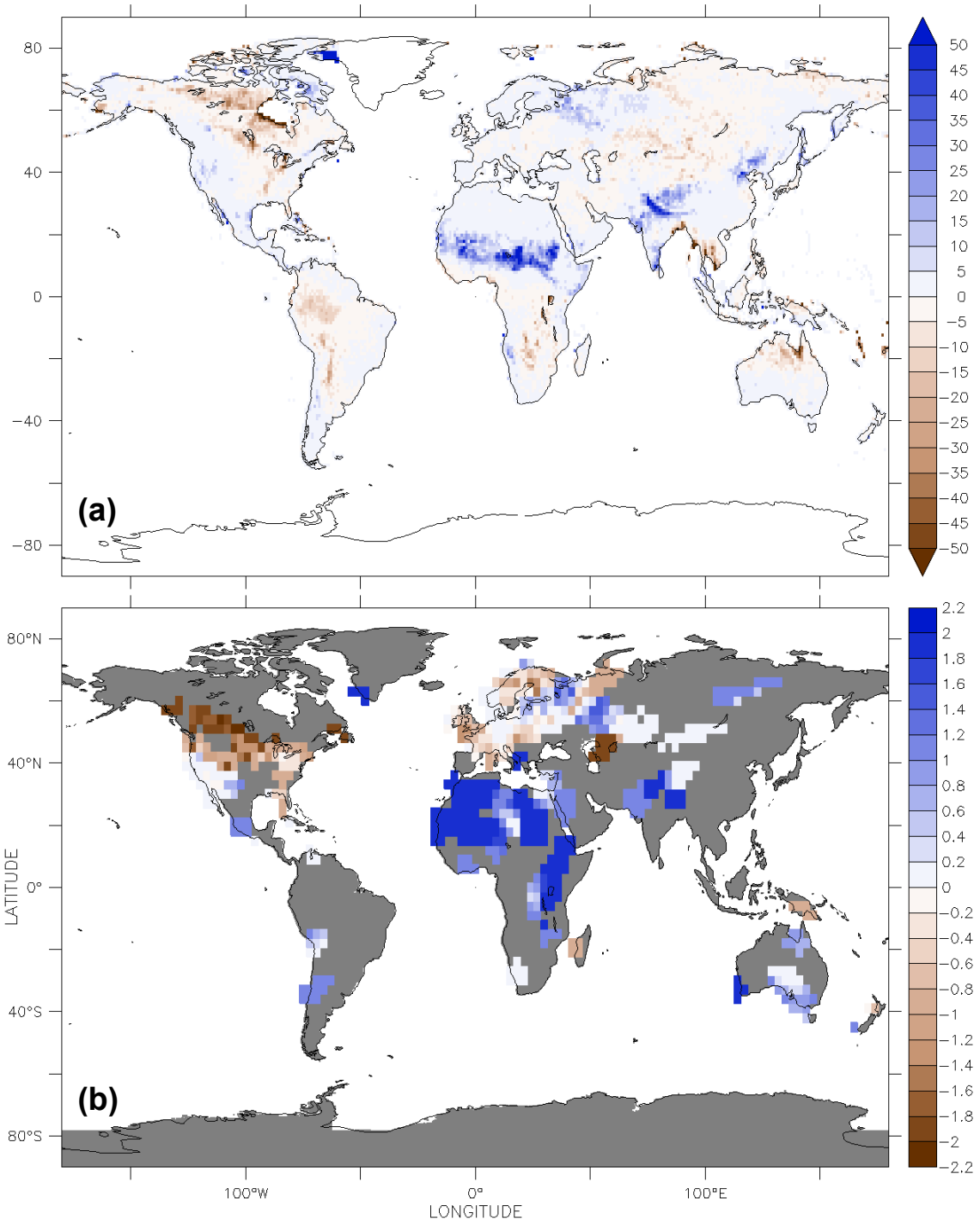

Figure 33. (a) Change in shallow water table coverage (%) for a 6ka-modern water table model experiment. (b) Change in relative lake height (from Global Lake Level Status Grids, Viau and Gajewski 2001). Gray regions in (b) do not have data in at least one of the time periods. Shallow water table coverage is

calculated on a 1° by 1° grid to show additional detail. Because shallow water table coverage is not being compared to the CM2.1 results here, the courser 2° by 2.5° grid is not necessary.

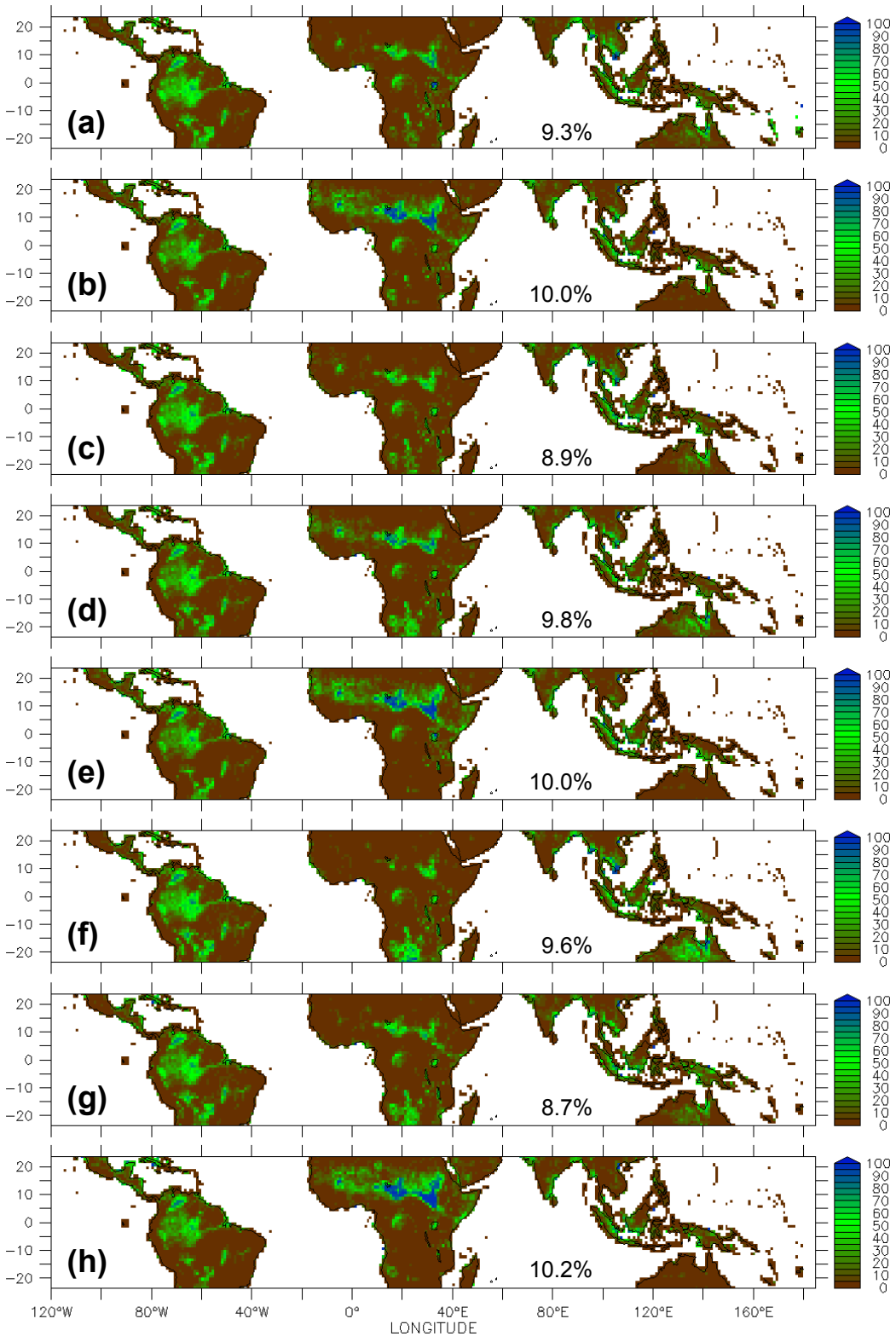

Figure 34. Shallow water table coverage (%) for (a) modern, (b) 6ka, (c) Lo, (d) Hi, (e) AE, (f) WS, (g) VE, and (h) SS. Mean values for each simulation,

averaged over the tropics, are given on each map. Like in Fig. 33, shallow water table coverage is calculated on a 1° by 1° grid.